IN-02

NASA Technical Paper 3503

p. 116

Low-Speed Longitudinal Aerodynamic Characteristics Through Poststall for Twenty-One Novel Planform Shapes

Gregory M. Gatlin and Brian E. McGrath

August 1995

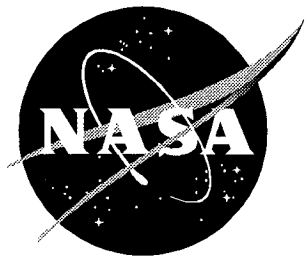

NASA Technical Paper 3503

Low-Speed Longitudinal Aerodynamic Characteristics Through Poststall for Twenty-One Novel Planform Shapes

Gregory M. Gatlin
Langley Research Center • Hampton, Virginia

Brian E. McGrath
Lockheed Engineering & Sciences Company • Hampton, Virginia

National Aeronautics and Space Administration
Langley Research Center • Hampton, Virginia 23681-0001

August 1995

Available electronically at the following URL address: http://techreports.larc.nasa.gov/ltrs/ltrs.html

Printed copies available from the following:

NASA Center for AeroSpace Information
800 Elkridge Landing Road
Linthicum Heights, MD 21090-2934
(301) 621-0390

National Technical Information Service (NTIS)
5285 Port Royal Road
Springfield, VA 22161-2171
(703) 487-4650

Summary

To identify planform characteristics which could have promise for a highly maneuverable vehicle, an investigation to determine the low-speed longitudinal aerodynamics of 21 planform geometries was conducted in the Langley Subsonic Basic Research Tunnel (SBRT). Concepts that were studied included twin bodies, double wings, cutout wings, and serrated forebodies. The planform models that were tested were all 1/4-in.-thick flat plates with beveled edges on the lower surfaces. A 1.0-in.-diameter cylindrical body with a hemispherical nose was used to house the six-component strain gauge balance on each configuration. Aerodynamic force and moment data were obtained over an angle-of-attack range of 0° to 70° with zero sideslip at a free-stream dynamic pressure of 30 psf, which corresponds to a free-stream Mach number of 0.14.

Surface flow visualization studies were also conducted on selected configurations to aid in the interpretation of the force and moment data. The surface flow was made visible through the use of fluorescent minitufts and ultraviolet lighting. Minitufts were applied to model upper surfaces in a 1/2-in.-square grid pattern, and photographs of the complete flow patterns on the configurations were taken.

Results of the investigation indicate that, when compared with single-component configurations, twin-body planforms have minimal effects on lift and longitudinal stability characteristics, while double wings can improve lift and longitudinal stability characteristics. The investigation of cutout wing planforms indicates that, when compared with noncutout configurations, cutout planforms can improve lift characteristics; however, cutout size, shape, and position and wing leading-edge sweep all influence the effectiveness of the cutout configuration. Tests of serrated forebodies identify this concept as an extremely effective means of improving configuration lift characteristics. Increases of up to 25 percent in the values of maximum lift coefficient can be obtained when compared with a nonserrated forebody configuration.

Introduction

With continuing demand for increased maneuverability of fighter aircraft, especially at high angles of attack (ref. 1), novel control concepts are receiving more and more attention. A number of concepts such as deployable strakes (refs. 2–5), blowing and suction systems (refs. 5–10), and porous surfaces (refs. 11–13) have been developed for a variety of applications. These novel means of control could be incorporated into a newly developed vehicle design and result in a configuration with substantially greater maneuverability than current fighter aircraft configurations. However, to develop such a vehicle, appropriate initial studies would include an investigation of the characteristics of various total configuration planform shapes. A study of complete configuration planforms could identify promising combinations of wing and body shapes which would be appropriate for a highly maneuverable vehicle. Thus, to assess alternate planforms for efficient high-angle-of-attack performance, a low-speed study was undertaken.

This report presents the low-speed aerodynamic characteristics of 21 flat plate planform models. Because wings and bodies affect the overall configuration aerodynamics, both wings and bodies were varied as part of the investigation. Therefore, the term planform is used throughout this report to refer to the total configuration including wings and bodies. The goal of this investigation was not necessarily to define an optimum planform shape but to identify promising planform concepts. High lift performance and benign stability characteristics at all angles of attack were the primary features of interest.

Current fighter aircraft are typically designed for both speed and maneuverability, but because air-to-air combat generally occurs at subsonic speeds, maneuverability is of utmost importance. (See ref. 14.) These requirements drive fighter aircraft to designs with wing leading-edge sweeps ranging from 20° to 70°, depending on the mission, and low aspect ratios ranging from 2 to 4. (See refs. 14 and 15.) The resulting planforms are typically delta, arrow, and low-aspect-ratio swept wings. The objective of providing pilots with maximum visibility has also resulted in designs of slender forebodies with cockpits located as far forward on the vehicles as possible. These fundamental design characteristics of low-aspect-ratio swept wings and slender forebodies are still present in the planforms that are discussed in this report.

The 21 planforms that were investigated included flat plate representations of double-wing and cutout wing configurations as well as twin-body and serrated forebody concepts. Double-wing and cutout wing configurations were expected to benefit from a forward and an aft lifting surface, which would act independently at moderate to high angles of attack. Previous research on close-coupled wing-canard configurations (refs. 16–18) has shown favorable improvements in maximum lift coefficients when a close-coupled canard was added to the basic wing planform. Thus, in this investigation, it was anticipated that two separate wings would generate lift more effectively than one. In addition, the effects of cutout size, shape, and location were investigated. Twin-body and serrated forebody configurations were included to investigate the effects of multiple forebody vortices on the high-angle-of-attack characteristics. The serrated

forebody was specifically designed so that a vortex would form on each forebody serration; thus, multiple vortices would extend over the length of the configuration. These multiple vortices were expected to enhance lift-generating capability at moderate to high angles of attack.

In typical planform studies such as those presented in references 19–21, the effects of wing aspect ratio, leading-edge sweep, and trailing-edge sweep on the longitudinal aerodynamic characteristics must be investigated. Therefore, baseline planform shapes that included variations in these parameters were designed, built, and tested; the acquired data were used as a reference point for comparison with the alternate planform concepts.

Longitudinal aerodynamic data were obtained in the Langley Subsonic Basic Research Tunnel (SBRT) on each of the 21 planforms for angles of attack ranging from 0° to 70° at zero sideslip. These data were taken at a free-stream dynamic pressure of 30 psf, which corresponds to a free-stream Mach number of 0.14. Surface flow visualization was also conducted on selected planforms to aid in the interpretation of the longitudinal force and moment data.

Symbols

All measurements are presented in U.S. Customary Units. All data have been reduced to standard coefficient form, and longitudinal data are presented in the stability-axis system.

b	wing span, in.
C_D	drag coefficient, $\frac{\text{Drag}}{q_\infty S}$
C_L	lift coefficient, $\frac{\text{Lift}}{q_\infty S}$
$C_{L,\max}$	maximum lift coefficient
C_m	pitching-moment coefficient, $\frac{\text{Pitching moment}}{q_\infty S c}$
c	planform reference length, in.
q_∞	free-stream dynamic pressure, $\frac{1}{2}\rho V_\infty^2$, psf
S	planform reference area, ft^2
V_∞	free-stream velocity, ft/sec
X_{ref}	distance from model nose to moment reference center, in.
α	angle of attack, deg
Λ	leading-edge sweep, deg
ρ	density, $slugs/ft^3$

Model Description

In this wind tunnel investigation 21 different planforms were tested. Six planforms were chosen as reference configurations and are listed in table I. The remaining 15 planforms were identified as alternate configurations and are listed in table II. The alternate configurations were designed as variations of the reference configurations. The reference area, length, and span used to calculate the aerodynamic coefficients for all configurations are presented in tables I and II. In all cases, the configuration planform reference area includes the body and wings; the cutout area of a cutout wing configuration was not included. The photograph in figure 1 shows the installation of a typical planform model in the test section of the Langley Subsonic Basic Research Tunnel (SBRT). Sketches of all planform models that were tested are presented in figures 2 and 3.

Eleven of the planforms were models that were specifically designed and built in accordance with predetermined specifications for improvement in maneuverability at high lift. These planforms are referred to as the original planform models and are presented in the sketches in figure 2. Each sketch includes side and bottom views of the model as tested with the balance housing. The top surface of each planform model is flat and lies on the centerline of the balance housing. The balance housing is a 1.0-in.-diameter cylinder with a hemispherical nose. To ensure uniform flow separation and, thus, uniform vortex formation at positive angles of attack, the leading edges were made sharp by beveling the lower surface. Trailing edges were beveled on the lower surfaces of all configurations except on the two delta wing planforms. Because the trailing edges of the delta wings were not swept, beveling would have had no effect and was deemed unnecessary. The 11 original planform models are all 1/4-in.-thick plates and include 55° and 65° delta wings, 30° and 40° diamond wings, a 47.5° diamond with a wide forebody, 30° and 40° diamond wings with twin forebodies, 30° and 40° diamond cutout wings, and two double-wing configurations.

The remaining 10 planforms were configured during the test by modifying several of the original planform models. These planforms, referred to as the modified planforms, were also designed to improve maneuverability at high lift and are presented in the sketches in figure 3. They are identified by asterisks in table II. Each modified planform was generated by attaching 1/16-in.-thick flat plates to the top of an existing model to produce the desired planform. In all cases, the edges of the flat plates were taped over to minimize the effects of any forward- and rearward-facing steps. Because the original complete configurations are defined in figure 2, only the modified overall planform shapes are presented in

figure 3. The first modified planform is referred to as the "55° delta with trailing-edge serrations." It was produced by adding a forebody and a sawtooth trailing edge to the 55° delta wing. The forebody is the same size and shape ($\Lambda = 80°$) as the standard forebody on the majority of the original configurations. The 55° delta with trailing-edge serrations configuration was used to investigate the effects of a forebody and trailing-edge serrations on a 55° delta wing.

The next five modified planforms resulted from changing the cutout area on the original 30° diamond cutout wing planform. These modifications are shown in figures 3(b)–3(f). By covering parts of the original cutout, configurations with forward, aft, and reduced-area cutouts were assembled. In addition, a planform with a diamond-shaped cutout was produced. The cutout area on the 30° diamond with diamond cutout configuration is equal to the cutout area on the 30° diamond with the smallest cutout. This was done so that the effects of cutout shape alone could be investigated. The 30° diamond with reduced cutout configuration has a ratio of cutout area to total planform area of 0.1 to 1.0, which is the same ratio as that of the 40° diamond cutout wing configuration. Thus, these two configurations provided a means of identifying leading-edge sweep effects on a cutout configuration. One last configuration was created by reshaping the 30° diamond cutout wing planform into a 55° delta cutout wing, as illustrated in figure 3(g). The remaining modified planforms were produced to study the effects of serrated forebodies. These included a delta sawtooth forebody, which was added to the 65° delta wing, and two diamond sawtooth forebody configurations, which were added to the 40° diamond wing. The serrated forebody configurations are presented in figures 3(h)–3(j).

Test Conditions and Techniques

Wind Tunnel Description

The investigation was conducted in the Langley Subsonic Basic Research Tunnel. This facility is an open-circuit atmospheric wind tunnel capable of producing a maximum continuous test-section speed of 194 ft/sec (q_∞ = 45 psf). The test-section dimensions are 22.5 in. wide by 32.25 in. high by 73 in. long. The model support system provides an angle-of-attack capability of 0° to 70° in increments of 5° while maintaining the model on the tunnel centerline. Sketches of the model support system and the balance housing used in this investigation are presented in figures 4 and 5.

Test Conditions

All 21 planforms were tested at a free-stream dynamic pressure of 30 psf (159 ft/sec), which corresponds to a nominal Reynolds number of 1.0×10^6 per foot with the model positioned on the tunnel centerline. Longitudinal data were obtained at increments of 10° for angles of attack ranging from 0° to 70°. Longitudinal data were also obtained at angles of attack of 25° and 35° to provide a better definition of the aerodynamic characteristics around $C_{L,\,max}$. All tests were conducted at zero sideslip. Because of the sharp edges on the configurations and the vortex-dominated flow fields, the application of transition grit was deemed unnecessary in this investigation.

Test Techniques

The aerodynamic forces and moments on each configuration were measured with an internal six-component strain gauge balance. Even though all six force and moment components were measured, only the longitudinal components were of interest in this study and are the only data presented. Lift and pitching-moment data are of primary interest in identifying the aerodynamic characteristics of each planform and, therefore, are analyzed in this report as each configuration is discussed. All longitudinal data are presented in table III. No base drag or base pressure corrections were made to any of the data because these corrections were not expected to have a significant effect on the overall longitudinal aerodynamic characteristics of the flat plate configurations; therefore, the zero-lift drag has been included in all drag data presented.

To present the pitching-moment data in a manner in which the planforms could be appropriately compared with one another, these data were adjusted so that all configurations would be neutrally stable at 0° angle of attack. This was accomplished by determining the moment arm increment associated with the change in pitching moment as the configuration was moved from an angle of attack of 0° to 10°. This moment arm increment was then subtracted from the moment arm at each data point to produce the desired pitching-moment data. For each configuration, the moment reference center resulting from this procedure is identified by the distance X_{ref}, as measured back from the nose, and is presented in table III. A desirable pitching-moment curve is indicated by a linear distribution of the data as presented. A linear distribution is desirable because near-neutral stability can be obtained across the angle-of-attack range by proper location of the aircraft center of gravity.

The longitudinal stability characteristics of each configuration will be independently addressed as the overall results for each planform are presented throughout the report. However, because a desirable pitching-moment curve is indicated by a linear distribution, a linear regression was performed on the pitching-moment data for each planform to provide a quantitative assessment of the planform stability characteristics. The correlation coefficients, as derived from the linear regressions, are values between zero and one and indicate the degree of linearity of the pitching-moment data. The greater the value of the correlation coefficient, the more linear the data; a value of one indicates perfect linearity. Correlation coefficients for the pitching-moment data of each of the 21 planforms are presented in table IV in decreasing order from most linear to least linear. A general assessment of these data indicates that the pitching-moment data is fairly linear for correlation coefficients of 0.90 or greater. Thus, configurations with correlation coefficients greater than 0.90 were assumed to have desirable longitudinal stability characteristics, while marginal longitudinal stability characteristics were identified with configurations having correlation coefficients between 0.70 and 0.90.

In addition to the force and moment data, flow visualization studies were conducted on selected configurations, and photographs illustrating surface flow patterns were taken. Monofilament nylon fluorescent minitufts, 0.0019 in. in diameter, were applied to the models in a 1/2-in.-square grid pattern and used with ultraviolet lighting to identify flow patterns on the upper surface of each configuration. Minitufts respond to the surface flow and indicate regions of attached or separated flow as well as areas influenced by vortical flow. Attached flow in this investigation is generally indicated when the minitufts are aligned with the free-stream flow direction, while separated flow is indicated by minitufts that are lifted off the model surface and/or randomly oriented when compared with one another. When a vortex lies above the model surface, the swirling vortical flow, which initially comes up over the swept leading edge and then moves around the vortex core, will orient the minitufts so that they are tangent to this flow. Thus, the presence of a vortex above a wing or forebody surface with a swept leading edge is generally indicated by minitufts swept in an outboard direction. Additional documentation of the fluorescent minituft flow visualization technique is presented in references 22 and 23. Flow visualization photographs, where available, are presented and discussed along with the longitudinal force and moment data. Photographs were generally taken at the angle of attack corresponding with $C_{L,\,max}$ as well as at angles of attack of 20° and 50°.

The force and moment balance used in this investigation was designated as SWT-01 and is a standard Langley six-component strain gauge balance. The maximum static load errors for this balance have been determined to be no greater than ±0.3 percent of the maximum load of each component. Maximum errors are presented in table V for the normal, axial, and pitch components in both load and coefficient form. Even though all six balance components were measured, only the longitudinal components were of interest in this study; therefore, only the errors for these components are presented.

Discussion

The aerodynamic data figures for configuration comparisons and the flow visualization figures are listed in tables I and II. To discuss the aerodynamic characteristics of the planforms in a meaningful fashion, the data are presented in groups according to specific design characteristics.

Diamond Wings and Twin Bodies

The first set of data, presented in figure 6 provides for a comparison between the 30° and 40° diamond wings as well as identifies the effects of twin-body planforms. The single-body planforms are shown in figures 2(c) and 2(d) and the twin-body planforms in figures 2(f) and 2(g). The lift coefficient data indicate that at angles of attack up to 20°, the 30° diamond wing generates a slightly greater lift coefficient than the 40° diamond wing, but at angles of attack greater than 25°, the 40° diamond wing is clearly more effective in generating lift than the 30° diamond wing. When the 30° diamond wing with twin bodies is compared with the single-body configuration, a slight decrease in lift is noted at angles of attack below 20°, but a more substantial increase in lift occurs at angles of attack of 25° and greater. The effect of twin bodies on the 40° diamond wing is a decrease in lift at angles of attack up to 40° and an increase in lift at angles of attack from 50° to 70°. At $C_{L,\,max}$, the twin bodies improve lift on the 30° diamond wing but reduce lift on the 40° diamond wing. Therefore, the overall effect of twin bodies on both diamond wings that were tested is that no increase in lift is generated at angles of attack below 20°, while the most substantial increase in lift is generated by twin bodies on the 30° diamond wing at angles of attack greater than 20°. This occurs because at angles of attack below 20° strong forebody vortices have not yet formed, and thus, the addition of a second forebody provides no lift benefit. However, at angles of attack of 50° and greater, an additional forebody produces an additional set of forebody vortices, and thus, the lift-generating capability is enhanced. At angles of attack between 20° and 50°, the effectiveness of the

forebody vortices in producing additional lift is most likely dependent on the interaction of the forebody and wing vortices. The drag coefficient data (fig. 6(b)) indicate a slight improvement in the drag characteristics in the region of $C_{L,\,max}$ of the 30° diamond wing with the addition of the second body; however, no appreciable benefit is obtained from the 40° diamond wing with twin bodies.

As mentioned previously when analyzing the pitching-moment data, note that a desirable pitching-moment versus angle-of-attack curve is indicated by a linear distribution. With this in mind, the pitching-moment data presented in figure 6(c) indicate only a small effect due to twin bodies for both diamond wing configurations. These data also indicate that the 40° diamond wing would have slightly better longitudinal stability characteristics than the 30° diamond wing because of the undesirable change in sign of the slope of the pitching-moment data for the 30° diamond wing as it passes through 20° angle of attack. Also, note that the twin bodies on both diamond wing configurations generate a nose-up increment in pitching moment at 0° angle of attack, which may be due to the additional forward-facing surface of the beveled leading edge of the second forebody. Overall, however, the longitudinal stability characteristics of each of these configurations are reasonable, and the twin-body planforms do not produce any significant adverse effects. This conclusion is further supported by the correlation coefficients presented for these configurations in table IV.

In addition to the force and moment data, surface flow visualization photographs were taken of both 30° and 40° diamond wing configurations. These photographs, which show surface flow conditions as indicated by fluorescent minitufts, are presented in figures 7 and 8. Each fluorescent minituft photograph presented in this report is accompanied by a sketch which indicates the primary regions influenced by vortical flows as well as regions of attached and separated flows. These sketches are interpretations of the minituft patterns and are presented as an aid to the reader. In general in this report, tufts which are swept outboard on forebodies and swept wings indicate regions influenced by the presence of a vortex lying just above the model surface. A feed sheet originating at the leading edge of a swept wing will lift up off the surface and then revolve around the vortex core. If the vortex core lies close enough to the surface of the wing, the vortex will scrub the model surface and deflect the tufts outboard and toward the leading edge. When vortex influence is not present and the surface flow is attached and well behaved, the tufts are generally aligned with the free-stream flow direction. Separated flows often consist of some reversed flow and some dynamic erratic flow, which causes tufts to lift off the surface or to be oriented on the surface in a random disheveled fashion. Examples of each of these tuft pattern interpretations are presented in reference 22.

The sketches presented along with the photographs in figures 7 and 8 of both diamond wings show the relative location of the primary regions affected by vortical flow, attached flow, and/or separated flow. In each sketch presented in this report, the primary area affected by a forebody and/or wing vortex is identified by a shaded region. In many cases, the influence of the forebody vortices cannot be separated from the influence of the wing vortices, and a shaded region indicating the effects of both vortices is presented.

When the flow visualization photographs and sketches of both diamond wings (figs. 7 and 8) are examined at angles of attack up to 35°, the influence of a forebody vortex and a wing vortex can be seen on each side of the configuration. These vortices are typical for a configuration consisting of a forebody and a swept wing, and additional documentation of such vortices is presented in references 24 and 25. A vortex is present on each side of the forebody with its core swept aft at an angle slightly greater than the forebody sweep angle. A wing vortex is also present on each side of the configuration with its core originating at the wing-body junction. The wing vortex is swept aft at an angle slightly greater than the wing leading-edge sweep angle. These well-behaved vortical flow patterns are indicative of a prestall condition. Note that, as the forebody vortices flow aft of the wing leading edge, the forebody and wing vortices are likely to interact and the influence of both vortices will be present on the configuration. An attached flow region is indicated on the aft inboard portion of both diamond wing configurations at 20° angle of attack and illustrates that vortical flows are not influencing this area; however, some effect from the balance housing may be present. At 50° angle of attack (figs. 7(d) and 8(c)), minitufts on the forebodies are still generally swept outboard, which indicates that vortices still exist in this area. However, fully separated flows on the wings of both diamond planforms are indicated by the minitufts being lifted up off the model surface, and evidence of wing vortices no longer exists. Furthermore, the dynamics of separated flow conditions are indicated in the photograph presented in figure 7(d); completely separated flow is indicated by the minitufts on the majority of the right wing, while the minitufts on the left wing are generally well behaved and oriented in the free-stream direction. This asymmetric surface flow pattern was typical of many of the configurations at 50° angle of attack and was observed to oscillate back and forth between indications of separated flow and indications of relatively well-behaved flow on either side of the configuration. The significant amount of separated flow present at this angle of attack indicates a

poststall condition in which lift is reduced and drag is increased. Thus, the flow visualization photographs effectively illustrate the surface flow conditions and support the trends identified in the force data. Because the twin-body planforms did not produce any substantial effects in the force and moment data, flow visualization was not conducted on these configurations.

The overall results of this phase of the investigation indicate that the 30° and 40° diamond wings and twin-body configurations all perform similarly. However, the 40° diamond wing generates a slightly greater lift coefficient than the 30° diamond wing for angles of attack greater than 25°. The twin bodies produce a slight improvement in lift on both diamond wing configurations at angles of attack beyond $C_{L,\max}$ but are more effective on the 30° diamond wing configuration.

Double Wings

The next phase of the investigation dealt with the effects of double wings. As mentioned previously, double wings were expected to benefit from forward and aft lifting surfaces which would act independently to effectively generate more lift than that of a single wing at moderate to high angles of attack. A 30° diamond twin wing (fig. 2(j)) and a 60° double-arrow configuration (fig. 2(k)) were tested and these data are presented for comparison with the 30° diamond wing data in figure 9. The lift coefficient data indicate a 24-percent increase in $C_{L,\max}$ when comparing the 30° diamond twin wing with the 30° diamond wing. The 30° diamond twin wing also produces a greater lift coefficient than the 30° diamond wing at the angles of attack beyond $C_{L,\max}$. This indicates that, in the moderate- to high-angle-of-attack region, an additional wing, whether it is strongly influenced by the other wing or effectively acting independently, adds significantly to the lift-generating capability of the configuration. One explanation is that two sets of vortices may effectively generate a larger low-pressure region on the upper surface and produce greater overall lift on the surface of two small wings than would just one set of vortices on a single larger wing. The 60° double-arrow configuration generates a $C_{L,\max}$ comparable with that of the 30° diamond twin wing while generating more lift than the 30° diamond wing or the 30° diamond twin wing configurations at angles of attack beyond $C_{L,\max}$. The greater leading-edge sweep on the 60° double arrow may well account for some of the lift increases beyond $C_{L,\max}$ because the nonlinear portion of lift increases with increasing leading-edge sweep. (See ref. 26.) In a similar flat plate planform study presented in reference 24, increases in lift at and beyond $C_{L,\max}$ were noted as wing sweep was increased. The drag coefficient data (fig. 9(b)) indicate increases in both C_L and C_D at angles of attack above 20° for the double-wing configurations when compared with the single-wing configurations. The pitching-moment data indicate only slightly better longitudinal stability characteristics for the double-wing configurations than for the 30° diamond wing; however, the absence of significant nonlinearities in the data for all configurations results in relatively comparable pitching-moment characteristics. This conclusion is also supported by the correlation coefficients presented in table IV.

Fluorescent minituft photographs were taken of both double-wing configurations and are presented in figures 10 and 11. As noted in previous flow visualization photographs, the minitufts being swept outboard on the forebody indicate that forebody vortices are present on both configurations at all angles of attack presented up to 50°. On the 30° diamond twin wing, vortical flow regions are indicated on both wings at angles of attack of 20° and 35°. Other promising surface flow conditions are indicated at 50° angle of attack (fig. 10(c)) where the surface flow appears to have less separation than on the 30° diamond wing. (See fig. 7(d).) Specifically, at 50° angle of attack, the minitufts on the leading edges of the wings of the 30° diamond twin wing are lying in a more streamwise direction than the minitufts on the 30° diamond wing. The aft wing is benefitting from operation at a lower effective angle of attack because of the downwash (ref. 27) from the forward wing while the forward wing may simultaneously be benefitting from a similar influence because of the presence of the aft wing. The possibility of both wings operating at effectively reduced angles of attack would generate more lift in the poststall angle-of-attack range and could explain the greater lift generated by the 30° diamond twin wing than by the 30° diamond wing. The surface flow visualization of the 60° double-arrow configuration (fig. 11(c)) indicates the same general trends on the forward wing as on the wings of the 30° diamond twin wing configuration. However, the 60° leading-edge sweep produces a wing vortex which lies farther inboard than the wing vortex on the 30° diamond wing. The more inboard location of the wing vortex on the 60° double arrow has a greater influence on the overall configuration and, thus, could account for the improved lift characteristics beyond $C_{L,\max}$. In addition, the more inboard location of the wing vortex could possibly result in a beneficial interaction between the forebody and wing vortices. However, the flow over the outboard portion of the aft wing of the 60° double arrow is very different from the flow over the forward wing. At each of the angles of attack presented, the random orientation of the minitufts and the fact that they are generally lifted up off the model surface indicate that the flow over the aft wing appears to be separated. This means that the outboard region of the aft

wing is not generating as much lift as would a wing with attached flow.

The overall results of the double-wing tests indicate that double-wing planforms produce increased lift and improved stability characteristics when compared with single-wing planforms. However, the aft-wing planform may require specific attention to issues such as vertical and horizontal placement as well as size to ensure that the flow over the aft wing is not separated.

Forebody Effects

The effects of a wider forebody as well as the effects of adding a forebody to the 55° delta wing were investigated, and the results are presented in figure 12. When compared with the 40° diamond wing, the 47.5° diamond with wide forebody (fig. 2(e)) produces a $C_{L,\max}$ that is 11.5 percent greater. This increased $C_{L,\max}$ may be due to the wider forebody and/or to the increased sweep of the main wing; aerodynamic data in reference 24 indicate that a wider forebody will increase $C_{L,\max}$. When the 55° delta with trailing-edge serrations (fig. 3(a)) is compared with the original 55° delta wing, a less abrupt drop-off in C_L occurs after $C_{L,\max}$ for the 55° delta with trailing-edge serrations. Although the 55° delta wing produces a greater $C_{L,\max}$, the 55° delta with trailing-edge serrations produces greater lift coefficients at angles of attack of 30° to 70°. This indicates that the presence of the forebody and the trailing-edge serrations on the 55° delta wing significantly improve the lift characteristics at angles of attack beyond stall. Previous studies have identified lift increases due to the addition of a forebody to a delta planform (ref. 24); the addition of the forebody to the 55° delta wing, rather than the trailing-edge serrations, is expected to account for most of the lift increase. When pitching-moment data are compared, the 55° delta with trailing-edge serrations shows the least desirable longitudinal stability characteristics, while the other three configurations are substantially better. In fact, the correlation coefficients presented in table IV indicate that the 47.5° diamond with wide forebody, the 55° delta wing, and the 40° diamond wing have the most desirable longitudinal stability characteristics of all the configurations tested.

Surface flow visualization photographs were taken of the 55° delta wing and the 55° delta with trailing-edge serrations and are presented in figures 13 and 14. When these configurations are compared at 20° angle of attack, both indicate the influence of strong vortical flows over the majority of the configuration. As expected from the previous discussion of flow visualization photographs, strong vortical flows are noted on the forebody of the 55° delta with trailing-edge serrations. When the two configurations are compared at 35° angle of attack, the flow patterns are very different. The 55° delta wing (fig. 13(c)) has separated flow over the majority of the configuration, while the 55° delta with trailing-edge serrations (fig. 14(b)) has very little, if any, separated flow. This explains why the 55° delta with trailing-edge serrations generates much more lift than does the 55° delta wing at this test condition. Furthermore, note in reference 24 that forebody vortices resulting from the addition of a forebody to a delta wing will have a stabilizing effect on the wing vortices and actually delay wing vortex breakdown. This appears to be occurring in the flow visualization photographs just discussed at an angle of attack of 35°. At an angle of attack of 50°, the photographs of both configurations indicate substantial regions of separated flow. Examination of the surface flow pattern on the sawtooth trailing-edge region of the 55° delta with trailing-edge serrations did not reveal any unexpected or significant flow phenomenon in this area at any of the test angles of attack.

In summarizing these comparisons, note that forebody effects can be dependent on three-dimensional characteristics; more specifically, forebody vortex location will depend on the three-dimensional shape of the forebody. The results in this report show only two-dimensional effects because the models are flat plates; therefore, further tests would be required to represent three-dimensional configurations properly and to determine their associated aerodynamic characteristics. This study shows that a wider forebody on a diamond wing planform or the addition of a forebody and trailing-edge serrations to the 55° delta wing generally improves lift at angles of attack of 30° and above. The addition of a forebody to the 55° delta wing produces beneficial vortical flows over the configuration for angles of attack up to approximately 35°. However, the longitudinal stability characteristics, generally, were not improved with the widening or addition of a forebody.

Cutout Wings

The evaluation of the effects of wing cutout regions was a significant portion of this wind tunnel investigation. The first data to be presented are for the 30° and 40° diamond wings with the original cutouts. (See fig. 15.) The intent of wing cutouts was to postpone flow separation on the wing by energizing the flow aft of the cutout and to produce a forward and an aft wing with reduced chords when compared with the noncutout wing. Thus, attached flow on the forward portion of the wing would be maintained at higher angles of attack. The lift coefficient data for the 30° diamond wing and the 30° diamond cutout wing indicate that the cutout wing produces decreased lift coefficients at angles of attack between 10° and 35° and a decreased $C_{L,\max}$. However, this same comparison for the 40° diamond wings indicates that the

cutout improves the lift characteristics in the angle-of-attack region around $C_{L,\max}$ and postpones $C_{L,\max}$ by approximately another 5° angle of attack. At angles of attack between 40° and 70°, the cutout configurations generate greater lift coefficients on both diamond wing planforms. The drag data for the 30° diamond wing configurations indicate that the cutout configuration produces a greater drag coefficient than the noncutout configuration across the angle-of-attack range. However, at prestall conditions, the 40° diamond wing configurations have roughly the same drag characteristics. When evaluating the pitching-moment data, the trends indicate that the wing cutouts tend to degrade the longitudinal stability characteristics. The cause of increased drag and degraded longitudinal stability characteristics produced by the cutout configurations is not clear; however, the aft portion of the wing may be immersed in or unfavorably affected by the wake from the forward portion of the wing.

Surface flow visualization was conducted on the 40° diamond cutout wing, and photographs of this configuration are presented in figure 16. The conditions presented in figure 16 can be compared directly with the flow visualization photographs of the 40° diamond wing presented in figure 8. If the cutout configuration is thought of as having both a forward and an aft wing surface, then the flow over the aft wing is shown to be separated at all angles of attack presented (i.e., 20°, 35°, and 50°). The surface flow on the 40° diamond wing is not separated at either 20° or 35° angle of attack. This explains why the 40° diamond wing produces more lift at 20° angle of attack than the 40° diamond cutout wing. This same trend would be expected at 35° angle of attack; however, why both configurations produce the same lift coefficient at this condition is not clear. When the photographs of the 40° diamond cutout wing (figs. 16(a) and 16(b)) are compared with those of the 40° diamond wing (figs. 8(a) and 8(b)) at angles of attack of 20° and 35°, note that the presence of the cutout affects the wing vortex and may cause it to burst prematurely or to be moved farther off the body. This conclusion is derived from the fact that the presence of a vortex is indicated by the outboard-swept minitufts on the aft portion of the 40° diamond wing, whereas the minitufts on the aft portion of the 40° diamond cutout wing do not indicate the presence of a vortex at all. The reason for the improved lift performance of the cutout wing (fig. 16(c)) when compared with the 40° diamond wing configuration (fig. 8(c)) at 50° angle of attack is not evident from the flow visualization photographs as both indicate separated flow over the wings. However, lift coefficients on the cutout configuration may be greater because the cutout regions produce less lift than the regions that are retained (e.g., forebody region). Therefore, the combination of a smaller reference area and high-lift regions results in a greater overall lift coefficient for the configuration. This conclusion is derived from the fact that the lift coefficients for the cutout configurations are based on smaller reference areas.

The results from this initial data of cutout effects indicate that improved lift can be generated by a cutout wing design at angles of attack beyond $C_{L,\max}$. However, the exact physics of how this improvement occurs is not yet well understood. To more systematically identify cutout wing effects, several tests were conducted with various cutout sizes, shapes, and locations.

Determination of the effects of varying the wing leading-edge sweep on a cutout wing configuration while keeping the ratio of cutout area to total planform area constant was of interest. To do this, the cutout region on the 30° diamond cutout wing was reduced so that the ratio of cutout area to total planform area was equal to that for the 40° diamond cutout wing. This area ratio of 0.1 to 1.0 was the design criteria for the configuration identified as the 30° diamond wing with reduced cutout. (See fig. 3(d).) Thus, this configuration is compared with the 40° diamond cutout wing and the data are presented in figure 17. For angles of attack of 30° and above, the 30° diamond with reduced cutout generates essentially the same increase in lift coefficient over the noncutout configuration as does the 40° diamond cutout wing when compared with the 40° diamond wing. Thus, in this angle-of-attack range, wing leading-edge sweep has negligible impact on the effect of a cutout wing. At angles of attack of 0° and 10°, the 30° diamond with reduced cutout generates greater lift coefficients than the noncutout configuration, whereas the 40° diamond cutout wing does not. This may be due to an unintentional cambering effect created when the 30° diamond cutout wing planform was modified by attaching flat plates to create the reduced cutout configuration.

When the pitching-moment data for the cutout configurations are compared, the cutouts are shown to have a similar effect on both 30° and 40° diamond wings. In both cases the cutouts tend to degrade the longitudinal stability characteristics; however, the cutout effect is greater on the 30° diamond wing configuration. The data presented thus far on the effects of cutouts indicate that a cutout configuration can generate increased lift coefficients at angles of attack beyond stall and that wing leading-edge sweep in the range of 30° to 40° has little impact on cutout effects.

The effect of cutout size was investigated next. The 30° diamond cutout wing, which was modified once to reduce the cutout, was modified again to further reduce the cutout size resulting in a configuration which will be referred to as the "30° diamond with smallest cutout." (See fig. 3(e).) Longitudinal data for the 30° diamond

wing and the three cutout configurations are presented together for comparison in figure 18. The lift coefficient data indicate that the 30° diamond cutout wing (i.e., largest cutout area) produces the lowest values of lift coefficients between angles of attack of 10° and 35° when compared with the other configurations, including the 30° diamond wing. In this same angle-of-attack range, the 30° diamond with reduced cutout produces lift coefficients which are greater than those of the 30° diamond wing; the 30° diamond with the smallest cutout produces the greatest lift coefficients of the four configurations. At angles of attack from 50° to 70°, all the cutout configurations produce slightly greater lift coefficients than the 30° diamond wing. This may be due to the forward portion of the wing causing a reduced effective angle of attack for the aft portion of the wing, and thus increasing lift in this poststall region. In other words, a downward deflection of the flow on the aft portion of the wing is caused by the presence of the forward portion of the wing. The result is that the aft portion of the wing is located in the downwash (ref. 27) from the forward portion of the wing; therefore, the aft portion of the wing is at a lower effective angle of attack and generates more lift in the poststall angle-of-attack range.

Not only does the configuration with the largest cutout produce the lowest lift coefficients for angles of attack from 10° to 35°, it also produces the greatest values of drag coefficient for a given lift coefficient across the angle-of-attack range. The pitching-moment data show that all cutouts degrade stability characteristics when compared with the configuration with no cutout; the reduced cutout and the smallest cutout are the least desirable.

The overall results of the cutout size investigation indicate that a small cutout configuration exhibits better lift characteristics than a large cutout configuration; however, the smaller the cutout, the less desirable are the longitudinal stability characteristics.

In addition to looking at the effects of cutout size, the effects of cutout longitudinal location were investigated. To do this, the 30° diamond cutout wing was modified to produce configurations with forward (fig. 3(b)) and aft (fig. 3(c)) cutout locations. Longitudinal data for the 30° diamond wing as well as for the forward, reduced (centered), and aft cutout configurations are presented together for comparison in figure 19. The cutout area on each of the configurations was held constant as the cutout region was shifted fore and aft. The data indicate increased lift coefficients across the angle-of-attack range for all cutout configurations; however, $C_{L,\max}$ is the greatest for the configuration with the cutout in the aft location. The drag data indicate that, when the cutout configurations are compared, the configuration with the cutout in the aft location has the best drag characteristics. Again, the pitching-moment data indicate degraded longitudinal stability characteristics for all cutout configurations; however, a trend is shown which indicates that, the farther aft the cutout is located, the less degraded are the stability characteristics.

Surface flow visualization photographs were taken of the 30° diamond with forward cutout and the 30° diamond with aft cutout and are presented in figures 20 and 21. Photographs are presented for angles of attack of 20°, 30°, and 50° for both configurations, and in each case the flow over the aft portion of the wing appears to be separated. At angles of attack of 20° and 30°, the flow visualizations on the forward portion of the wing indicate the presence of strong vortical flows on both configurations. Thus, when the cutout is shifted aft, the configuration as a whole has the majority of its wing area in the forward vortical flow region and the minimum amount of wing area in the aft separated-flow region. This explains why greater lift coefficients are generated on the configuration with the cutout in the aft location at angles of attack of 20° and 30°. The separated flow on the aft portion of these 30° diamond cutout wings and the vortical flow region indicated on the forward portion are also noted in the flow visualization photographs of the 40° diamond cutout wings presented in figure 16. These observations explain why an aft cutout can be more beneficial than a forward cutout.

The overall results of the investigation of cutout longitudinal location indicate that, for the cutout shape that was tested, separated flow is present on the wing aft of the cutout at angles of attack of 20° and above regardless of cutout location. This condition explains why the greatest $C_{L,\max}$ is generated with the cutout in an aft location. The aft cutout location is the most beneficial for increased lift, produces less drag for a given lift coefficient, and is the least detrimental to longitudinal stability characteristics.

Part of the cutout investigation was to determine if there were any effects due to cutout shape. The 30° diamond cutout wing was modified to produce a diamond cutout shape (fig. 3(f)) with the same amount of cutout area as the 30° diamond with smallest cutout. To illustrate the effects of cutout shape, data from these two configurations are presented together for comparison in figure 22. These data indicate that the diamond cutout shape will produce 9-percent greater $C_{L,\max}$ than the triangular cutout shape. At an angle of attack of 40° and above, both cutout configurations produce essentially the same amount of lift. The drag data indicate that in the vicinity of $C_{L,\max}$ the diamond cutout configuration has

better drag characteristics than the smallest triangular cutout configuration; however, both cutout configurations have better drag characteristics than the 30° diamond wing. When comparing the longitudinal stability characteristics as indicated in the pitching-moment data, the diamond cutout shape is shown to produce a substantial improvement over the triangular cutout shape.

Because cutout shape effects were evident in the longitudinal aerodynamic data, flow visualization was conducted on the previously mentioned configurations to gain further insight. Photographs of these results are presented in figures 23 and 24. The major difference noted in the flow patterns between the 30° diamond with diamond cutout and the 30° diamond with smallest cutout is that the inboard portion of the surface flow aft of the cutout appears to be less separated and more well behaved on the diamond-shaped cutout configuration than it is on the triangular-shaped cutout configuration. This suggests a sensitivity to the direction of the sweep of the aft edge of the cutout. In other words, the photographs indicate that, if the sweep of the aft edge of the cutout is in the same direction as the wing leading edge, a more desirable surface flow condition will result on the wing aft of the cutout. This effect can be seen directly on the diamond-shaped cutout configuration when the inboard portion of the surface flow aft of the cutout is compared with the outboard portion aft of the cutout. On the inboard region aft of the cutout, the outboard-swept minitufts indicate the presence of vortical flow; however, on the outboard region aft of the cutout, separated flow is indicated. These vortical flow regions inboard on the wing and aft of the cutout explain why the 30° diamond with diamond cutout produces a greater lift coefficient than the 30° diamond with smallest cutout (triangular) at the angles of attack presented of 20° and 35°.

The final results of the cutout shape portion of the investigation indicate that cutout shape can have a significant effect on configuration longitudinal characteristics. Specifically, if the sweep of the aft edge of the cutout is in the same direction as the wing leading edge, a much less-separated and more well-behaved flow results on the wing aft of the cutout than when the aft cutout sweep is in the opposite direction of the wing leading edge. This same cutout sweep philosophy also improves the longitudinal stability characteristics. At angles of attack of 40° and above, however, the effects of variations in cutout shape were minimal.

Because of indications earlier in this investigation that wing cutouts, especially in an aft location, will improve lift characteristics, one last cutout configuration referred to as the 55° delta cutout wing (fig. 3(g)) was tested. Note that this configuration essentially has a diamond planform shape, and a diamond planform will generally have a lower $C_{L,\max}$ than a delta wing with the same leading-edge sweep. However, the 55° delta cutout wing was still expected to produce a greater $C_{L,\max}$ than the 55° delta wing. The data presented in figure 25 show that the cutout configuration produces reduced lift coefficients when compared with the 55° delta wing across essentially the entire angle-of-attack range. The lift improvement present at 0° angle of attack is most likely due to an unintentional cambering effect resulting from the modification of the original 30° diamond cutout wing. In addition, the longitudinal stability characteristics are slightly degraded because of the cutout as indicated by the pitching-moment data.

Flow visualization was conducted at angles of attack of 20°, 25°, 35°, and 50° for the 55° delta cutout wing configuration, and photographs illustrating these flow conditions are presented in figure 26. These photographs indicate that the cutout effects are similar to previous observations that the surface flow over the wing aft of the cutout is separated at all of the angles of attack presented. The flow over the entire planform is separated at angles of attack of 35° and 50°, as expected from the data in figure 25. When flow visualization photographs of the 55° delta cutout wing at angles of attack of 20° (fig. 26(a)) and 25° (fig. 26(b)) are compared with those of the 55° delta wing (figs. 13(a) and 13(b) respectively), little difference is observed in the surface flow patterns in the region forward of the cutout.

The reason that the cutout is not effective on the 55° delta wing, while it is effective in improving lift on the 30° diamond configurations, may be due to the leading-edge sweep. In general, the vortex generated by a swept wing leading edge will be positioned on the configuration at an angle greater than the wing sweep angle. This holds true for all angles of attack where vortices exist and can be seen by noting the orientation of the minitufts in each delta or diamond planform flow visualization photograph that has been presented so far. For example, note the flow visualization photographs presented for the 30° diamond cutout configurations at 20° angle of attack in figures 20(a), 21(a), and 24(a). In each case the minitufts on the wing just aft of the leading edge are swept outboard essentially parallel to the wing leading edge. This indicates that the wing vortex cores, which originate at the junction of the wing leading edge and the forebody, are also swept outboard considerably. Specifically, these wing vortex cores are swept back at an angle slightly greater than the wing leading-edge sweep angle but not enough to pass over the cutout region. Thus, as the wing vortices flow aft, they ultimately pass outboard of the cutouts on the 30° diamond cutout configurations.

When observing the flow visualization photograph taken of the 55° delta cutout wing (fig. 26(a)) at 20°

angle of attack, the orientation of the minitufts indicates that the vortices, which originate from the apex, are swept farther aft than the wing vortices on the 30° diamond cutout configurations. As noted previously, the vortex cores are swept back at an angle slightly greater than the wing leading-edge sweep angle. Therefore, because the minitufts on the 55° delta cutout wing at 20° angle of attack (fig. 26(a)) are swept farther aft than those on the 30° diamond cutout configurations, and the vortices on the 55° delta cutout wing originate farther inboard than the wing vortices on the 30° diamond cutout configurations, the vortices on the 55° delta cutout wing appear to flow into the cutout region. This interaction of the leading-edge vortices with the cutout regions may cause the adverse lift effects noted in the data in figure 25. Thus, the cutout area on the 55° delta cutout wing was most likely an area on the noncutout configuration that was effectively generating lift because of the positive influence of the vortices (i.e., generating a low pressure region) on the upper surface.

In general, the results of the 55° delta cutout wing tests indicate that the effectiveness of a wing cutout can depend on the leading-edge sweep of the wing. Specifically, when the wing leading-edge sweep is on the order of 30° to 40°, the wing leading-edge vortex influence will tend to be outboard of the cutout and suggests a beneficial surface flow condition. When the wing leading-edge sweep is on the order of 55°, the leading-edge vortex may interact with the cutout, which results in a less desirable flow condition. Also, note that the 30° and 40° diamond cutout wing configurations had a forebody, while the 55° delta configurations did not. Thus, the presence of the forebody and forebody vortices may account for some of the improved cutout performance on the 30° and 40° diamond wing configurations.

Serrated Forebodies

The final test phase was the investigation of the effect of serrated forebodies. As mentioned earlier, a vortex would likely form off the leading edge of each forebody serration such that multiple vortices would extend over the length of the configuration. These multiple vortices were in turn expected to enhance the lift generating capability at moderate to high angles of attack. The first configuration that was tested is referred to as the "65° delta with delta sawteeth." This configuration consisted of a forebody with 65° swept sawteeth added to the 65° delta wing configuration as shown in figure 3(h). In addition, two serrated forebodies were examined on the 40° diamond wing in the form of a diamond sawtooth arrangement as illustrated in figures 3(i) and 3(j).

Longitudinal data illustrating the effect of each serrated forebody configuration are presented in figure 27. The 65° delta with delta sawteeth planform produces a slightly greater $C_{L,\max}$ but with a more abrupt stall than the 65° delta wing. At angles of attack from 50° to 70°, the 65° delta with delta sawteeth planform demonstrates better lift characteristics than the 65° delta wing.

When the diamond sawtooth forebody planforms are compared with the original 40° diamond wing, a significant lift improvement is noted for both diamond sawtooth configurations. An 18-percent increase in $C_{L,\max}$ is shown for the 40° diamond with 6 diamond sawteeth, and a 25-percent increase in $C_{L,\max}$ is shown for the 40° diamond with 3 diamond sawteeth. In addition, lift characteristics of the diamond sawtooth planforms are improved over the original 40° diamond wing across the entire angle-of-attack range covered. Generally, drag was reduced for a given C_L with the addition of sawteeth on all configurations for angles of attack up to $C_{L,\max}$.

When longitudinal stability characteristics are compared, the pitching-moment data indicate that the addition of the delta sawtooth forebody to the 65° delta wing has a significant degrading effect. The addition of the diamond sawtooth forebodies to the 40° diamond wing also has a degrading effect on the longitudinal stability characteristics; however, the effect is much less than that on the 65° delta with delta sawteeth planform. This degradation of the longitudinal stability characteristics is likely the result of the additional surface area that has been placed well forward of the moment reference center.

Flow visualization studies were conducted on the 40° diamond with 3 diamond sawteeth configuration, and photographs illustrating the surface flow conditions are presented in figure 28. A vortex was expected to form along the leading edge of each sawtooth such that multiple vortices would be distributed across the top of the configuration. In turn, this energized flow was expected to improve lift characteristics, especially beyond stall; further more, the multiple vortices could be anticipated to stabilize the flow field at high angles of attack. The flow visualization photographs in figure 28 at angles of attack of 20° and 35° indicate the anticipated vortical flow conditions on the second and third sawteeth back from the nose of the configuration and on the diamond wing. Thus, the expected effects were produced; however, separated flow was not expected to be present over the first sawtooth as indicated at all angles of attack presented. A greater sweep angle on the first sawtooth might have been more effective; however, this was not investigated in the test. At an angle of attack of 50°, the surface flow is extremely well behaved, much more so than on any of the other configurations tested. This explains why the lift was greater than that of the original 40° diamond wing. If the flow visualization photographs of the 40°

diamond wing (fig. 8) are compared with those of the 40° diamond with 3 diamond sawteeth (fig. 28), a less-separated, more-well-behaved surface flow is indicated on the main wing of the sawtooth configuration at all angles of attack. Thus, the vortices produced by the sawtooth forebody improve the surface flow conditions over the length of the configuration and thereby improve the lift-generating characteristics across the angle-of-attack range.

The results of the serrated forebody studies overwhelmingly indicate that substantial lift increases can be generated across the angle-of-attack range with a sawtooth forebody arrangement. The data further indicate that more sawteeth do not necessarily produce additional increases in $C_{L,\,max}$. The effects of a serrated forebody can degrade the longitudinal stability characteristics; however, for the diamond sawtooth configurations these characteristics were not overly degraded.

Summary of Results

The results of an investigation of the longitudinal aerodynamic characteristics of 21 different planforms tested in the Langley Subsonic Basic Research Tunnel (SBRT) are summarized as follows:

1. Twin-body planforms do not cause any detrimental effects at subsonic conditions.

2. Double-wing planforms increase lift and improve longitudinal stability characteristics.

3. a. Cutout wing configurations generate favorable lift characteristics; however, a smaller cutout is generally more effective than a larger one.

   b. An aft cutout location is more favorable than a forward location in terms of both lift and longitudinal stability characteristics.

   c. Cutout shapes produce increased effectiveness if the sweep of the aft edge of the cutout is in the same direction as the wing leading-edge sweep.

   d. The interaction of the wing leading-edge vortex with a wing cutout can be detrimental. Therefore, because wing leading-edge sweep determines the vortex location, wing leading-edge sweep can have a significant effect on the performance of a cutout configuration.

4. Serrated forebodies generate substantial lift increases at angles of attack up to 70°. A diamond sawtooth forebody planform produces a 25-percent increase in $C_{L,\,max}$. However, an increase in the number of serrations does not necessarily improve lift performance.

NASA Langley Research Center
Hampton, VA 23681-0001
May 22, 1995

References

1. Chambers, Joseph R.: High-Angle-of-Attack Technology—Progress and Challenges. *High-Angle-of-Attack Technology*, Volume I, Joseph R. Chambers, William P. Gilbert, and Luat T. Nguyen, eds., NASA CP-3149, Part 1, 1992, pp. 1–22.

2. Murri, Daniel G.; Biedron, Robert T.; Erickson, Gary E.; Jordon, Frank L., Jr.; and Hoffler, Keith D.: Development of Actuated Forebody Strake Controls for the F-18 High-Alpha Research Vehicle. *High-Angle-of-Attack Technology*, Volume I, Joseph R. Chambers, William P. Gilbert, and Luat T. Nguyen, eds., NASA CP-3149, Part 1, 1992, pp. 335–380.

3. Erickson, Gary E.; and Murri, Daniel G.: Forebody Strakes for High-Angle-of-Attack Vortex Flow Control: Mach Number and Strake Planform Effects. *High-Angle-of-Attack Technology*, Volume I, Joseph R. Chambers, William P. Gilbert, and Luat T. Nguyen, eds., NASA CP-3149, Part 1, 1992, pp. 381–480.

4. Murri, Daniel G.; Rao, Dhanvada M.: Exploratory Studies of Actuated Forebody Strakes for Yaw Control at High Angles of Attack. AIAA-87-2557, Aug. 1987.

5. Malcolm, Gerald N.; Ng, T. Terry; Lewis, Liane C.; and Murri, Daniel G.: Development of Non-Conventional Control Methods for High Angle of Attack Flight Using Vortex Manipulation. *Technical Papers—7th AIAA Applied Aerodynamics Conference*, 1989, pp. 249–267. (Available as AIAA-89-2192.)

6. Ng, T. Terry; and Malcolm, Gerald N.: Aerodynamic Control Using Forebody Vortex Control. *High-Angle-of-Attack Technology*, Volume I, Joseph R. Chambers, William P. Gilbert, and Luat T. Nguyen, eds., NASA CP-3149, Part 1, 1992, pp. 507–531.

7. Ng, T. Terry; and Malcolm, Gerald N.: Aerodynamic Control Using Forebody Blowing and Suction. AIAA-91-0619, Jan. 1991.

8. White, E. Richard: Effects of Suction on High-Angle-of-Attack Directional Control Characteristics of Isolated Forebodies. *High-Angle-of-Attack Technology*, Volume I, Joseph R. Chambers, William P. Gilbert, and Luat T. Nguyen, eds., NASA CP-3149, Part 1, 1992, pp. 533–556.

9. Schreiner, John A.; Erickson, Gary E.; and Guyton, Robert W.: Application of Tangential Sheet Blowing on the Forebody of an F-18-Like Configuration for High-Angle-of-Attack Maneuverability. *High-Angle-of-Attack Technology*, Volume II, Joseph R. Chambers, William P. Gilbert, and Luat T. Nguyen, eds., NASA CP-3150, 1992, pp. 1–25.

10. Roberts, Leonard; Tavella, Domingo A.; and Celik, Zeki: Controlled Vortex Flows Over Forebodies and Wings. *High-Angle-of-Attack Technology*, Volume I, Joseph R. Chambers, William P. Gilbert, and Luat T. Nguyen, eds., NASA CP-3149, Part 2, 1992, pp. 659–671.

11. Bauer, Steven X. S.; and Hemsch, Michael J.: Alleviation of Side Force on Tangent-Ogive Forebodies Using Passive Porosity. AIAA-92-2711, June 1992.

12. Wood, Richard M.; Banks, Daniel W.; and Bauer, Steven X. S.: Assessment of Passive Porosity With Free and Fixed Separation on a Tangent Ogive Forebody. AIAA-92-4494, Aug. 1992.

13. Modi, V. J.; and Stewart, A. C.: Approach to Side Force Alleviation Through Modification of the Pointed Forebody Geometry. *Technical Papers—AIAA Atmospheric Flight Mechanics Conference*, 1990, pp. 349–358. (Available as AIAA-90-2834.)

14. Gunston, Bill; and Spick, Mike: *Modern Air Combat: The Aircraft, Tactics and Weapons Employed in Aerial Warfare Today.* Crescent Books, 1983.

15. Gunston, Bill; Peacock, Lindsay; Bunce, Derek; and Bunce, Patrick: *Fighter Missions.* Orion Books, 1989.

16. Gloss, B. B.: *Effect of Wing Planform and Canard Location and Geometry on the Longitudinal Aerodynamic Characteristics of a Close-Coupled Canard Wing Model at Subsonic Speeds.* NASA TN D-7910, 1975.

17. Yip, L. P.; and Paulson, John W., Jr.: *Effects of Deflected Thrust on the Longitudinal Aerodynamic Characteristics of a Close-Coupled Wing-Canard Configuration.* NASA TP-1090, 1977.

18. Paulson, John W., Jr.; and Thomas, James L.: *Summary of Low-Speed Longitudinal Aerodynamics of Two Powered Close-Coupled Wing-Canard Fighter Configurations.* NASA TP-1535, 1979.

19. Kruse, R. L.; Lovette, G. H.; and Spencer, B., Jr.: *Reynolds Number Effects on the Aerodynamic Characteristics of Irregular Planform Wings at Mach Number 0.3.* NASA TM X-73132, 1977.

20. Wood, Richard M.; and Miller, David S.: *Wing Planform Effects at Supersonic Speeds for an Advanced Fighter Configuration.* NASA TP-2269, 1984.

21. McMillin, Naomi; and Wood, Richard M.: *Planform Effects on the Supersonic Aerodynamics of Multibody Configurations.* NASA TP-2762, 1987.

22. Yang, Wen-Jei, ed.: *Handbook of Flow Visualization.* Hemisphere Publ. Corp., 1989.

23. Crowder, J. P.: Fluorescent Minitufts for Flow Visualization on Rotating Surfaces. *Flow Visualization III—Proceedings of the Third International Symposium on Flow Visualization*, W. J. Yang, ed., Hemisphere Publ. Corp., 1985, pp. 55–59.

24. Graves, T. V.; Nelson, Robert C.; Schwimley, S. L.; and Ely, W. L.: Aerodynamic Performance of Strake Wing Configurations. *High-Angle-of-Attack Technology*, Volume I, Joseph R. Chambers, William P. Gilbert, and Luat T. Nguyen, eds., NASA CP-3149, Part 1, 1992, pp. 173–204.

25. Lamar, J. E.; and Campbell, J. F.: Recent Studies at NASA-Langley of Vortical Flows Interacting With Neighboring Surfaces. *Aerodynamics of Vortical Type Flows in Three Dimensions*, AGARD-CP-342, July 1983, pp. 10-1–10-32. (Available from DTIC as AD A135 157.)

26. Hemsch, Michael J.; and Luckring, James M.: Connection Between Leading-Edge Sweep, Vortex Lift, and Vortex Strength for Delta Wings. *J. Aircr.*, vol. 27, no. 5, May 1990, pp. 473–475.

27. Etkin, Bernard: *Dynamics of Flight—Stability and Control*, Second ed. John Wiley & Sons, Inc., 1982.

Table I. Reference Planform Geometric Characteristics and Figure Numbers

No.	Planform description	S, ft^2	c, in.	b, in.	Force and moment data figure no.	Flow visualization figure no.
1	55° delta wing	0.3236	8.16	11.42	12, 25	13
2	65° delta wing	0.3236	10.00	9.32	27	Not obtained
3	30° diamond wing	0.3140	11.90	11.80	6, 9, 15, 17, 18, 19, 22	7
4	40° diamond wing	0.3565	13.67	10.52	6, 12, 15, 17, 27	8
5	47.5° diamond with wide forebody	0.2702	11.30	8.00	12	Not obtained
6	60° double arrow	0.3067	14.96	7.36	9	11

Table II. Alternate Planform Geometric Characteristics and Figure Numbers

No.	Planform description	S, ft^2	c, in.	b, in.	Force and moment data figure no.	Flow visualization figure no.
7	30° diamond wing with twin body	0.3421	11.33	11.80	6	Not obtained
8	40° diamond wing with twin body	0.3783	12.38	10.52	6	Not obtained
9	30° diamond cutout wing	0.2626	11.90	11.80	15, 18	Not obtained
10	40° diamond cutout wing	0.3200	13.67	10.52	15, 17	16
11	30° diamond twin wing	0.2942	12.89	8.34	9	10
12*	55° delta with trailing-edge serrations	0.4338	14.44	11.42	12	14
13*	30° diamond with forward cutout	0.2819	11.90	11.80	19	20
14*	30° diamond with aft cutout	0.2819	11.90	11.80	19	21
15*	30° diamond with reduced cutout	0.2819	11.90	11.80	17, 18, 19	Not obtained
16*	30° diamond with smallest cutout	0.2909	11.90	11.80	18, 22	24
17*	30° diamond with diamond cutout	0.2909	11.90	11.80	22	23
18*	55° delta cutout wing	0.4362	11.90	11.80	25	26
19*	65° delta with delta sawteeth	0.3696	13.56	9.32	27	Not obtained
20*	40° diamond with 6 diamond sawteeth	0.3781	13.67	10.52	27	Not obtained
21*	40° diamond with 3 diamond sawteeth	0.3998	13.67	10.52	27	28

*Modified planforms.

Table III. Force and Moment Coefficients for All Planform Models

(a) 55° delta wing; X_{ref} = 4.45 in.

α, deg	C_L	C_D	C_m
0	0.03500	0.03400	0.00091
10	.58100	.16500	.00091
20	1.00100	.45300	−.00055
25	1.09300	.61100	−.00932
30	.89500	.62600	−.07057
35	.81900	.70800	−.08548
40	.79600	.81500	−.09382
50	.71800	1.04400	−.11264
60	.59000	1.27700	−.13815
70	.36700	1.39400	−.15771

(b) 65° delta wing; X_{ref} = 5.77 in.

α, deg	C_L	C_D	C_m
0	0.02000	0.03400	0.00215
10	.48900	.13600	.00215
20	.96400	.42900	.01987
25	1.15800	.63300	.02309
30	1.26100	.83800	.02390
35	1.25900	1.01200	.01578
40	1.13000	1.09200	−.02778
50	.75300	1.07800	−.07846
60	.58500	1.26200	−.09440
70	.37100	1.40300	−.11320

(c) 30° diamond wing; X_{ref} = 6.89 in.

α, deg	C_L	C_D	C_m
0	−0.04613	0.02307	0.01681
10	.36819	.10735	.01681
20	.67605	.31939	.02577
25	.74347	.42940	.02022
30	.78074	.53853	.01287
35	.79404	.65742	.00393
40	.72662	.71331	−.00143
50	.61306	.85437	−.02658
60	.50837	1.03359	−.05870
70	.36730	1.18352	−.07756

Table III. Continued

(d) 40° diamond wing; X_{ref} = 7.33 in.

α, deg	C_L	C_D	C_m
0	–0.05798	0.01993	0.01575
10	.34424	.09421	.01575
20	.65950	.29261	.01195
25	.73921	.41037	.00532
30	.82799	.54988	–.00171
35	.86966	.68395	–.01091
40	.80263	.75099	–.01292
50	.65497	.88144	–.04451
60	.54354	1.05719	–.07215
70	.39316	1.21481	–.09214

(e) 47.5° diamond with wide forebody; X_{ref} = 4.96 in.

α, deg	C_L	C_D	C_m
0	–0.07274	0.00988	0.02092
10	.29993	.07453	.02092
20	.70224	.29814	.01579
25	.90967	.46606	.00404
30	.95547	.60166	–.00313
35	.97253	.72738	–.01571
40	.90339	.81718	–.03150
50	.68068	.88363	–.08377
60	.52533	.99947	–.09282
70	.40141	1.12250	–.11119

(f) 60° double arrow; X_{ref} = 7.55 in.

α, deg	C_L	C_D	C_m
0	–0.03644	0.01913	0.01285
10	.24597	.06924	.01285
20	.60126	.26875	.00597
25	.78619	.42817	.00237
30	.92922	.61493	–.00587
35	.99937	.78710	–.01920
40	.98479	.92740	–.03143
50	.80168	1.06131	–.06184
60	.61219	1.16608	–.10625
70	.43728	1.34373	–.13827

Table III. Continued

(g) 30° diamond wing with twin body; X_{ref} = 6.08 in.

α, deg	C_L	C_D	C_m
0	−0.08039	0.02274	0.02163
10	.33942	.10150	.02163
20	.67315	.30288	.03370
25	.80956	.45147	.02873
30	.81525	.54729	.01793
35	.82256	.66503	.00862
40	.76734	.74298	−.00186
50	.67071	.91106	−.03858
60	.56109	1.10676	−.06366
70	.40356	1.27565	−.08214

(h) 40° diamond wing with twin body; X_{ref} = 6.29 in.

α, deg	C_L	C_D	C_m
0	−0.07768	0.02617	0.02122
10	.30395	.09118	.02122
20	.64505	.27777	.01973
25	.77085	.41033	.01499
30	.80968	.52600	.00574
35	.83923	.65518	−.00205
40	.78267	.73201	−.01980
50	.68304	.90340	−.05110
60	.56990	1.09590	−.08133
70	.40949	1.26223	−.10260

(i) 30° diamond cutout wing; X_{ref} = 6.57 in.

α, deg	C_L	C_D	C_m
0	0.07730	0.06324	−0.00963
10	.30656	.15460	−.00963
20	.52880	.31974	−.00300
25	.66231	.44096	−.00067
30	.75806	.57799	.00231
35	.75367	.68691	.00401
40	.73698	.77826	−.00098
50	.63069	.92320	−.02753
60	.52792	1.09888	−.06221
70	.38737	1.25699	−.10173

Table III. Continued

(j) 40° diamond cutout wing; X_{ref} = 7.48 in.

α, deg	C_L	C_D	C_m
0	–0.03401	0.02864	0.00513
10	.33652	.10740	.00513
20	.59965	.28461	.02101
25	.81534	.45197	.02445
30	.86367	.57548	.02023
35	.87352	.69094	.01766
40	.87441	.82429	.01135
50	.71153	.95407	–.01812
60	.58622	1.13576	–.05621
70	.41796	1.29596	–.07404

(k) 30° diamond twin wing; X_{ref} = 7.00 in.

α, deg	C_L	C_D	C_m
0	–0.05102	0.04046	0.01850
10	.27707	.08884	.01850
20	.68697	.30698	.01476
25	.87872	.47762	.00811
30	.97548	.63683	.00267
35	.99043	.76613	–.00345
40	.92006	.87080	–.01262
50	.66938	.90775	–.02780
60	.56734	1.12061	–.08104
70	.39670	1.25695	–.09782

(l) 55° delta with trailing-edge serrations; X_{ref} = 9.14 in.

α, deg	C_L	C_D	C_m
0	–0.05300	0.02200	0.01317
10	.47700	.10700	.01317
20	.83900	.34900	.03727
25	.96200	.49500	.03798
30	1.04000	.66200	.03621
35	1.04200	.79900	.03173
40	.94800	.86200	.02242
50	.81100	1.03600	.00869
60	.67700	1.25100	–.03949
70	.50500	1.45200	–.05863

Table III. Continued

(m) 30° diamond with forward cutout; X_{ref} = 7.37 in.

α, deg	C_L	C_D	C_m
0	0.11600	0.05800	–0.00671
10	.44400	.17300	–.00671
20	.65200	.35400	.01867
25	.75300	.47600	.03541
30	.81200	.60600	.04131
35	.82600	.71500	.04845
40	.80800	.82100	.04514
50	.64900	.94400	.03208
60	.51500	1.09800	–.00323
70	.37300	1.24600	–.01817

(n) 30° diamond with aft cutout; X_{ref} = 6.98 in.

α, deg	C_L	C_D	C_m
0	0.06200	0.06400	–0.00897
10	.45300	.15300	–.00897
20	.71900	.33900	.01256
25	.80000	.45600	.02587
30	.87900	.60400	.02685
35	.84600	.68400	.02409
40	.76700	.76900	.01631
50	.63400	.90700	.00455
60	.52100	1.06200	–.03431
70	.37100	1.20200	–.05937

(o) 30° diamond with reduced cutout; X_{ref} = 6.98 in.

α, deg	C_L	C_D	C_m
0	0.12400	0.07100	–0.01958
10	.46400	.16600	–.01958
20	.65300	.34200	.00417
25	.76200	.45600	.01251
30	.81100	.57500	.01543
35	.82300	.69900	.01890
40	.78000	.79600	.01231
50	.62600	.91900	.00153
60	.52300	1.07700	–.03379
70	.38000	1.22800	–.05691

Table III. Continued

(p) 30° diamond with smallest cutout; X_{ref} = 7.14 in.

α, deg	C_L	C_D	C_m
0	0.08700	0.05900	−0.01137
10	.50800	.15400	−.01137
20	.70800	.32900	.01448
25	.79900	.45200	.02836
30	.85600	.56900	.02853
35	.86200	.69800	.02604
40	.80800	.78700	.01949
50	.65900	.91600	.01022
60	.53200	1.06500	−.01422
70	.38700	1.21300	−.03773

(q) 30° diamond with diamond cutout; X_{ref} = 6.86 in.

α, deg	C_L	C_D	C_m
0	0.13500	0.06600	−0.01386
10	.43000	.14600	−.01386
20	.78200	.36400	−.00698
25	.91700	.50900	−.00137
30	.94000	.63100	.00092
35	.88500	.71400	−.00460
40	.79900	.77900	−.00769
50	.64800	.89700	−.01563
60	.53800	1.07500	−.05797
70	.38500	1.20400	−.07391

(r) 55° delta cutout wing; X_{ref} = 5.05 in.

α, deg	C_L	C_D	C_m
0	0.10900	0.04000	−0.00500
10	.53700	.14300	−.00500
20	.74600	.35100	.01064
25	.84600	.49200	.01345
30	.83400	.59100	−.00655
35	.78200	.67400	−.03632
40	.74700	.77000	−.05078
50	.61100	.91300	−.06753
60	.51300	1.11700	−.09498
70	.36200	1.32500	−.14205

Table III. Concluded

(s) 65° delta with delta sawteeth; X_{ref} = 8.83 in.

α, deg	C_L	C_D	C_m
0	0.02200	0.02700	0.00245
10	.45600	.11200	.00245
20	.97800	.41100	.01697
25	1.21900	.63600	.03028
30	1.29400	.83400	.05479
35	1.17100	.93000	.08127
40	1.08400	1.02500	.08503
50	.85000	1.16000	.07809
60	.65900	1.31500	−.01066
70	.44200	1.47800	−.01901

(t) 40° diamond with 6 diamond sawteeth; X_{ref} = 7.02 in.

α, deg	C_L	C_D	C_m
0	−0.04600	0.02500	0.01684
10	.33600	.09200	.01684
20	.78100	.31300	.02002
25	.96800	.48900	.01828
30	1.02500	.62600	.02382
35	.98500	.73200	.02242
40	.91500	.82100	.02258
50	.75200	.97200	.00410
60	.57100	1.11000	−.05699
70	.41300	1.29700	−.07596

(u) 40° diamond with 3 diamond sawteeth; X_{ref} = 6.61 in.

α, deg	C_L	C_D	C_m
0	−0.05200	0.03000	0.02049
10	.31900	.09500	.02049
20	.76400	.30600	.01634
25	.97300	.48300	.01395
30	1.09100	.66700	.02189
35	1.07200	.78800	.02883
40	1.00500	.89600	.03175
50	.77600	1.01900	−.00076
60	.58900	1.15200	−.06456
70	.42400	1.32430	−.07929

Table IV. Correlation Coefficients Derived From Linear Regression of Pitching-Moment Data

Planform description	Correlation coefficient
47.5° diamond with wide forebody	0.95
55° delta wing	0.95
40° diamond wing	0.95
40° diamond wing with twin body	0.94
60° double arrow	0.94
30° diamond twin wing	0.92
30° diamond wing with twin body	0.90
30° diamond wing	0.90
55° delta cutout wing	0.90
65° delta wing	0.83
40° diamond with 6 diamond sawteeth	0.77
40° diamond with 3 diamond sawteeth	0.77
30° diamond cutout wing	0.75
40° diamond cutout wing	0.75
30° diamond with diamond cutout	0.71
55° delta with trailing-edge serrations	0.70
30° diamond with aft cutout	0.51
30° diamond with reduced cutout	0.39
30° diamond with smallest cutout	0.30
30° diamond with forward cutout	0 .05
65° delta with delta sawteeth	≈0

Table V. Maximum Loads and Accuracy of SWT-01 Balance at Free-Stream Dynamic Pressure of 30 psf

Balance component	Maximum load	Maximum load error	Maximum coefficient error
Normal force, lb	150	±0.45	±0.0571
Axial force, lb	30	±0.09	±0.0114
Pitching moment, in-lb	225	±0.68	±0.0085

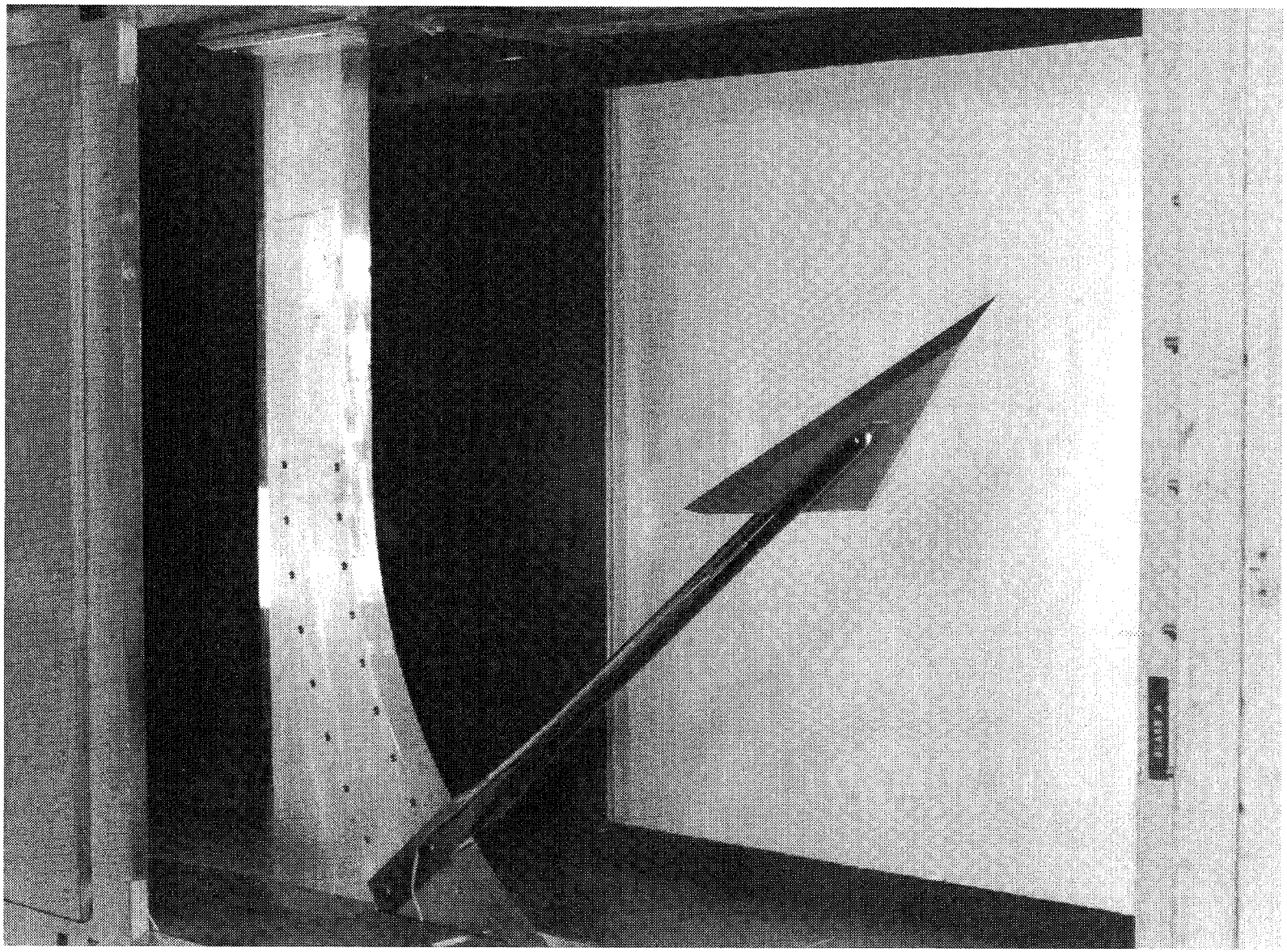

L-92-05547

Figure 1. Installation of 65° delta wing planform model in Subsonic Basic Research Tunnel.

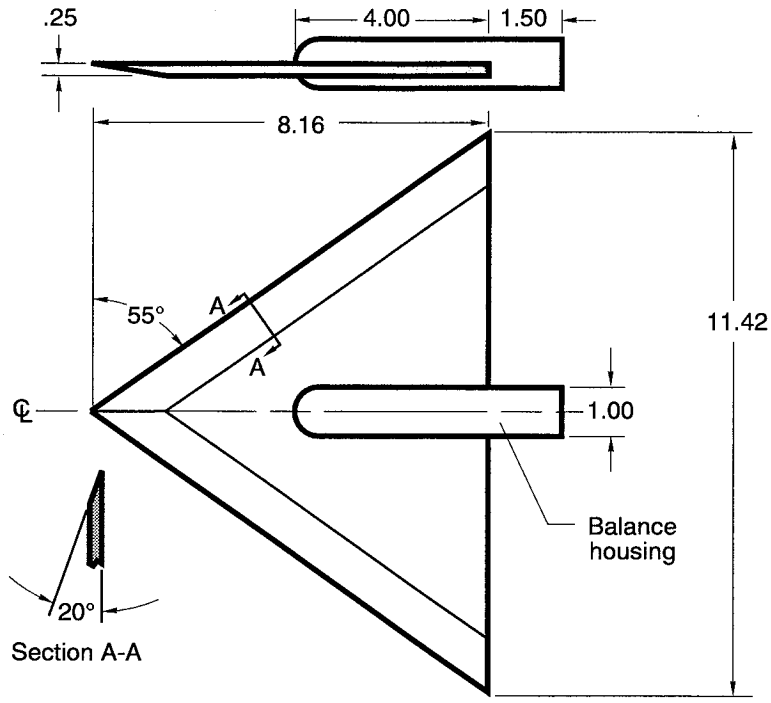

(a) 55° delta wing.

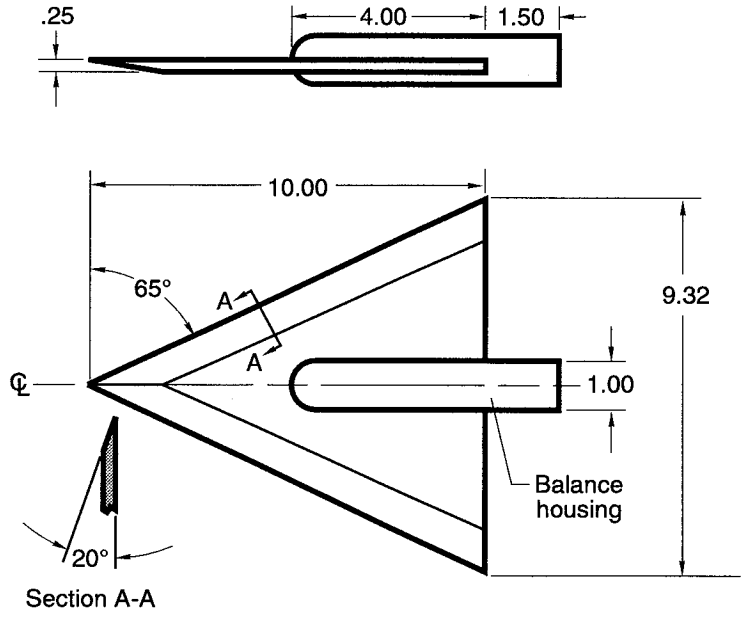

(b) 65° delta wing.

Figure 2. Side and bottom views of original 11 planform models. All linear dimensions are in inches.

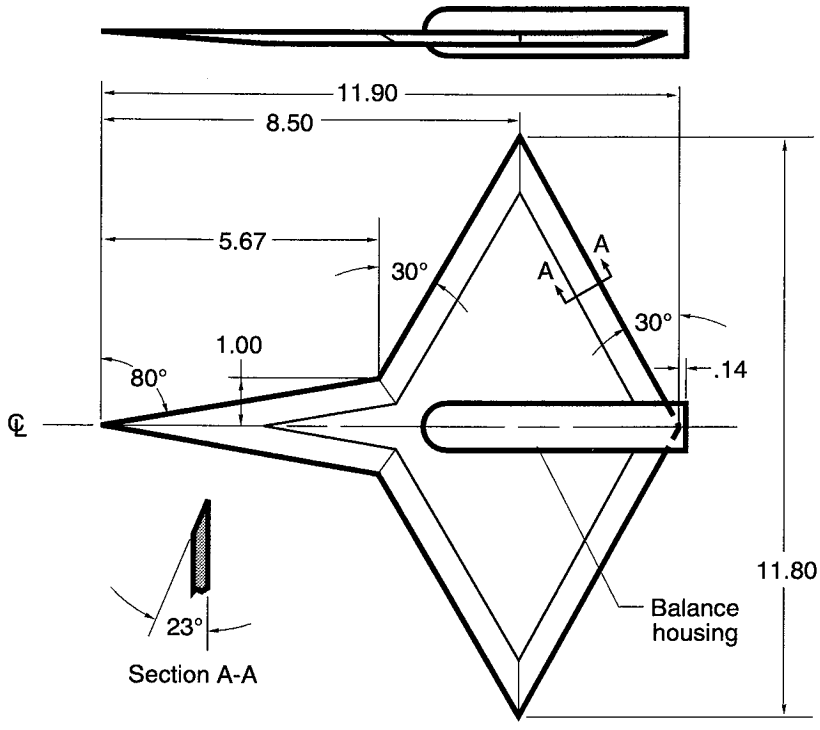

(c) 30° diamond wing.

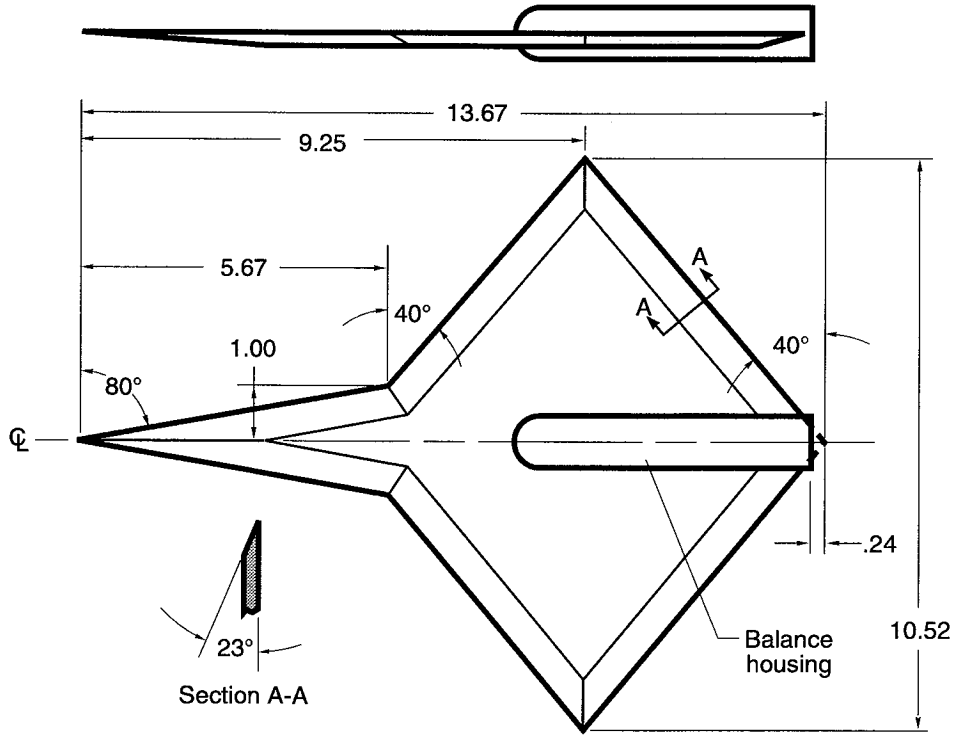

(d) 40° diamond wing.

Figure 2. Continued.

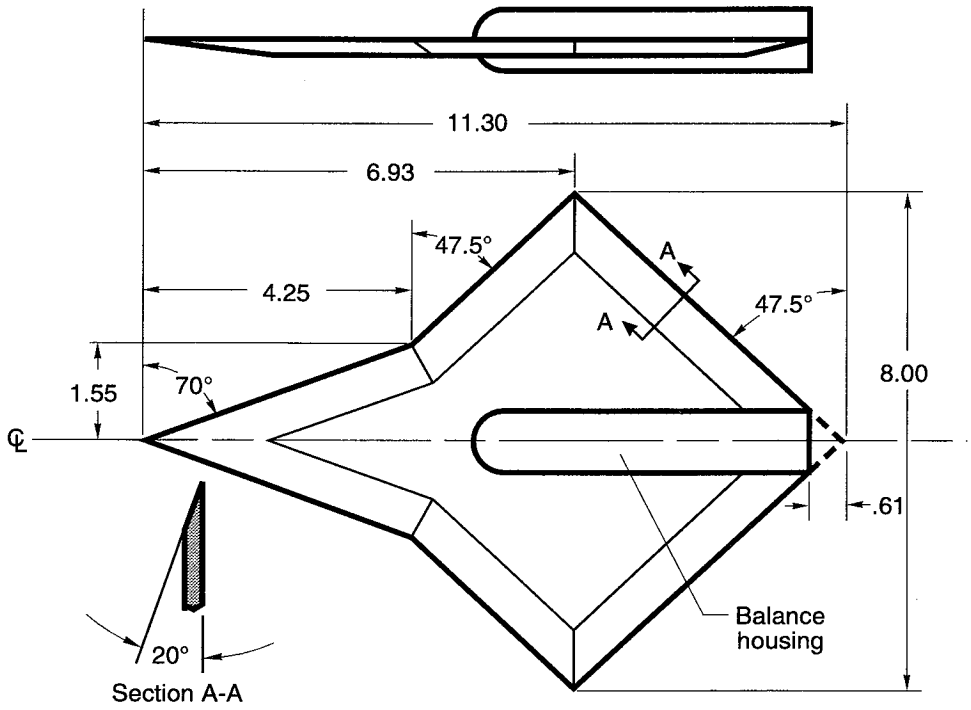

(e) 47.5° diamond with wide forebody.

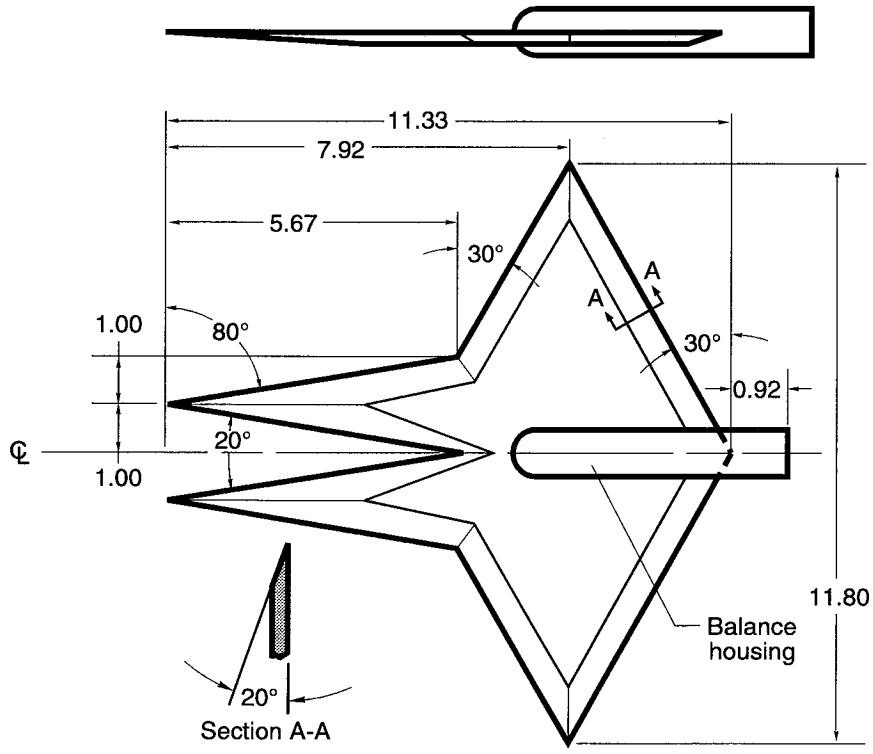

(f) 30° diamond wing with twin body.

Figure 2. Continued.

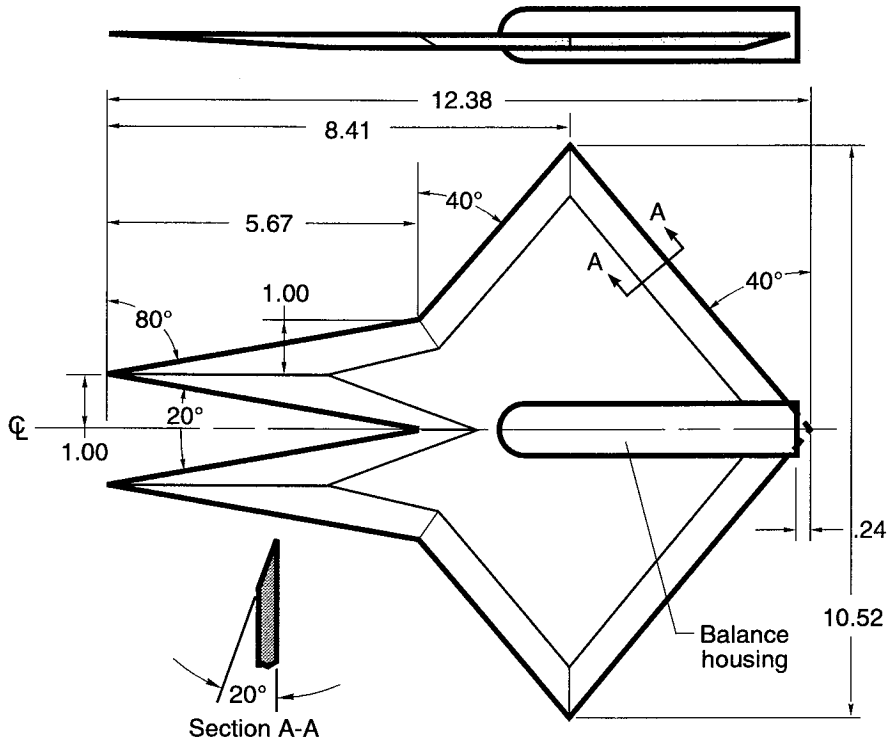

(g) 40° diamond wing with twin body.

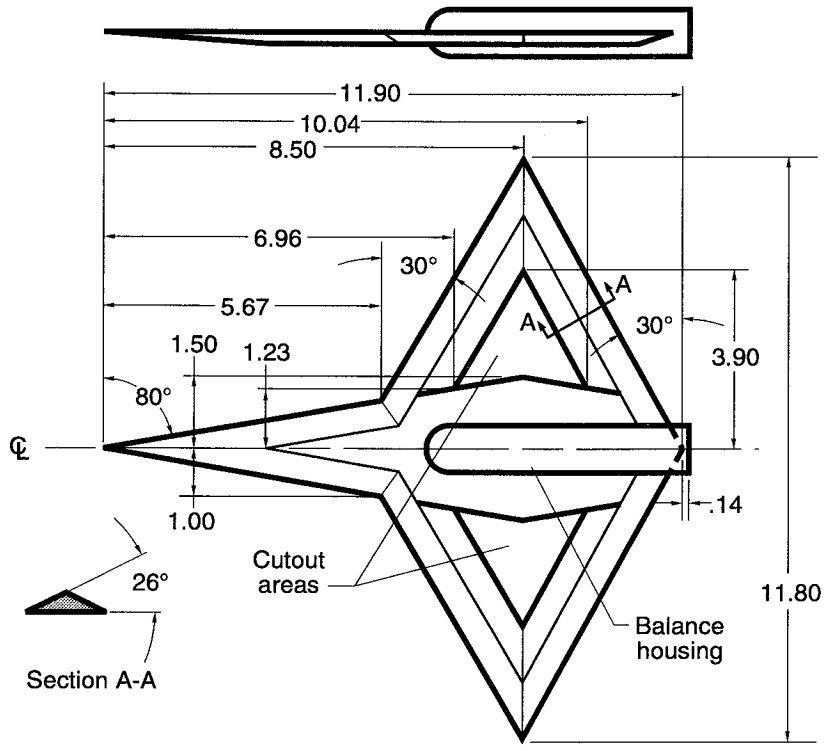

(h) 30° diamond cutout wing.

Figure 2. Continued.

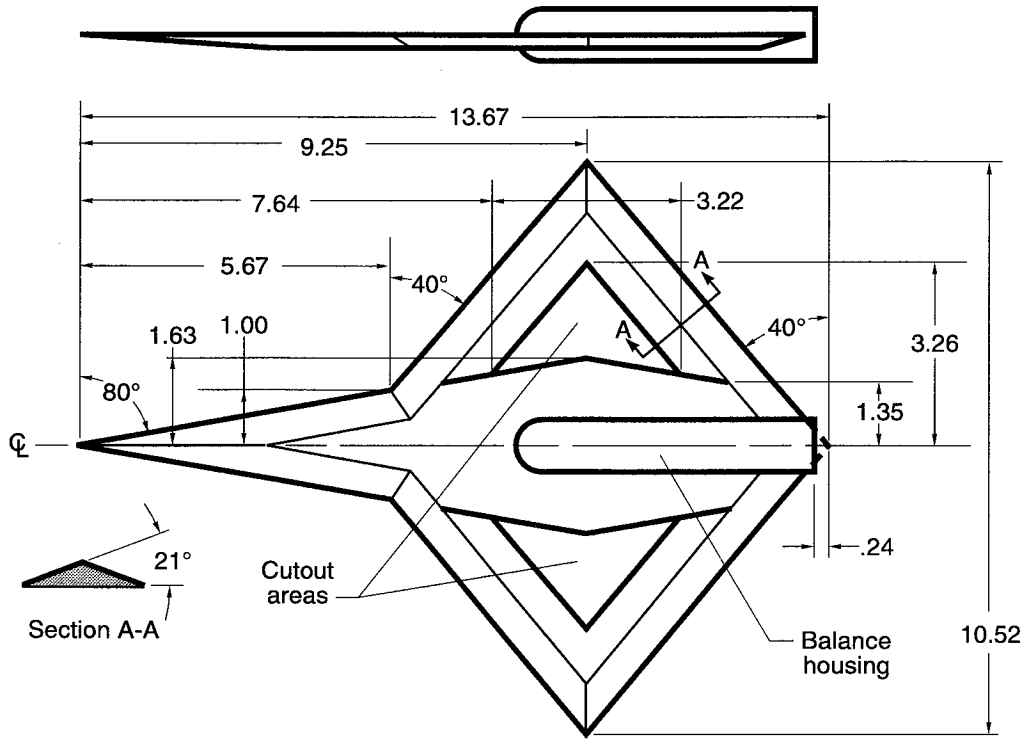

(i) 40° diamond cutout wing.

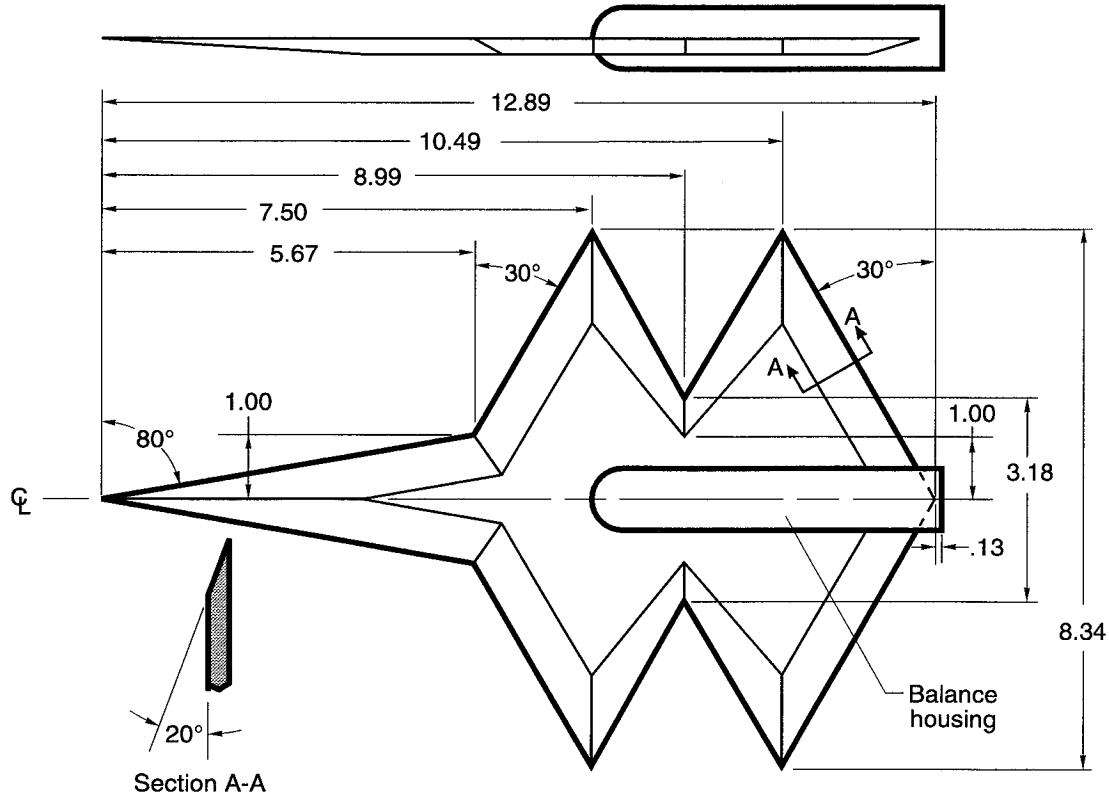

(j) 30° diamond twin wing.

Figure 2. Continued.

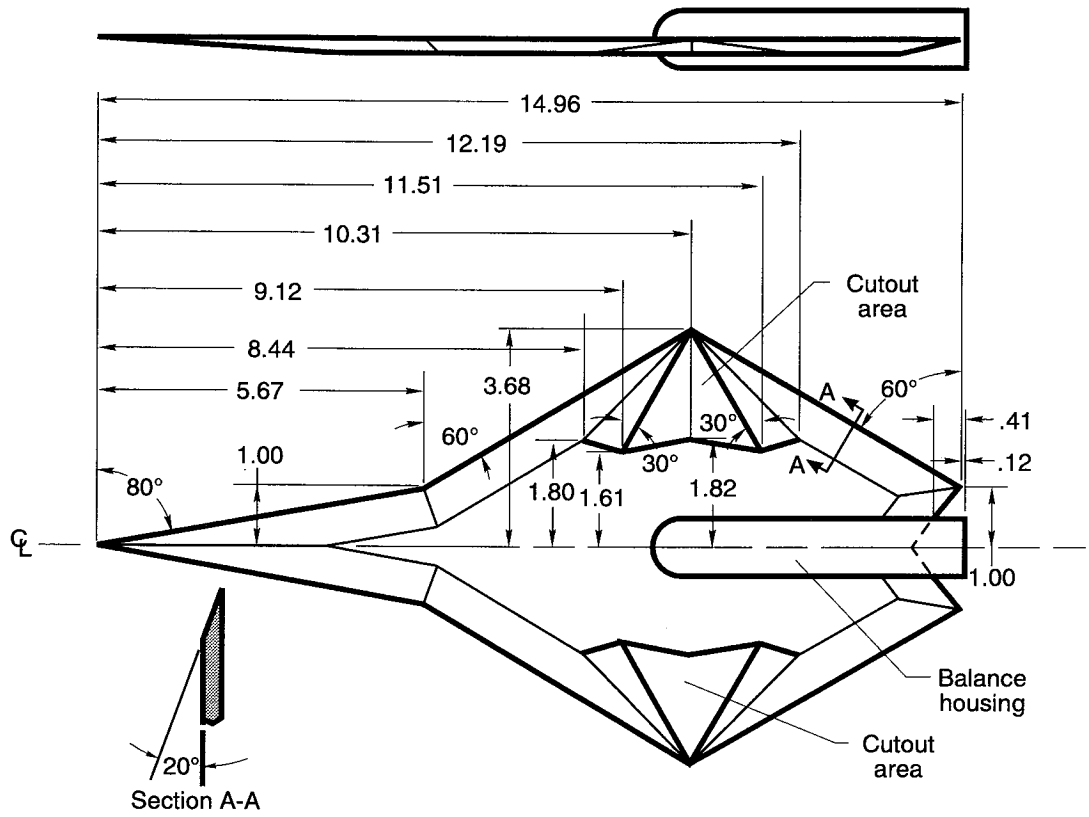

(k) 60° double arrow.

Figure 2. Concluded.

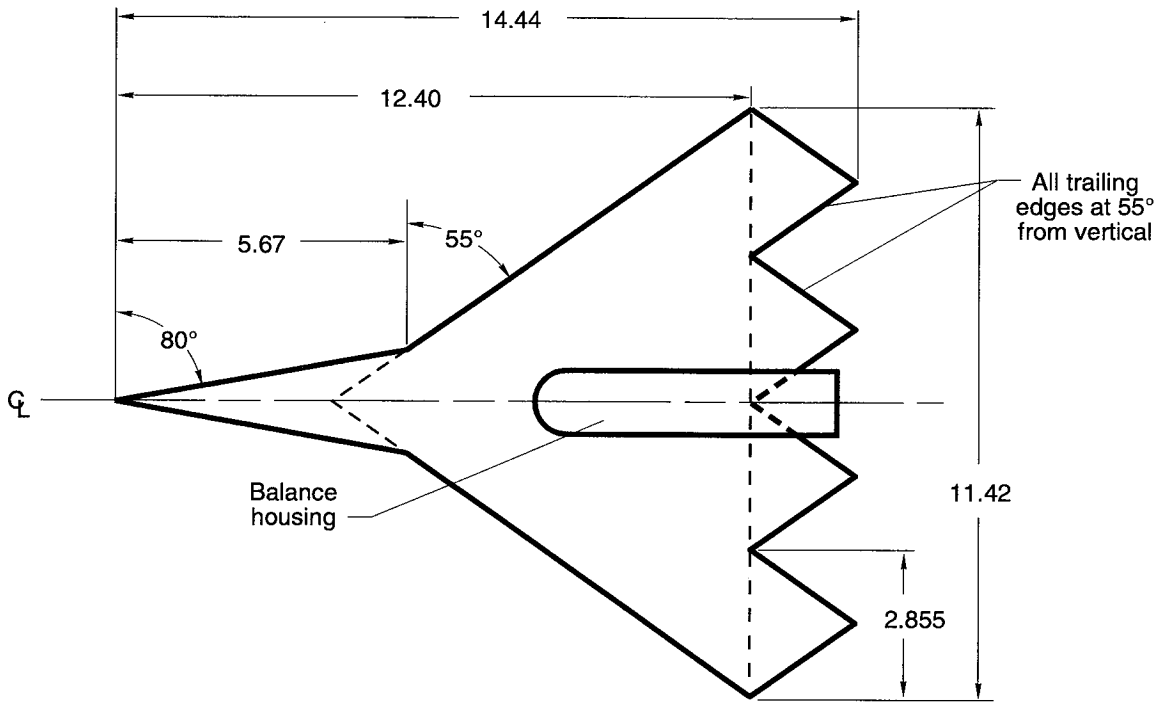

(a) 55° delta with trailing-edge serrations.

Figure 3. Top views of the 10 modified planform models. All linear dimensions are in inches.

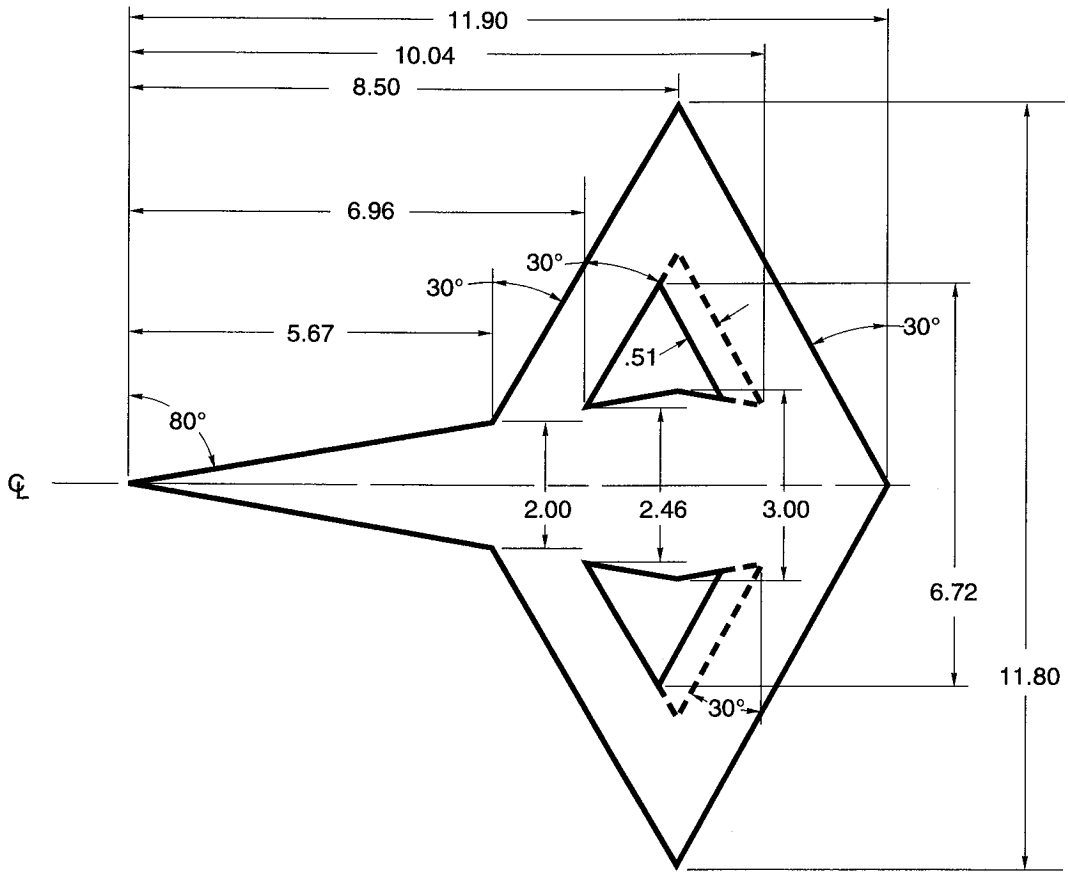

(b) 30° diamond with forward cutout.

Figure 3. Continued.

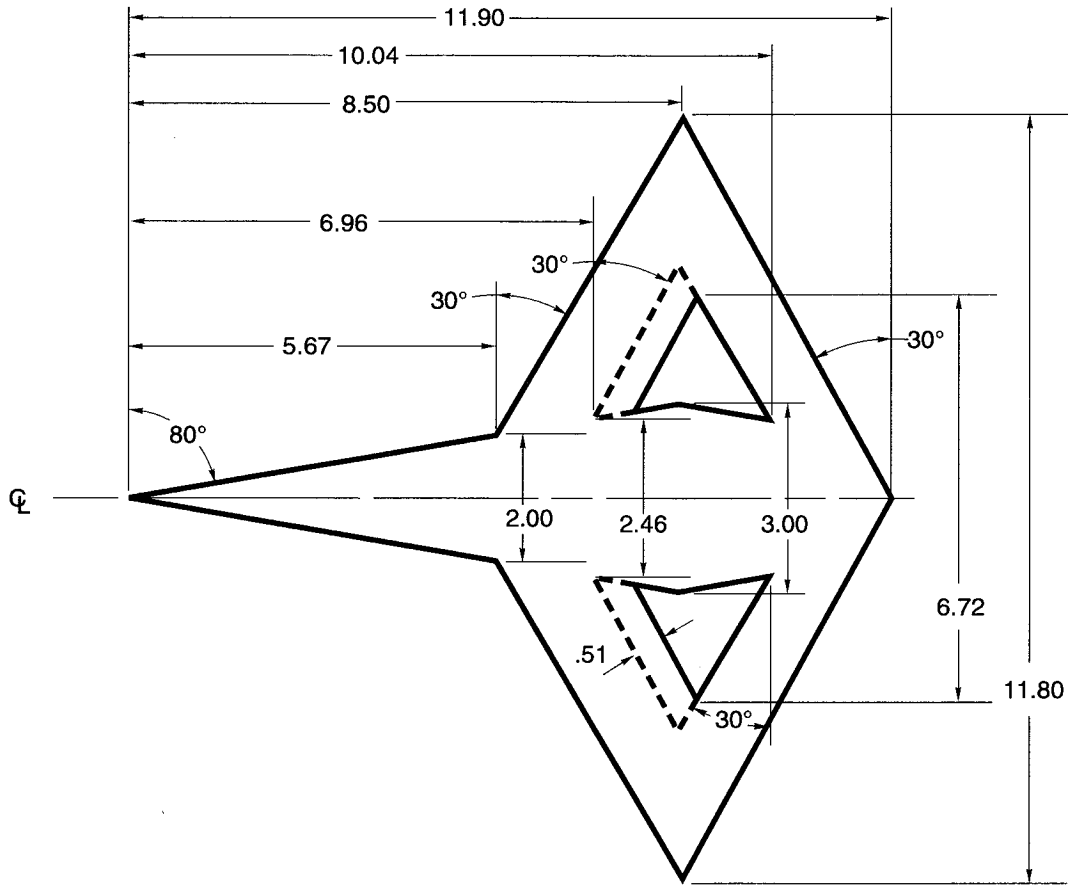

(c) 30° diamond with aft cutout.

Figure 3. Continued.

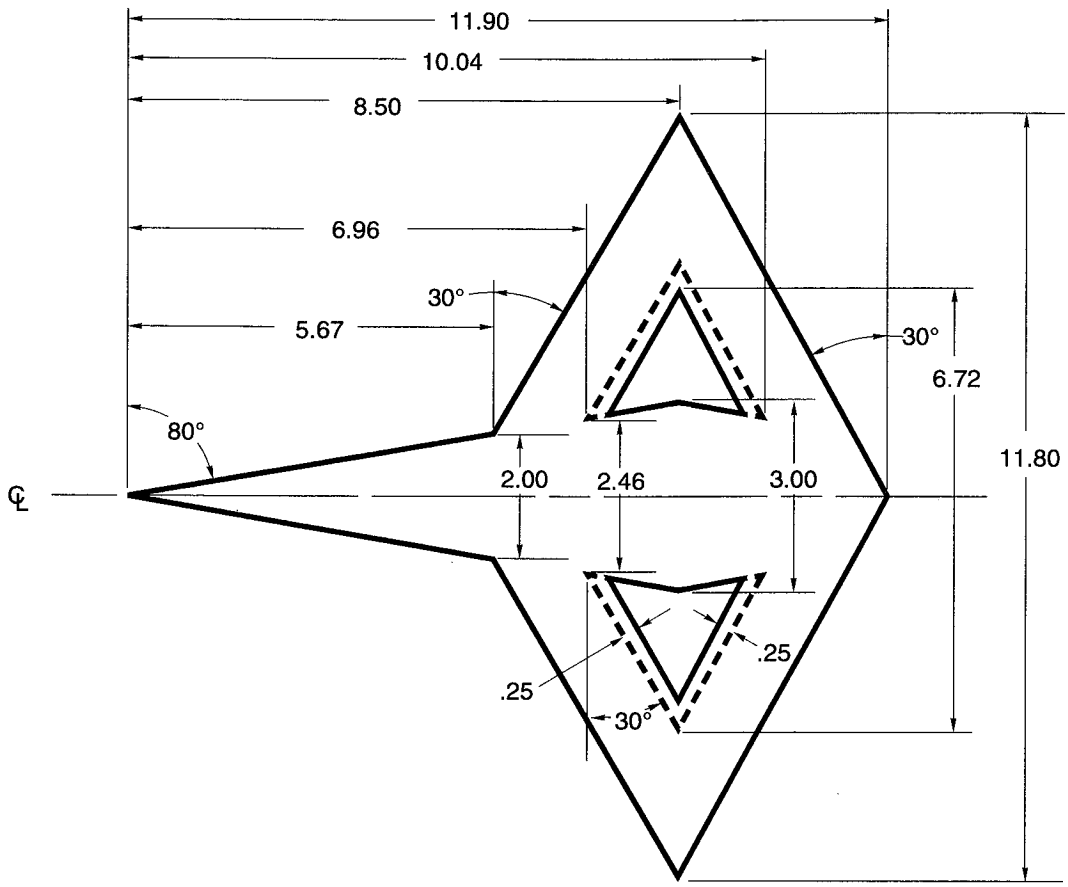

(d) 30° diamond with reduced cutout.

Figure 3. Continued.

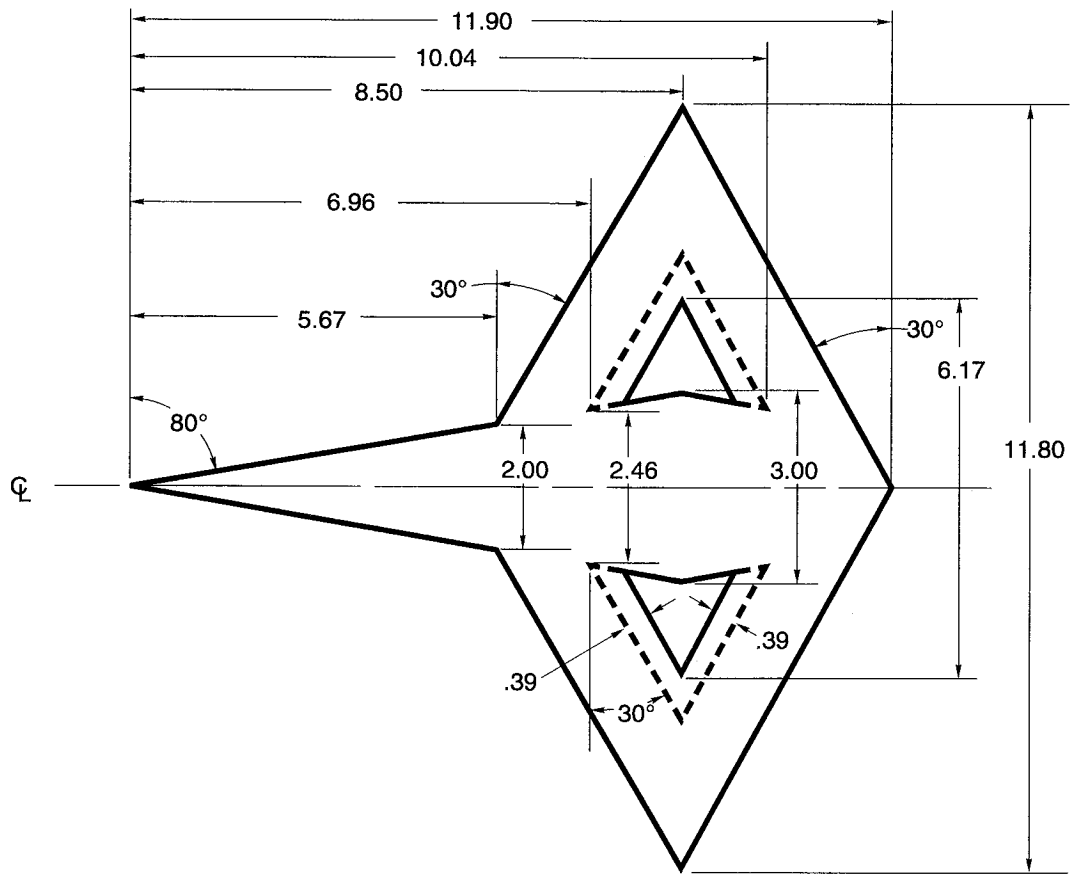

(e) 30° diamond with smallest cutout.

Figure 3. Continued.

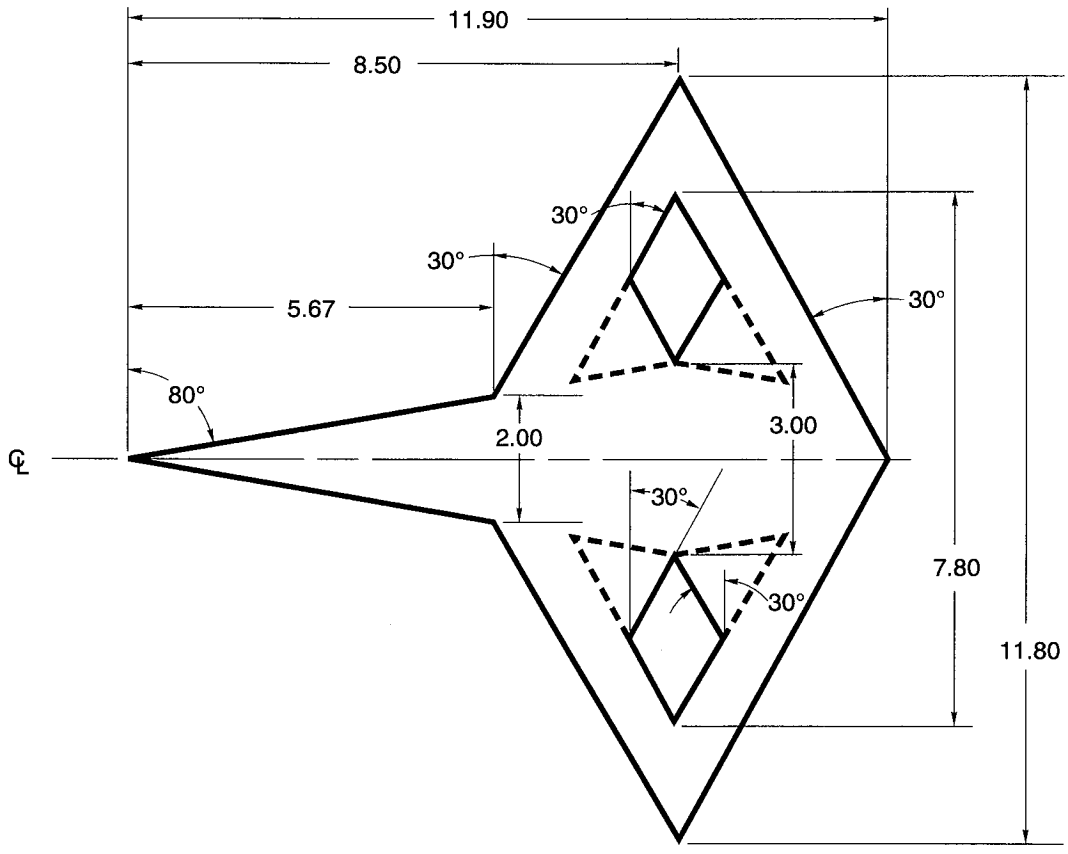

(f) 30° diamond with diamond cutout.

Figure 3. Continued.

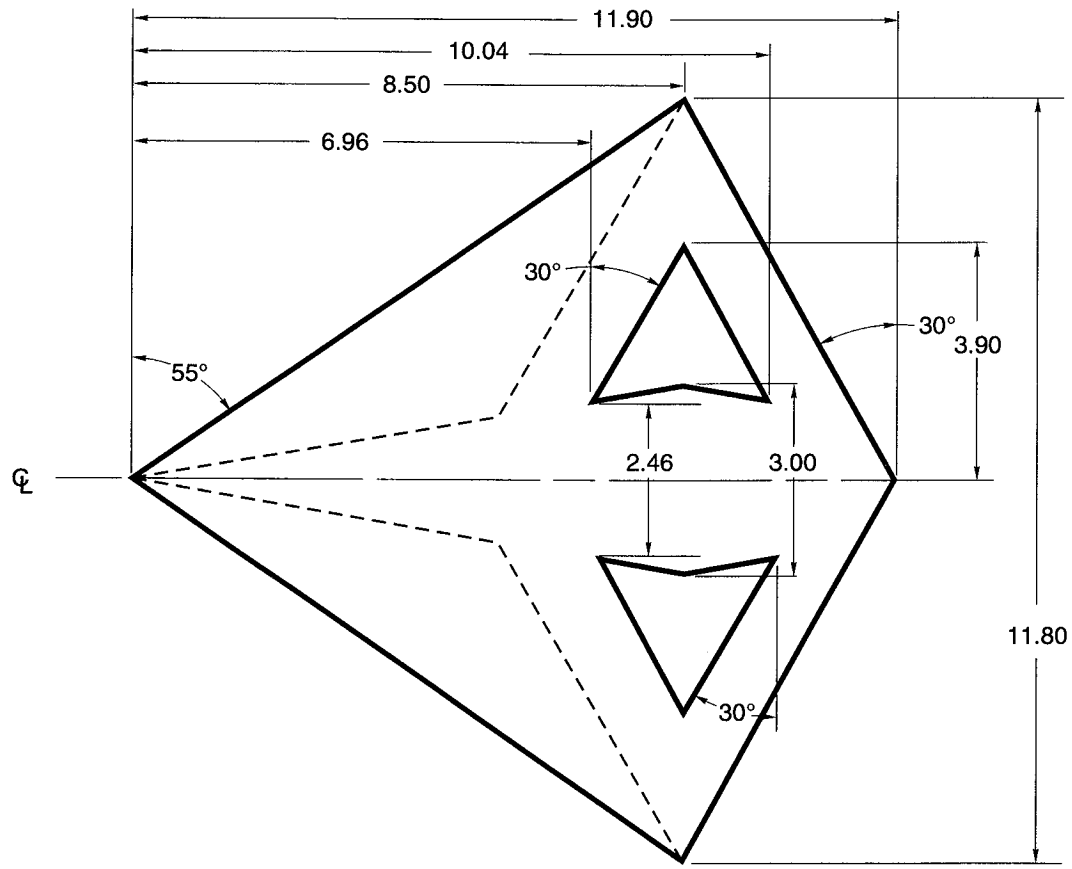

(g) 55° delta cutout wing.

Figure 3. Continued.

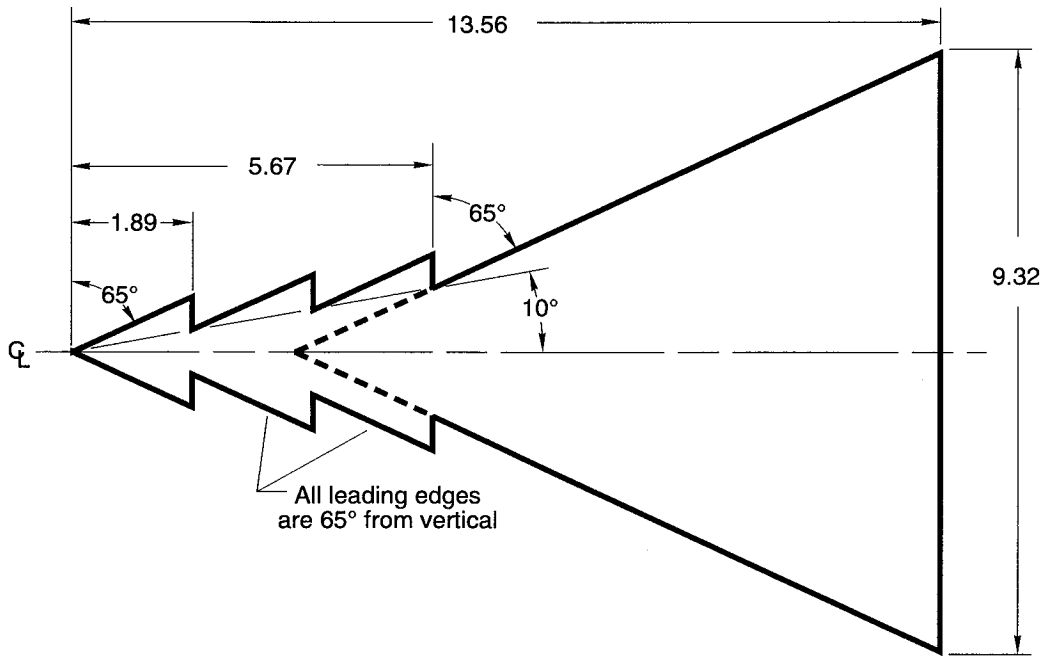

(h) 65° delta with delta sawteeth.

Figure 3. Continued.

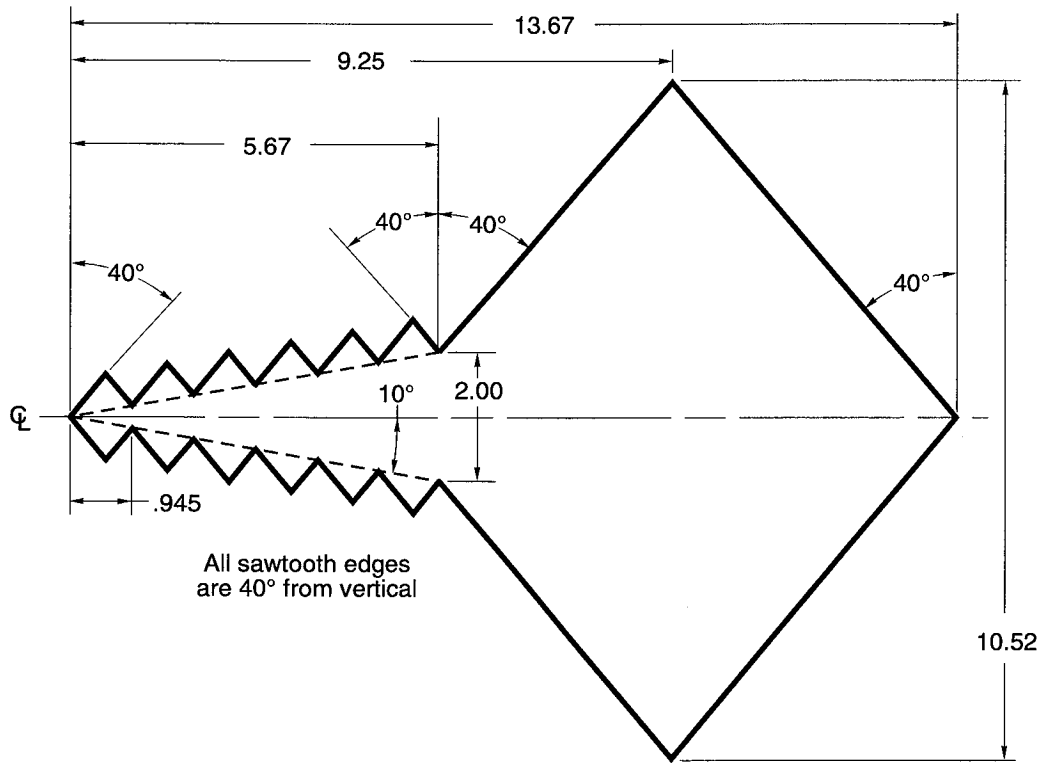

(i) 40° diamond with 6 diamond sawteeth.

Figure 3. Continued.

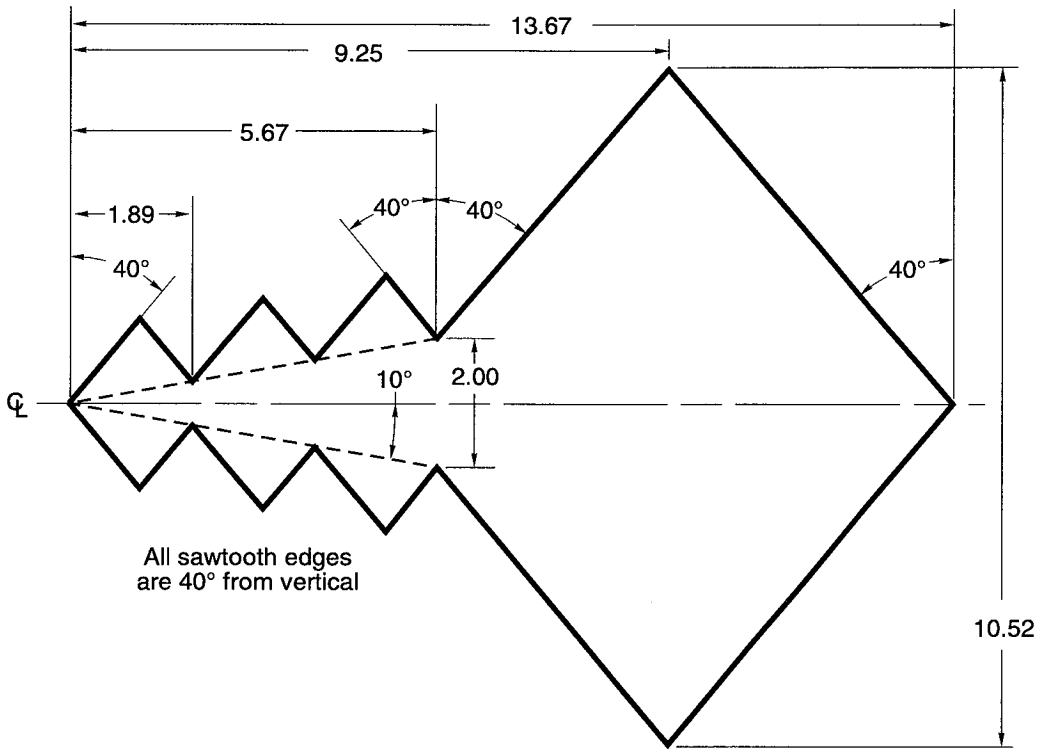

(j) 40° diamond with 3 diamond sawteeth.

Figure 3. Concluded.

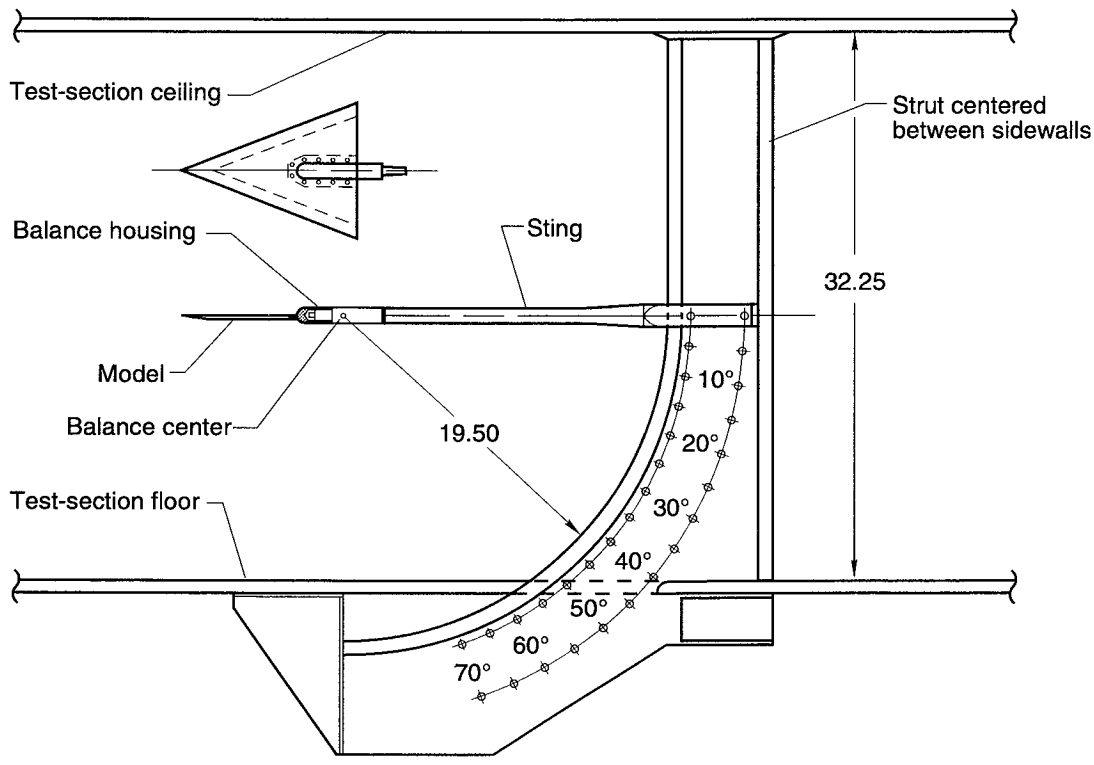

Figure 4. Model support system used in Subsonic Basic Research Tunnel. All linear dimensions are in inches.

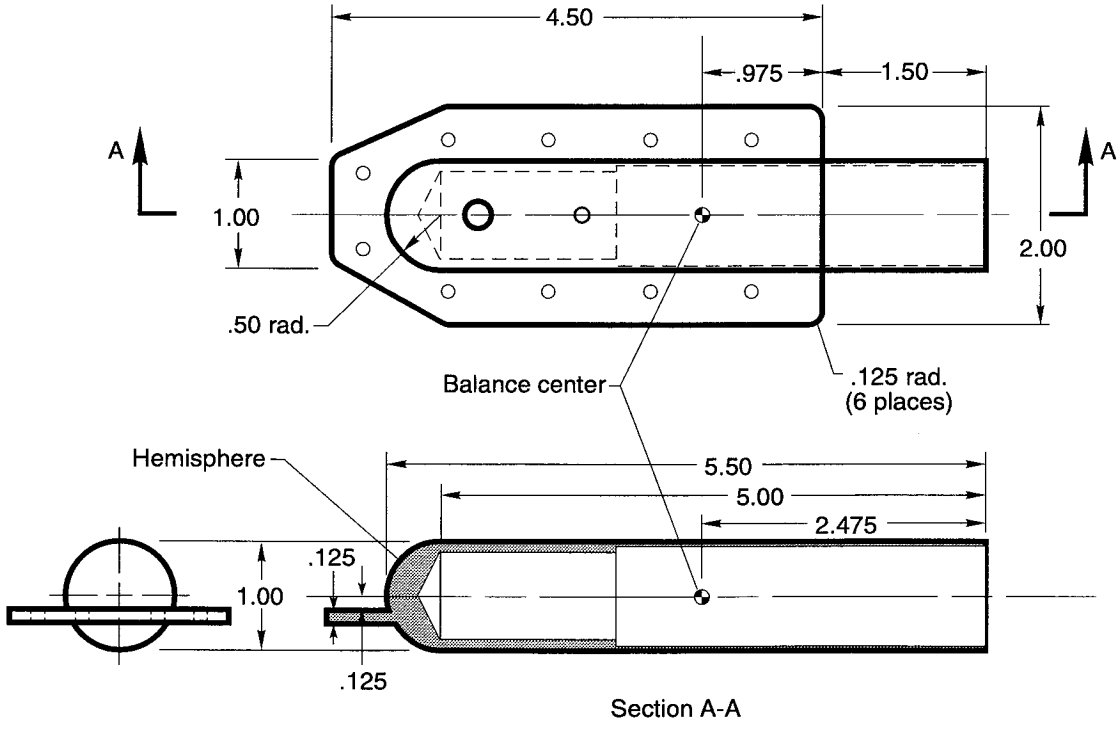

Figure 5. Balance housing used with all models. All linear dimensions are in inches.

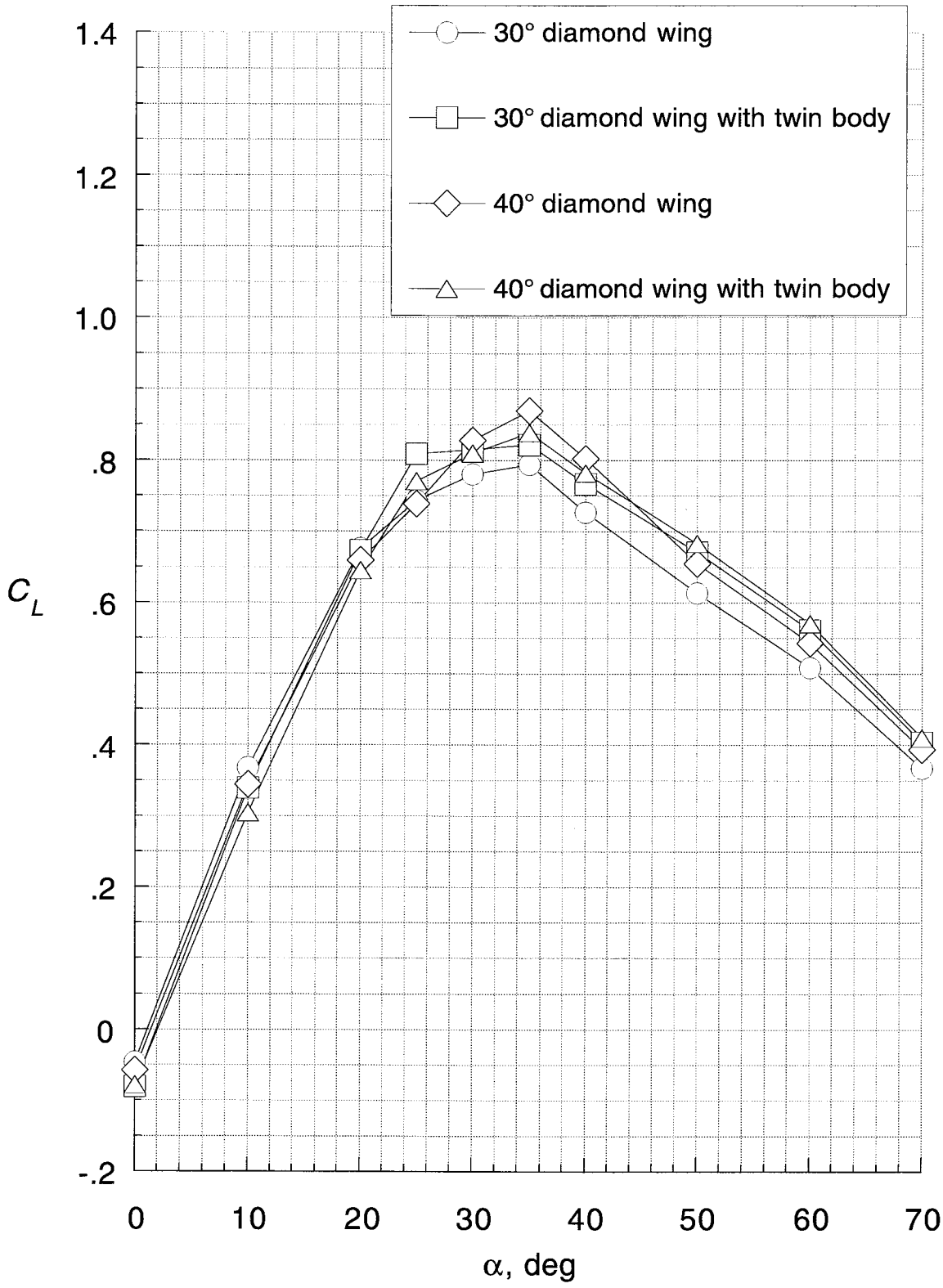

(a) Lift coefficient versus angle of attack.

Figure 6. Longitudinal data illustrating twin-body effects.

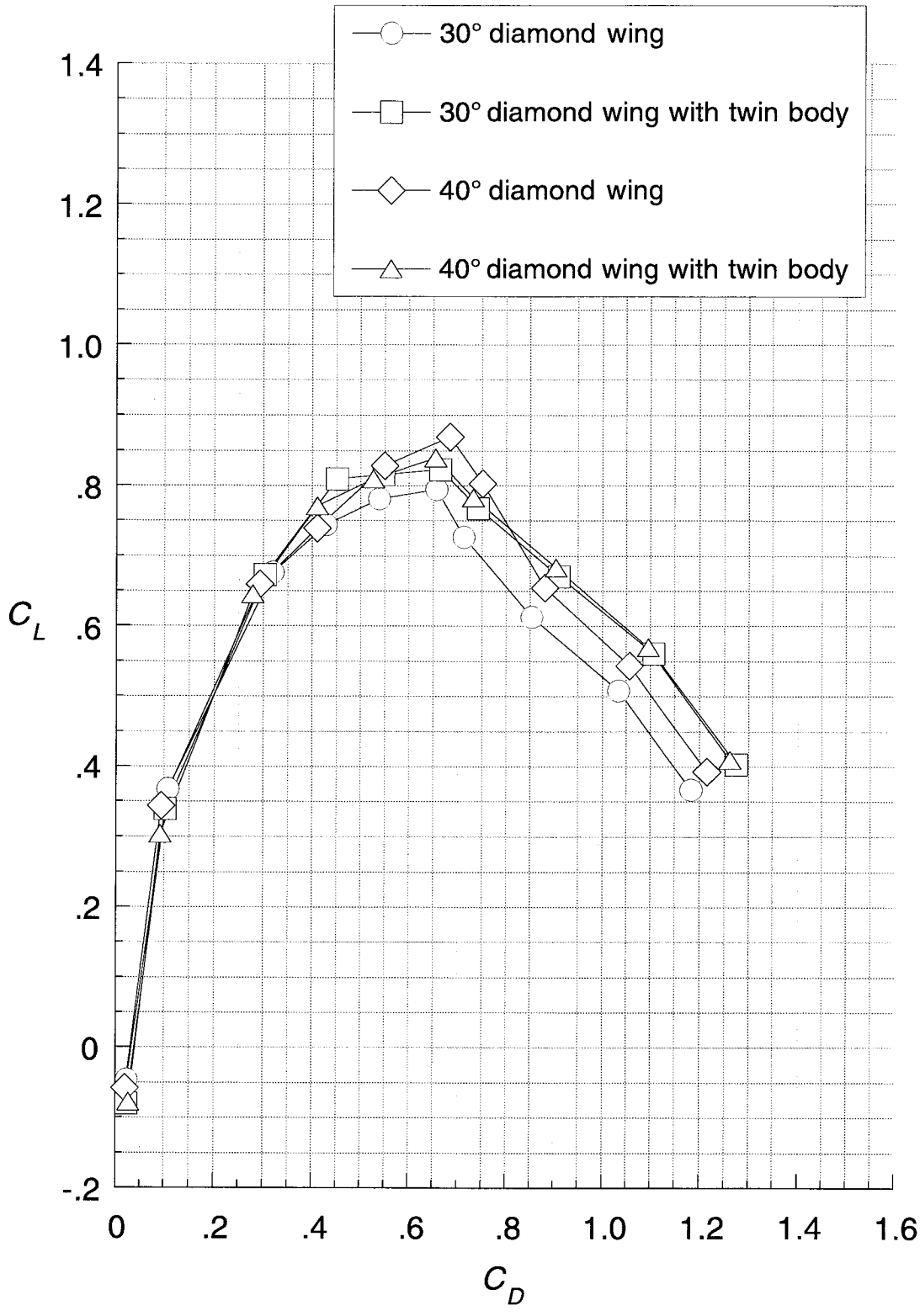

(b) Lift coefficient versus drag coefficient.

Figure 6. Continued.

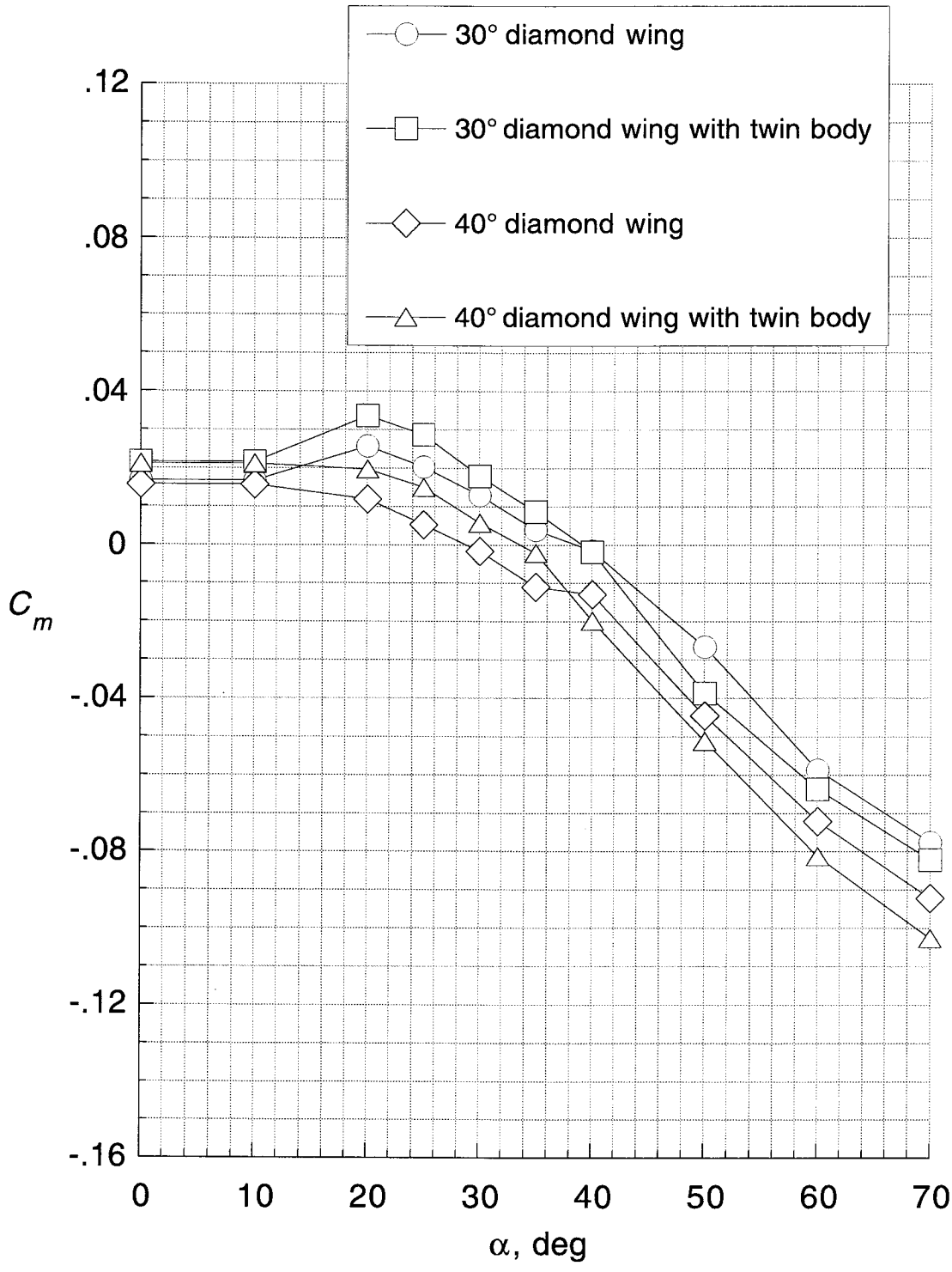

(c) Pitching-moment coefficient versus angle of attack.

Figure 6. Concluded.

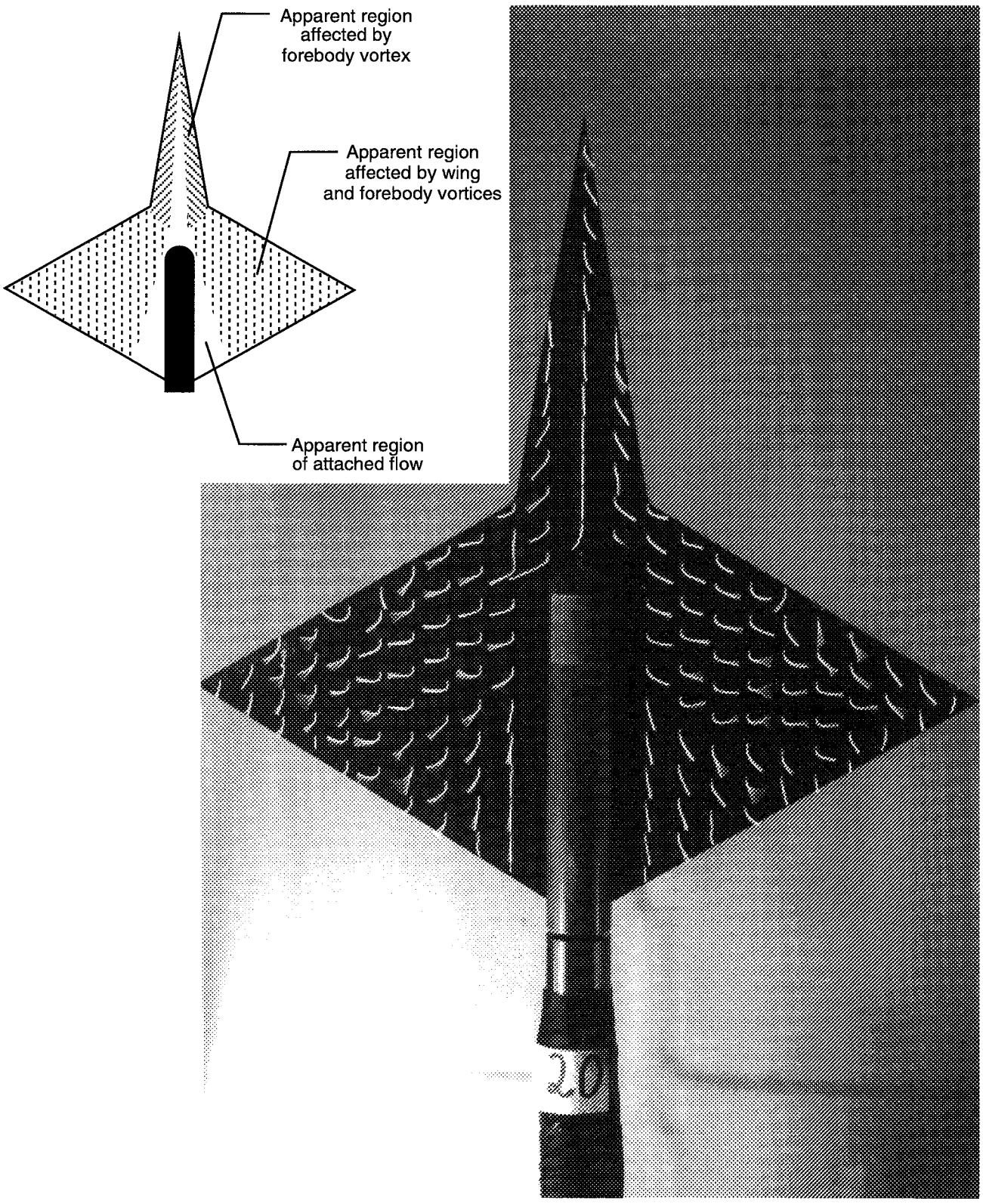

(a) $\alpha = 20°$.

Figure 7. Surface flow visualization on 30° diamond wing.

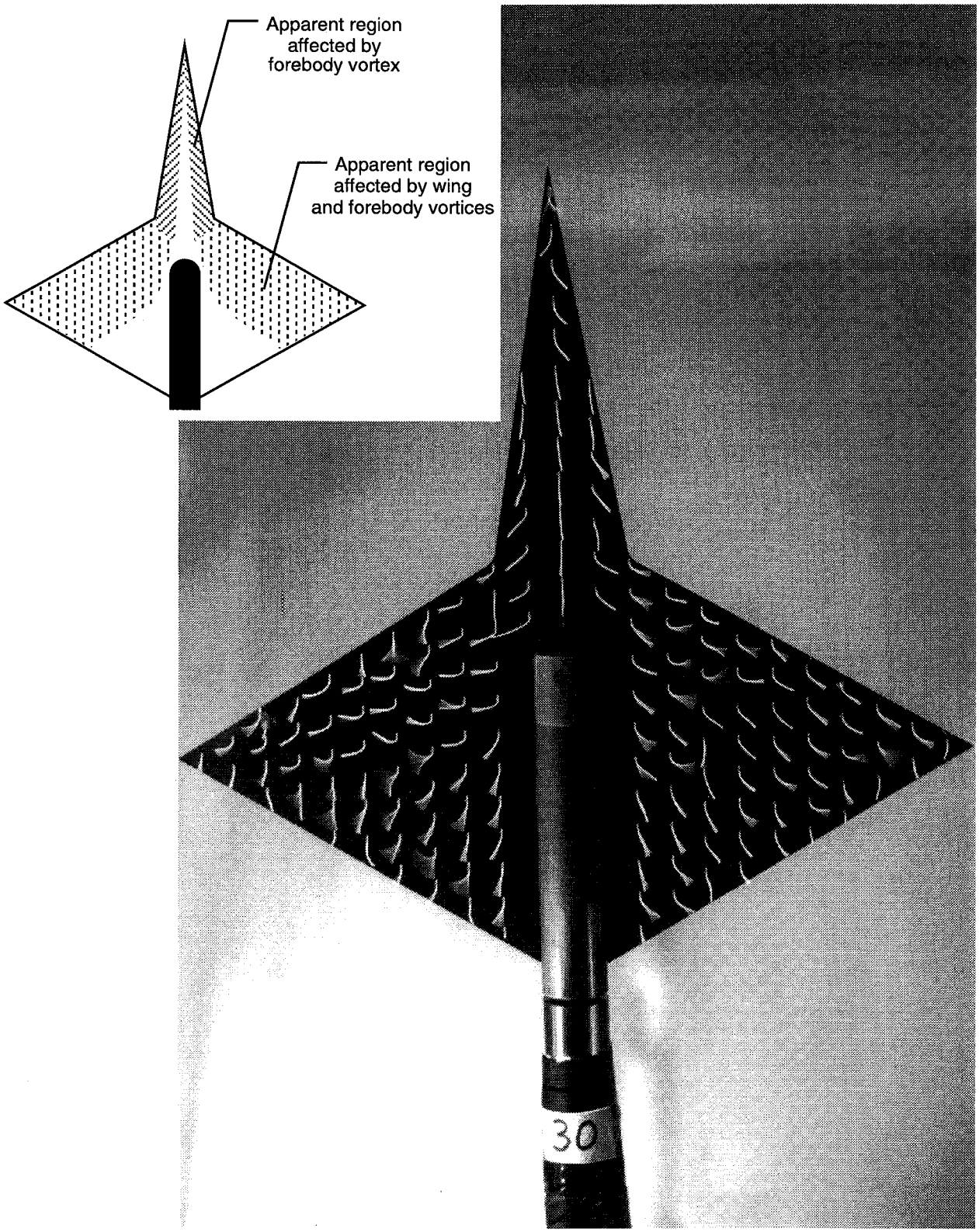

(b) $\alpha = 30°$.

Figure 7. Continued.

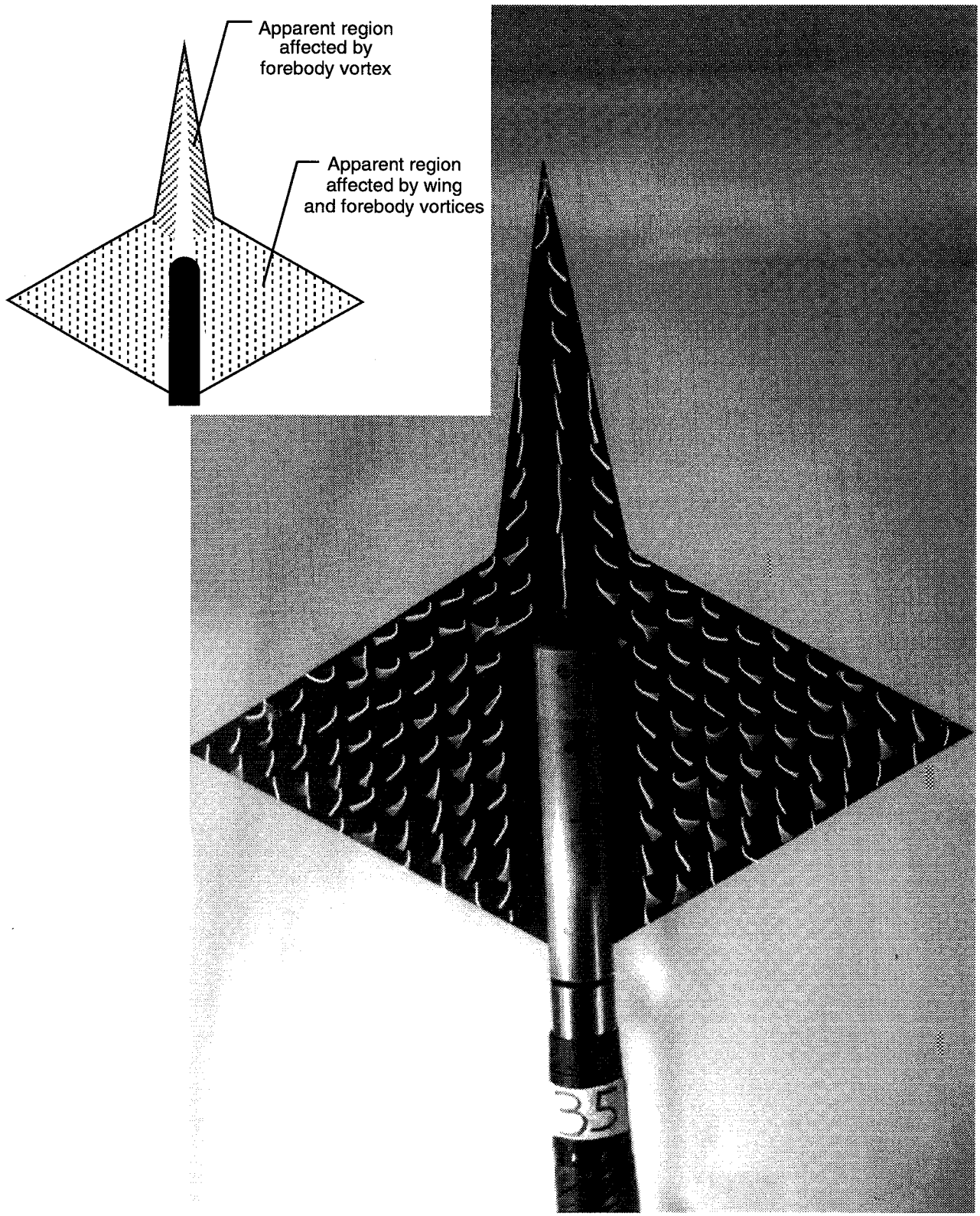

(c) $\alpha = 35°$.

Figure 7. Continued.

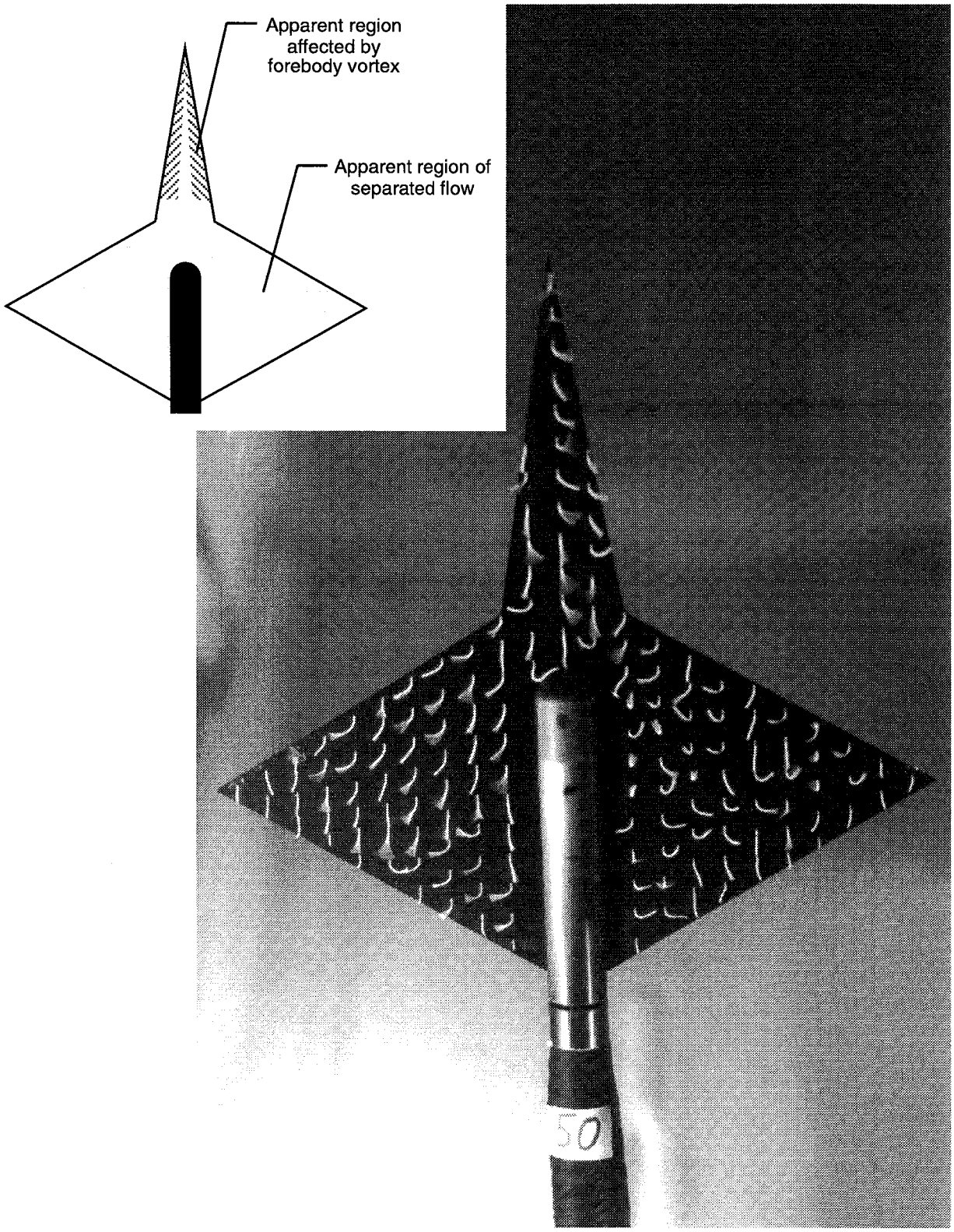

(d) $\alpha = 50°$.

Figure 7. Concluded.

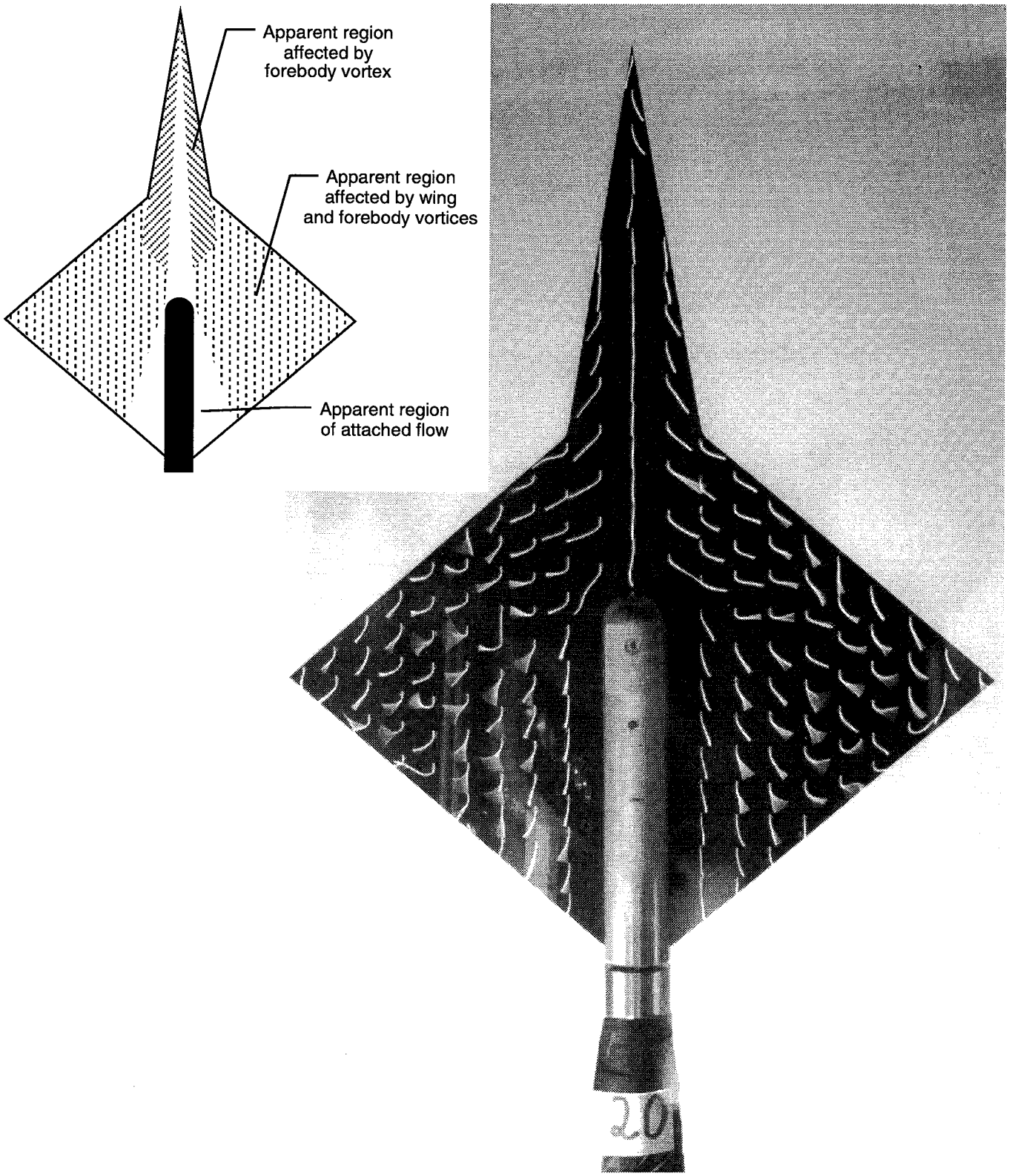

(a) $\alpha = 20°$.

Figure 8. Surface flow visualization on 40° diamond wing.

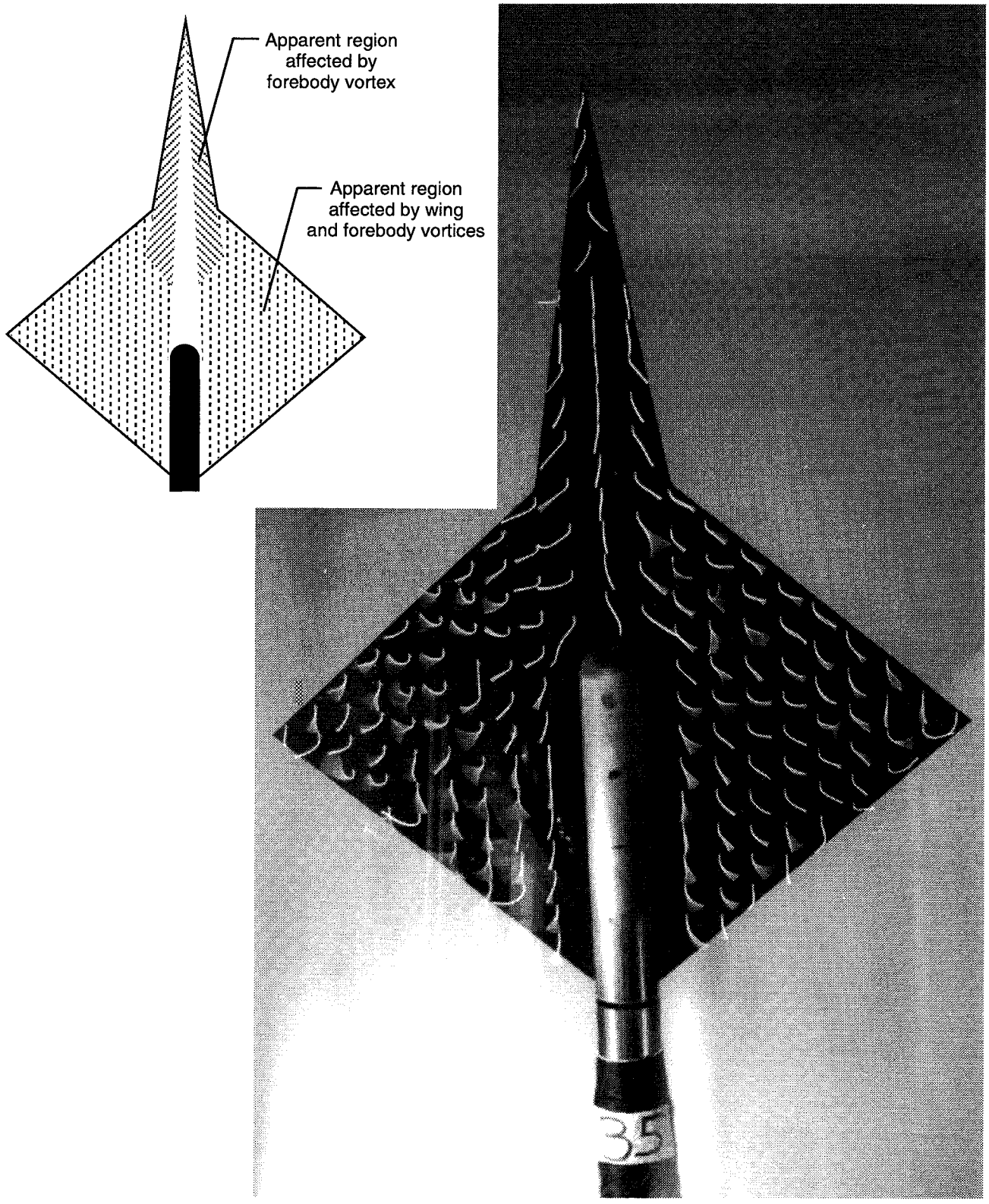

(b) $\alpha = 35°$.

Figure 8. Continued.

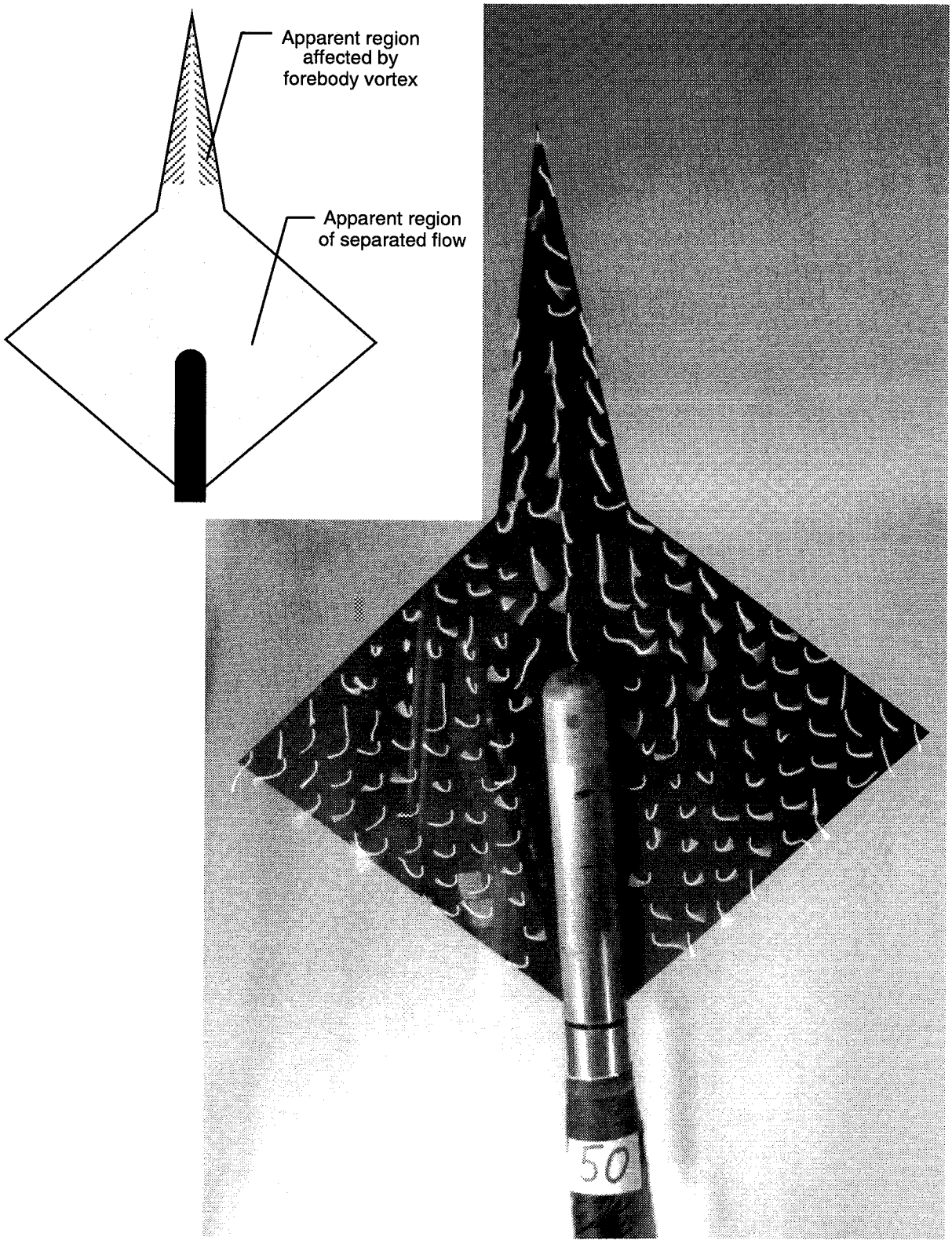

(c) $\alpha = 50°$.

Figure 8. Concluded.

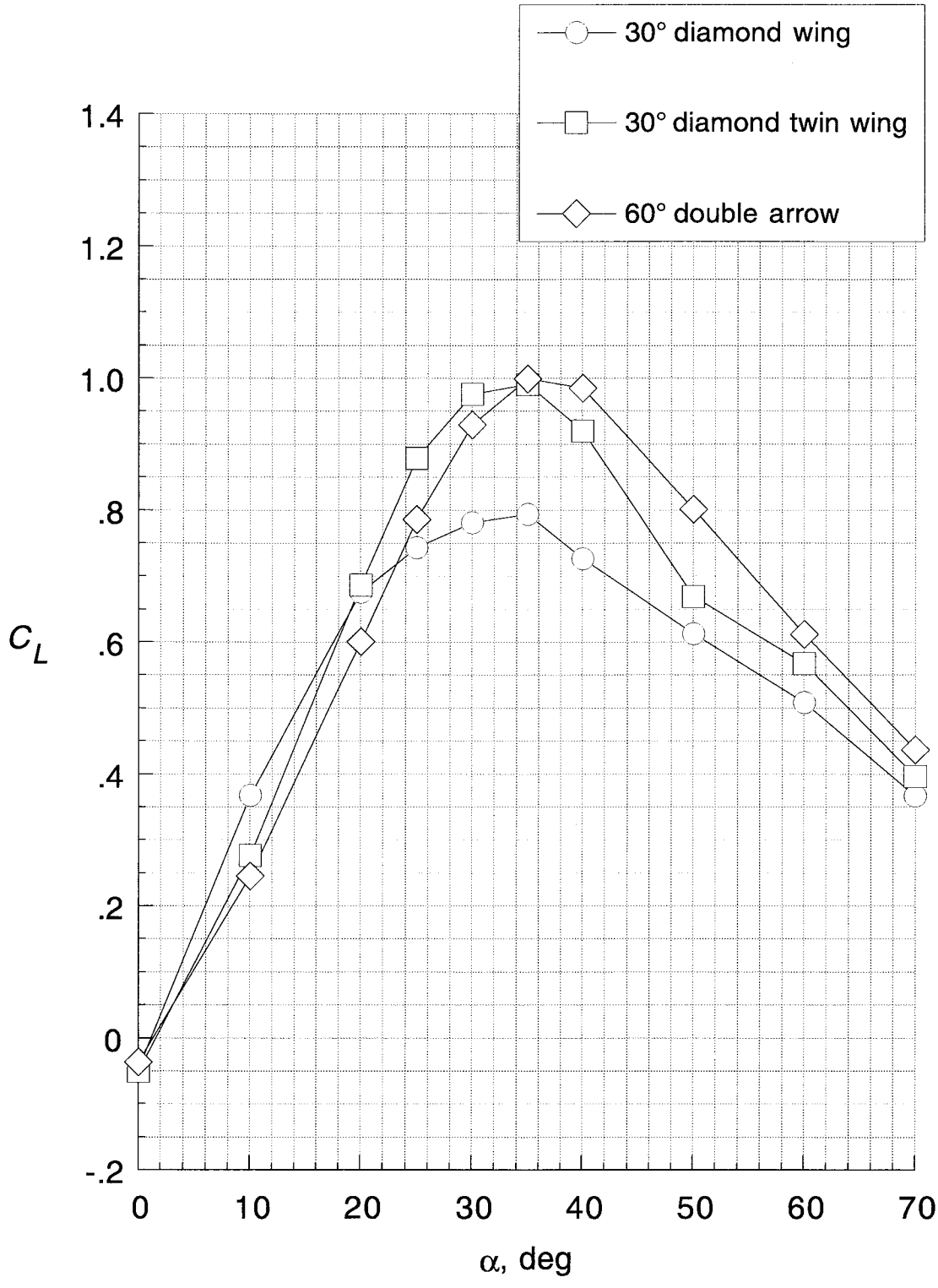

(a) Lift coefficient versus angle of attack.

Figure 9. Longitudinal data illustrating double-wing effects.

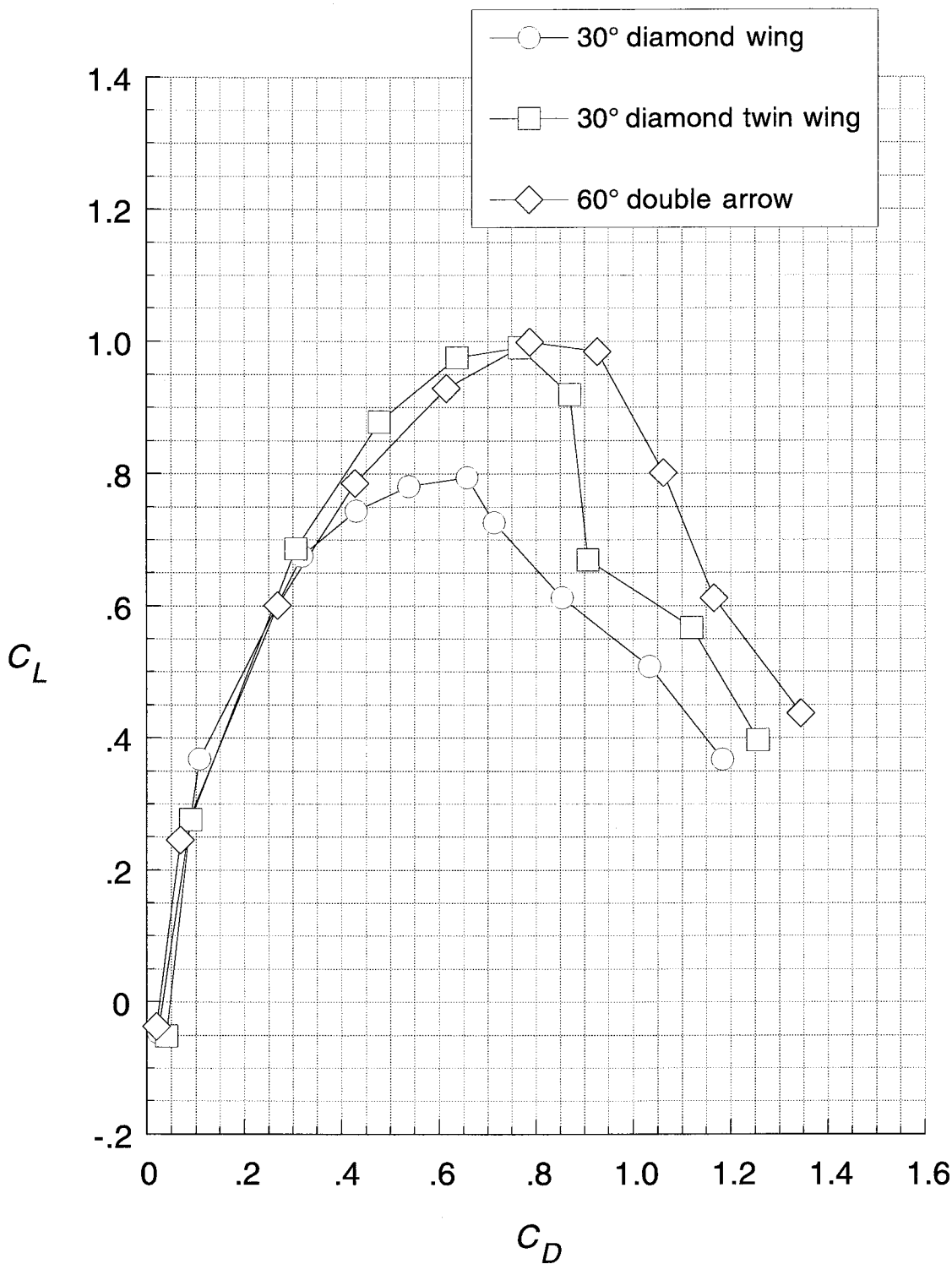

(b) Lift coefficient versus drag coefficient.

Figure 9. Continued.

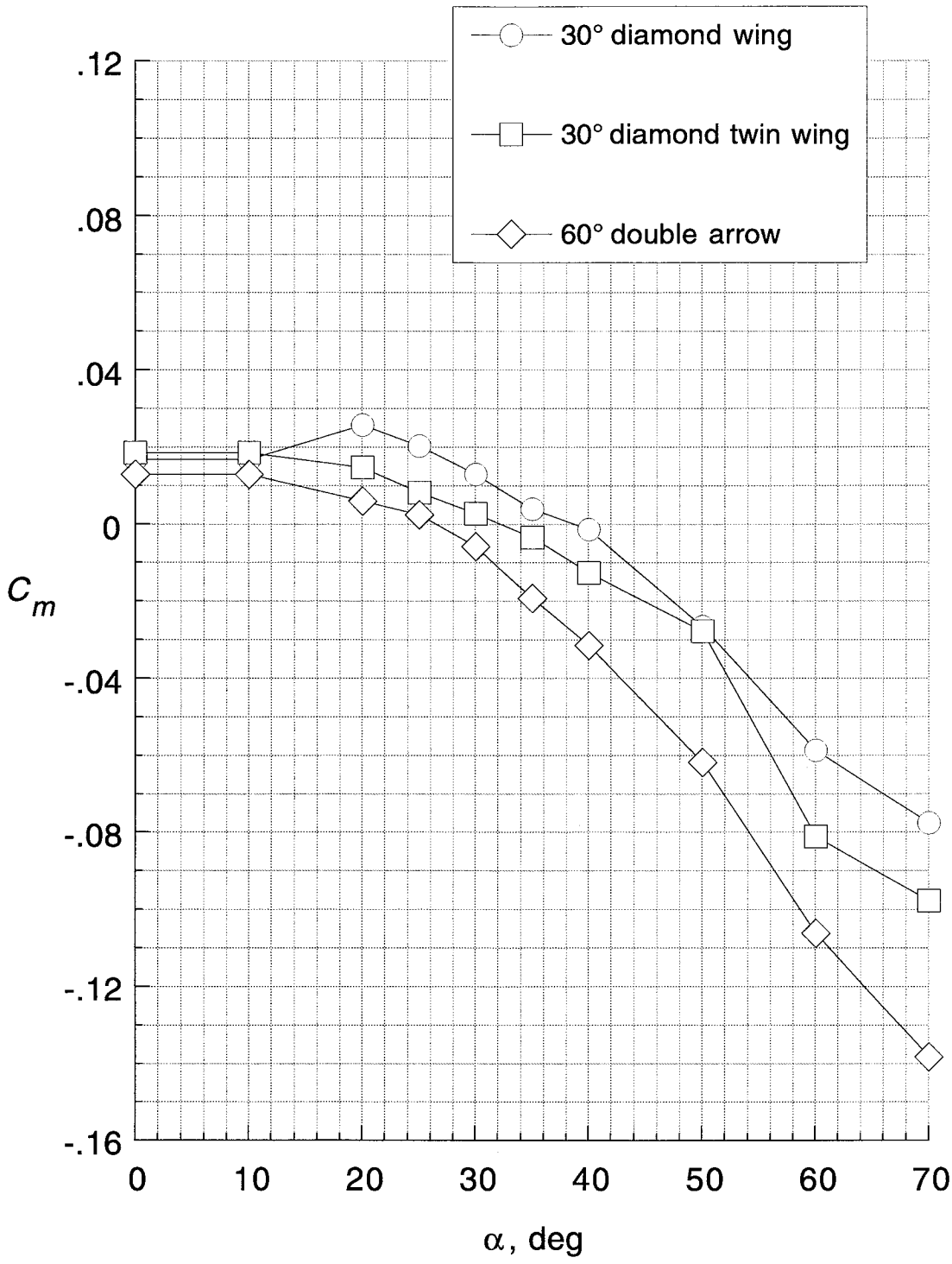

(c) Pitching-moment coefficient versus angle of attack.

Figure 9. Concluded.

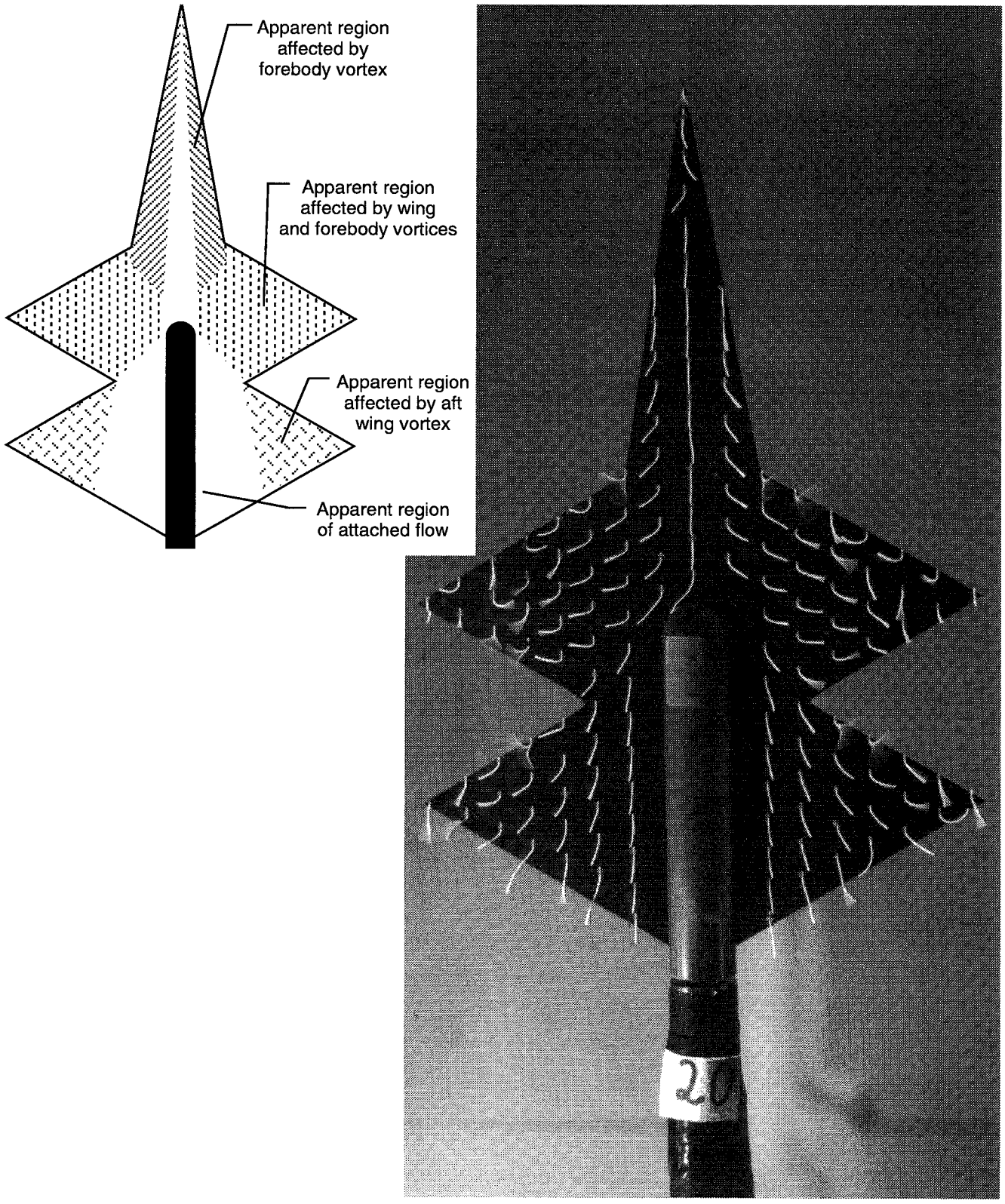

(a) $\alpha = 20°$.

Figure 10. Surface flow visualization on 30° diamond twin wing.

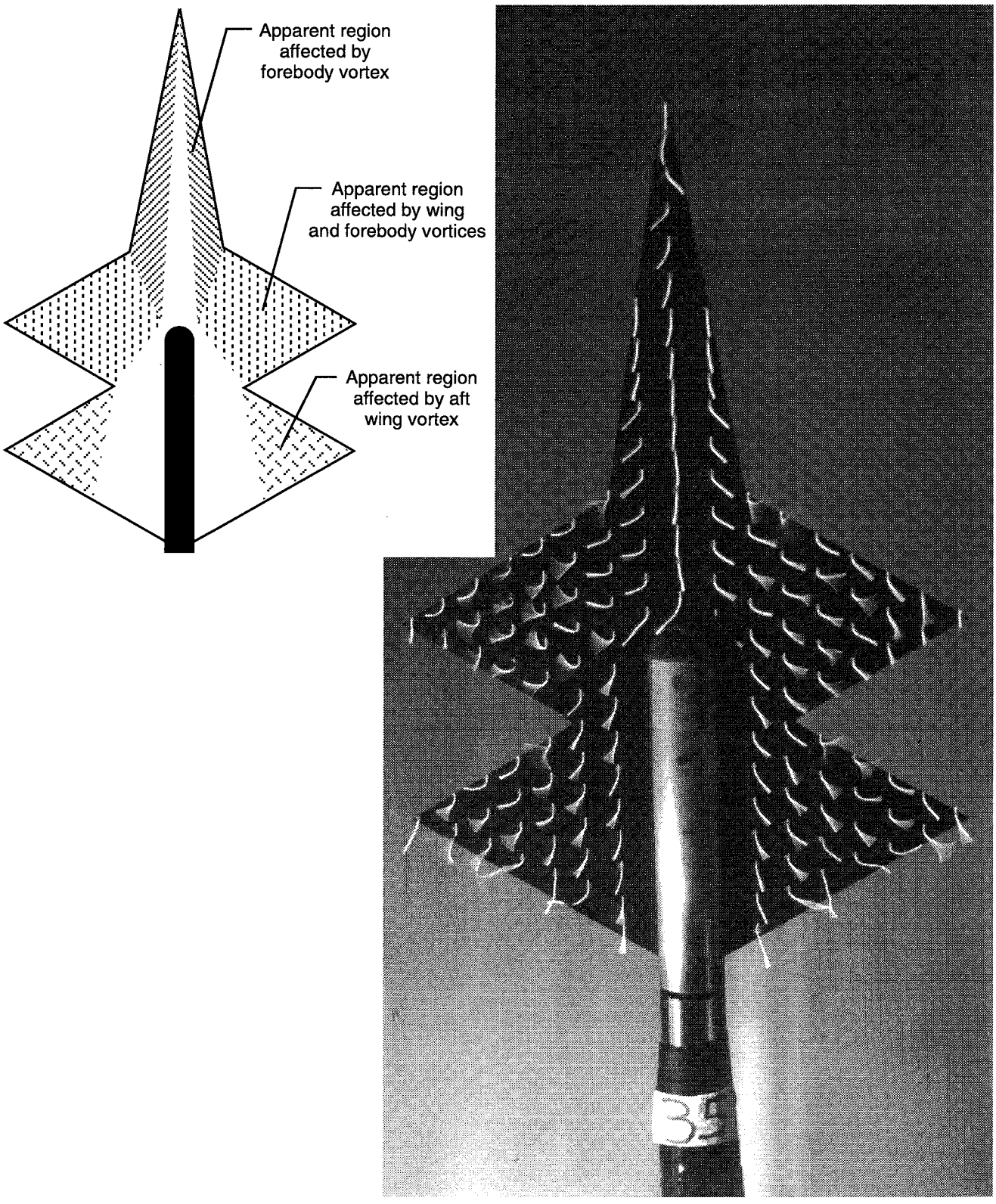

(b) $\alpha = 35°$.

Figure 10. Continued.

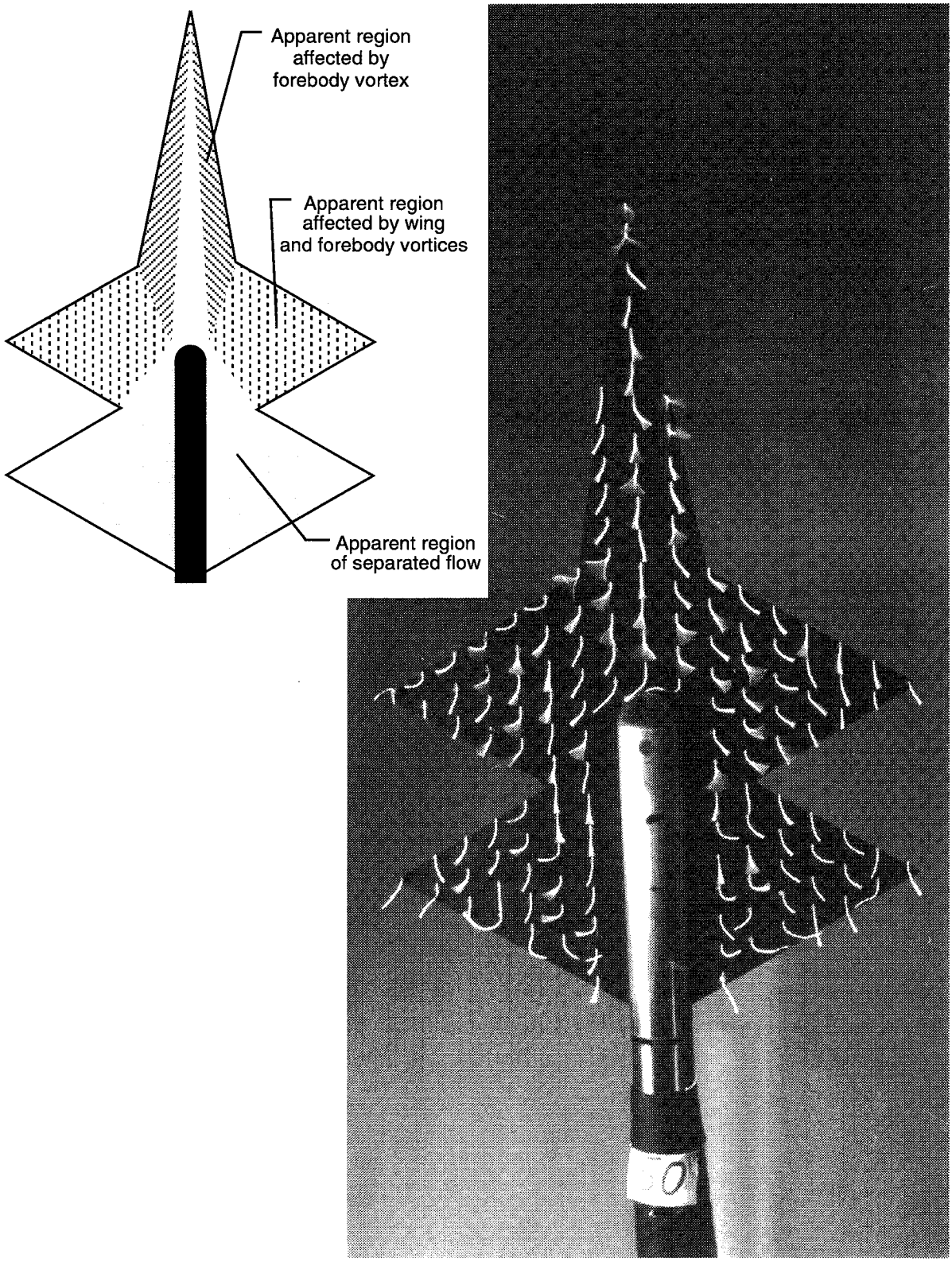

(c) $\alpha = 50°$.

Figure 10. Concluded.

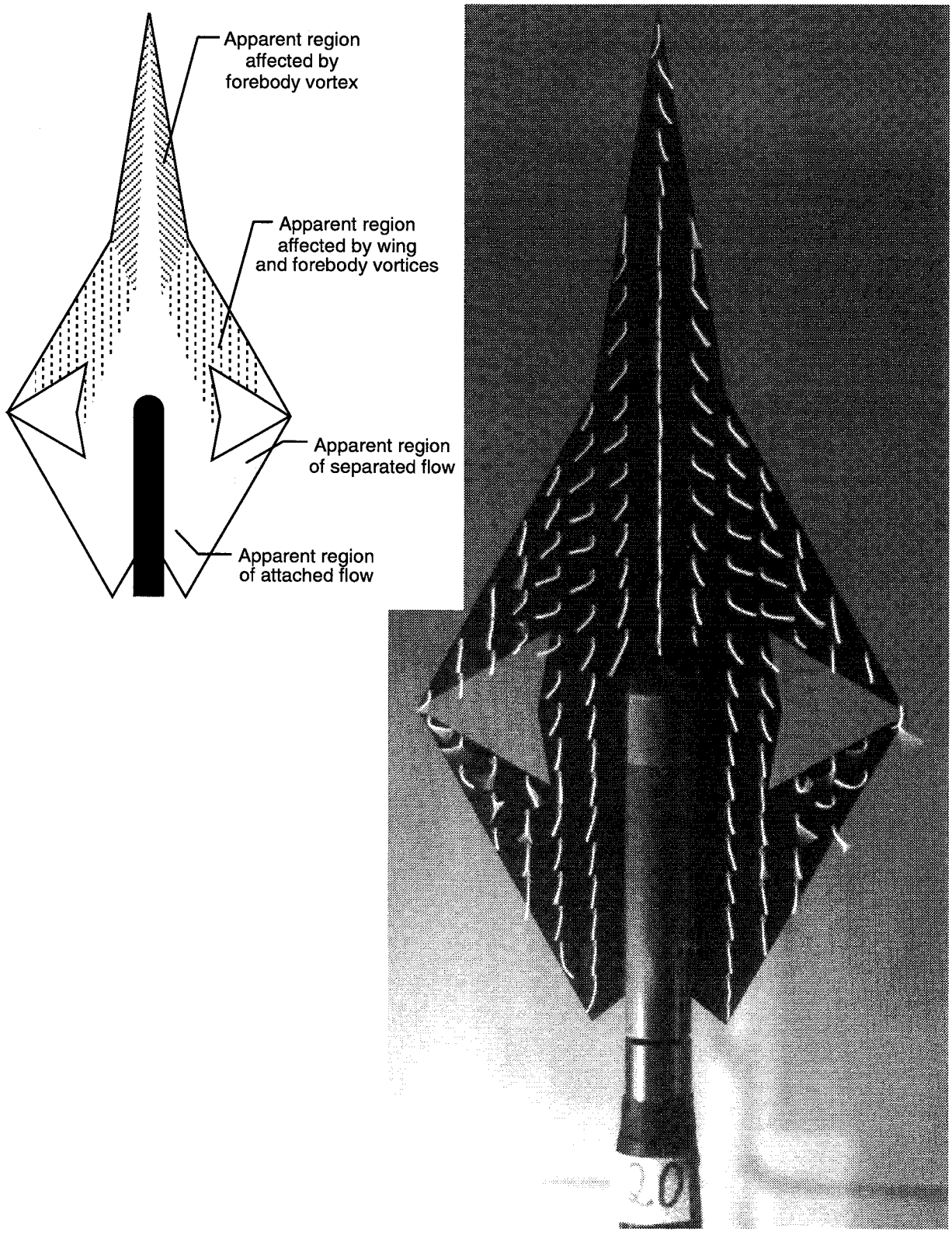

(a) $\alpha = 20°$.

Figure 11. Surface flow visualization on 60° double arrow.

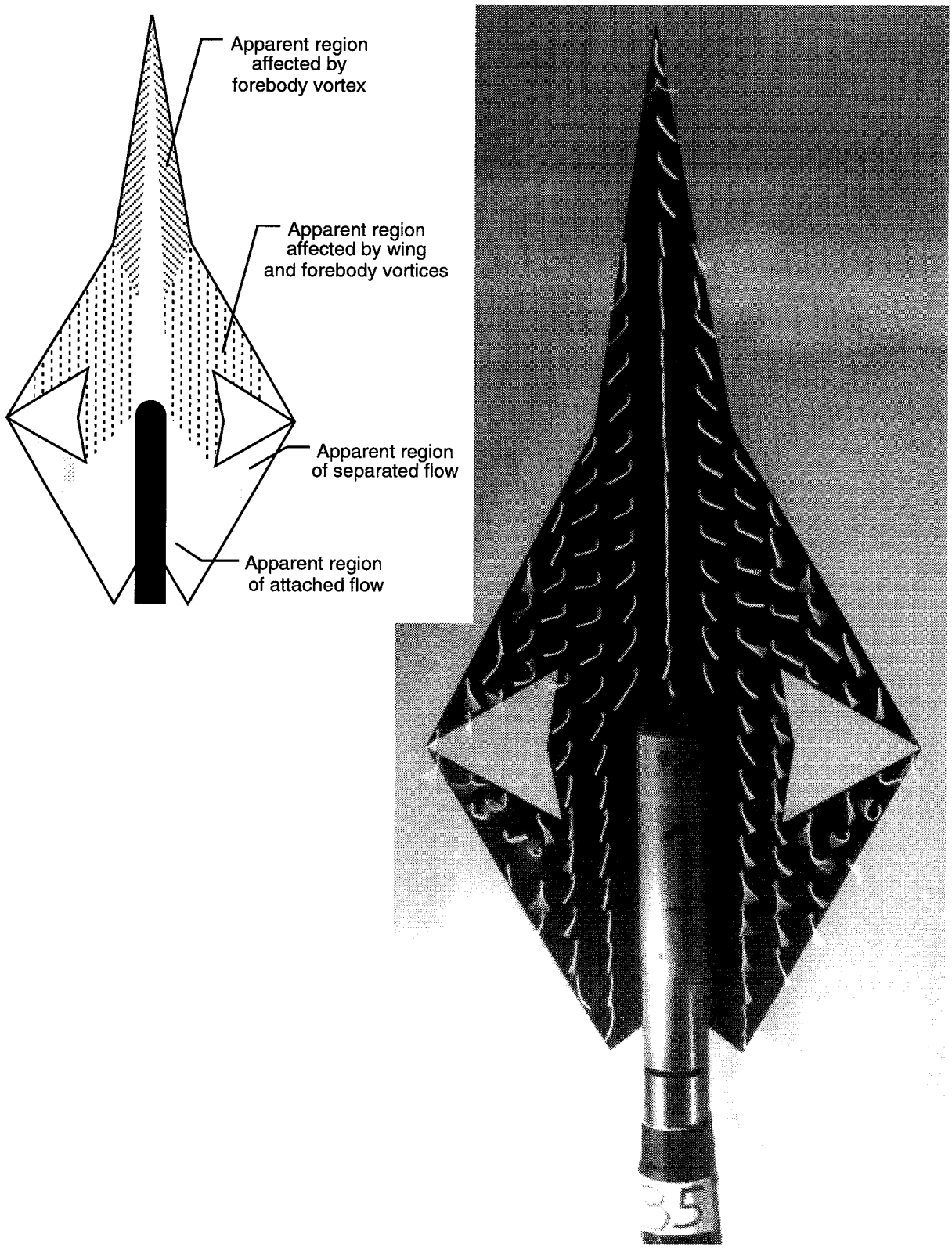

(b) $\alpha = 35°$.

Figure 11. Continued.

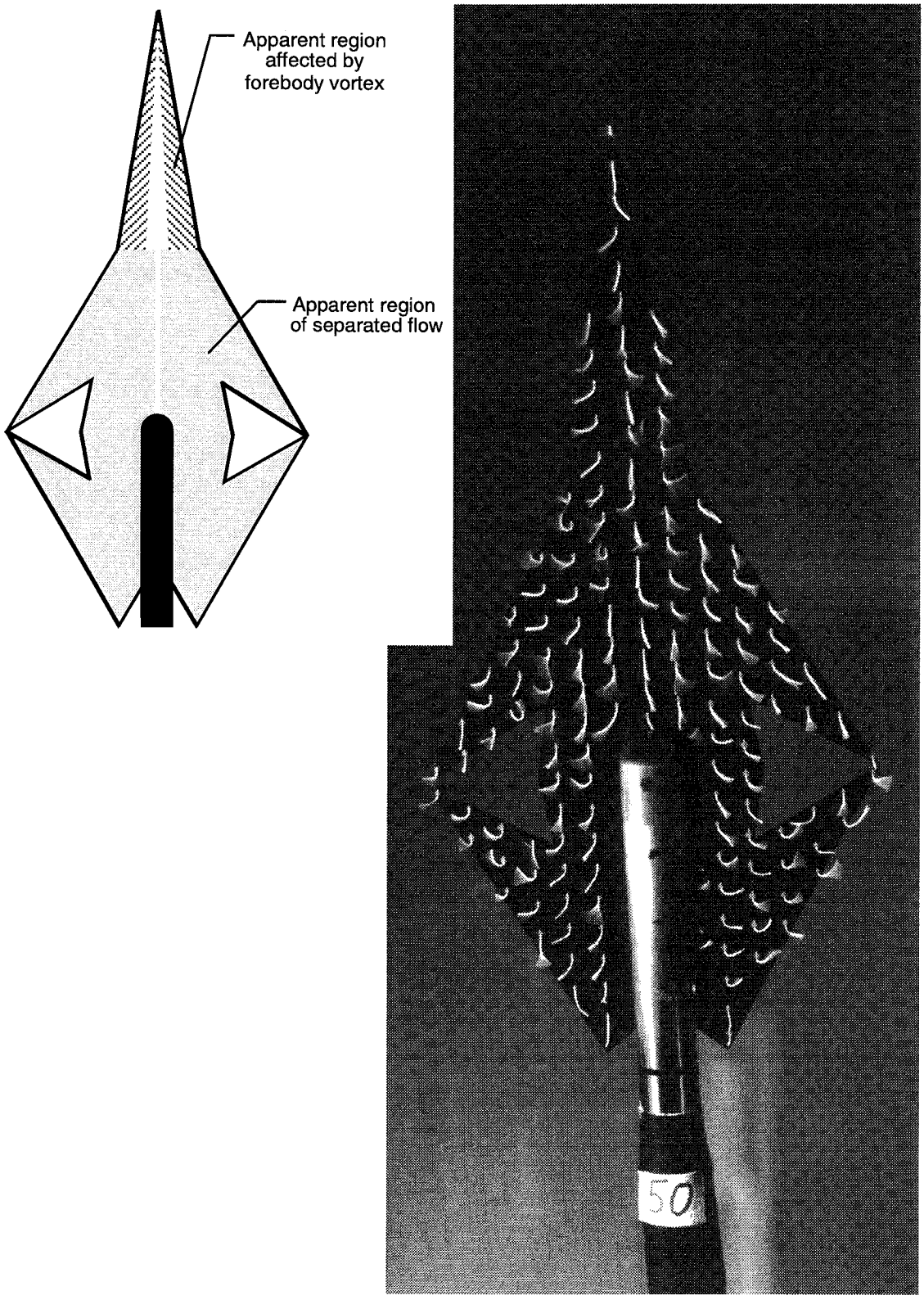

(c) $\alpha = 50°$.

Figure 11. Concluded.

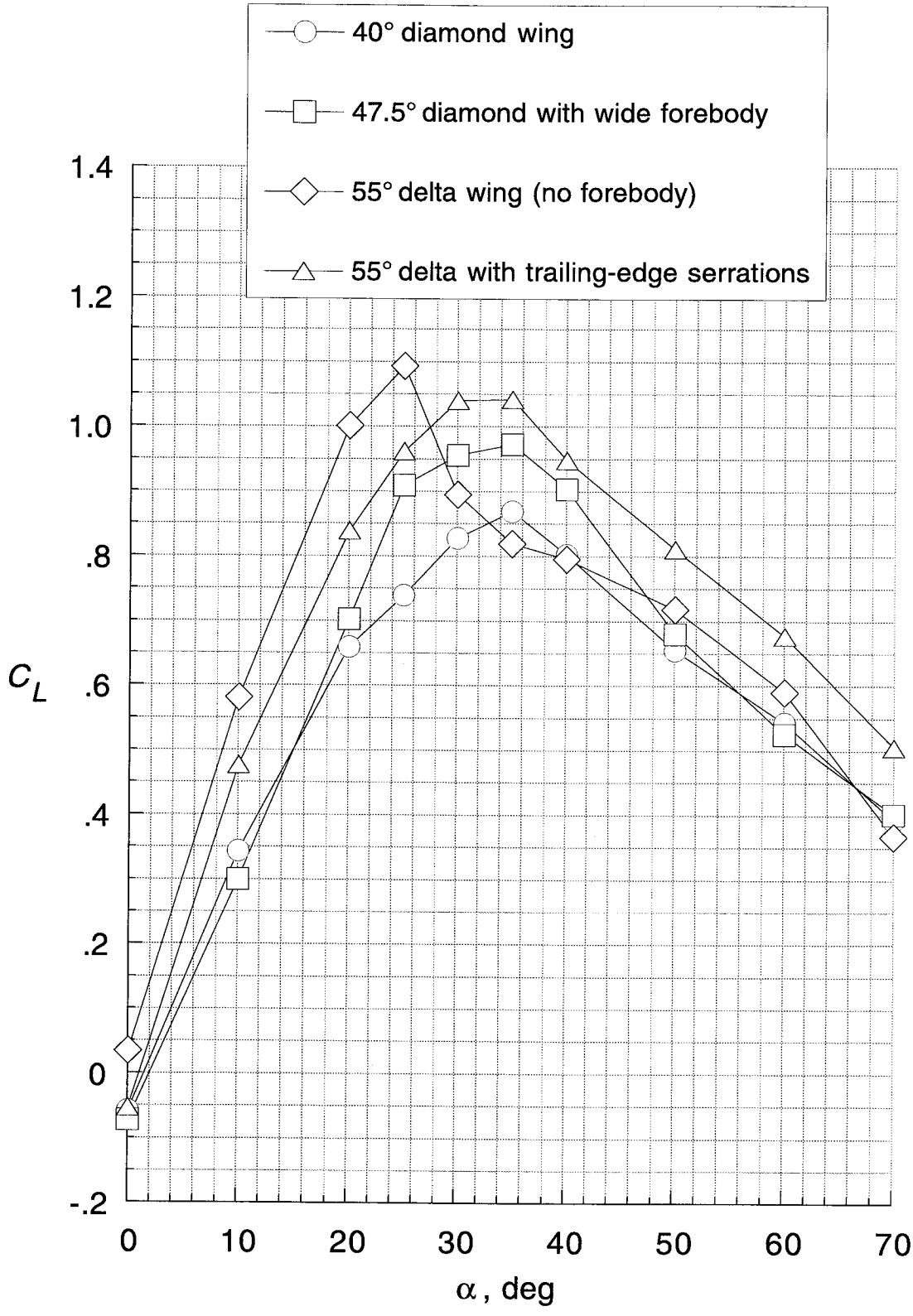

(a) Lift coefficient versus angle of attack.

Figure 12. Longitudinal data illustrating forebody effects.

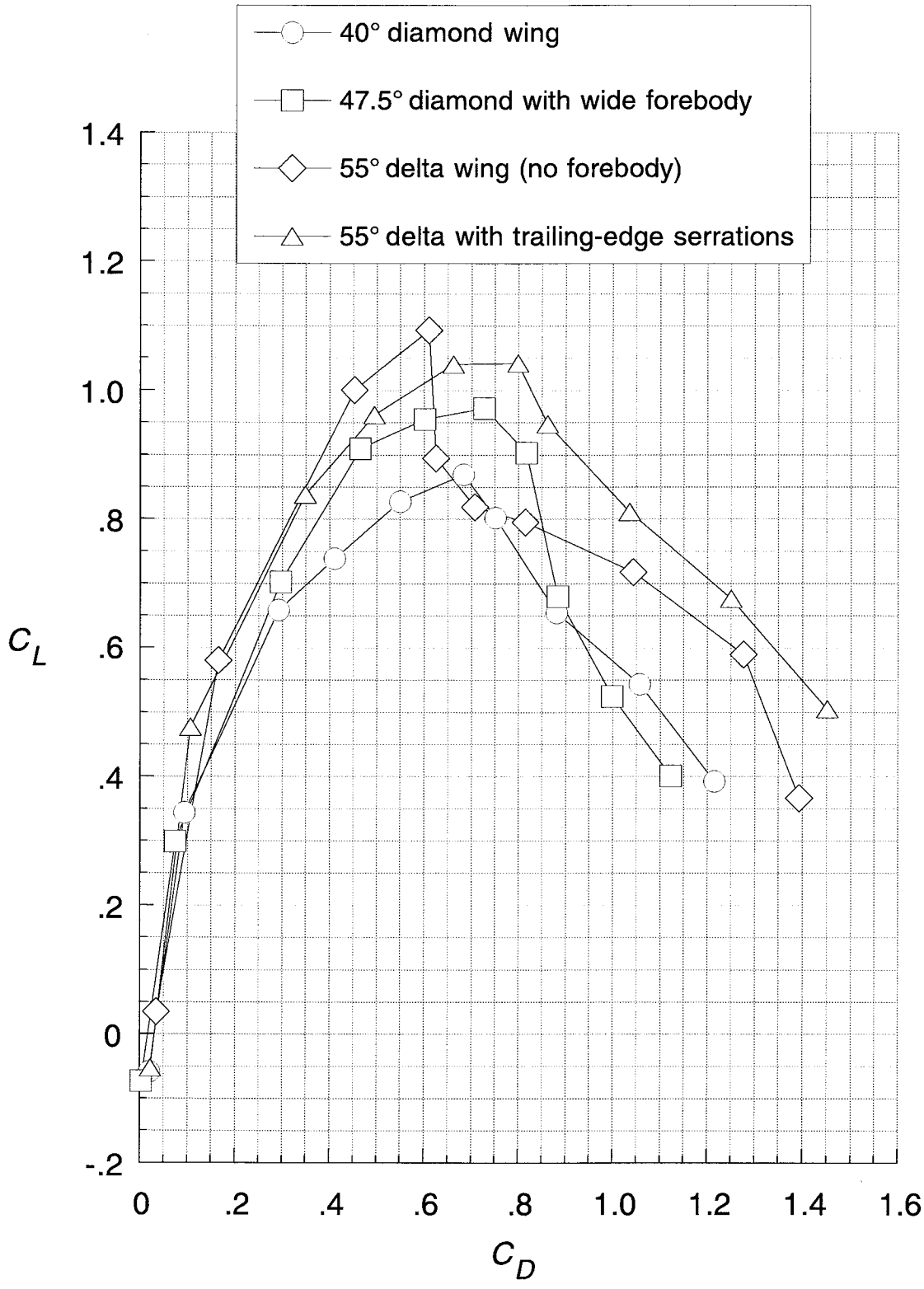

(b) Lift coefficient versus drag coefficient.

Figure 12. Continued.

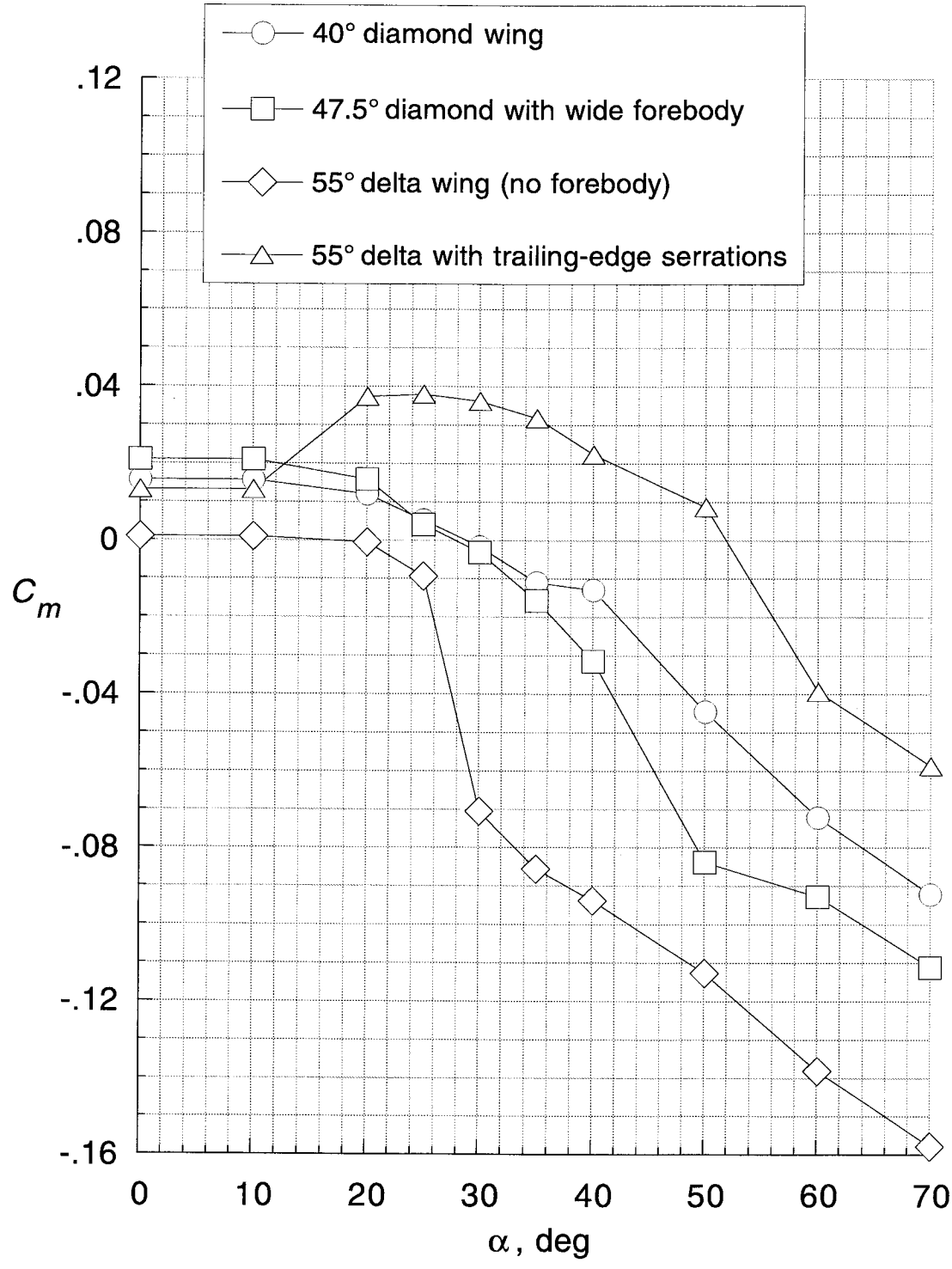

(c) Pitching-moment coefficient versus angle of attack.

Figure 12. Concluded.

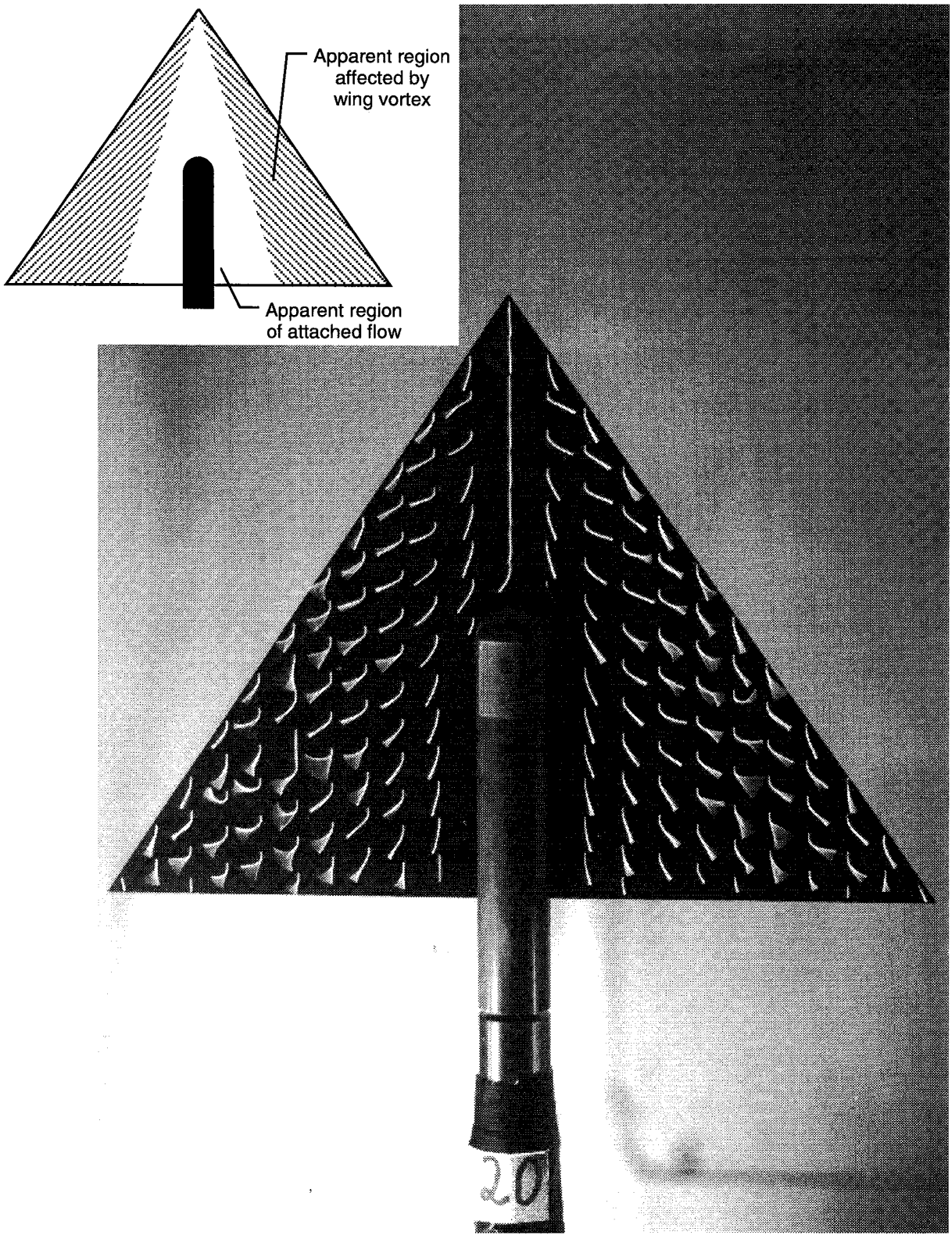

(a) $\alpha = 20°$.

Figure 13. Surface flow visualization on 55° delta wing.

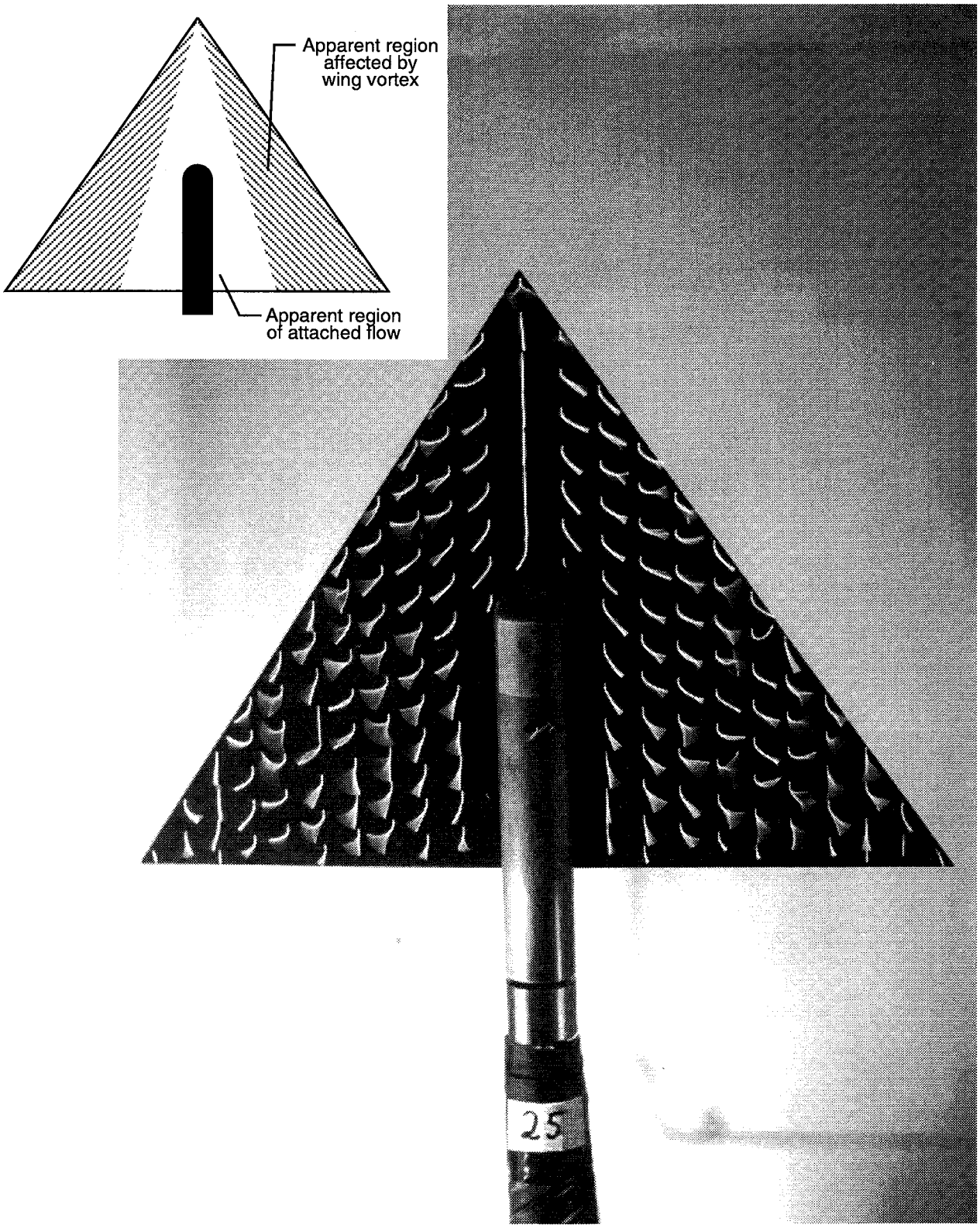

(b) $\alpha = 25°$.

Figure 13. Continued.

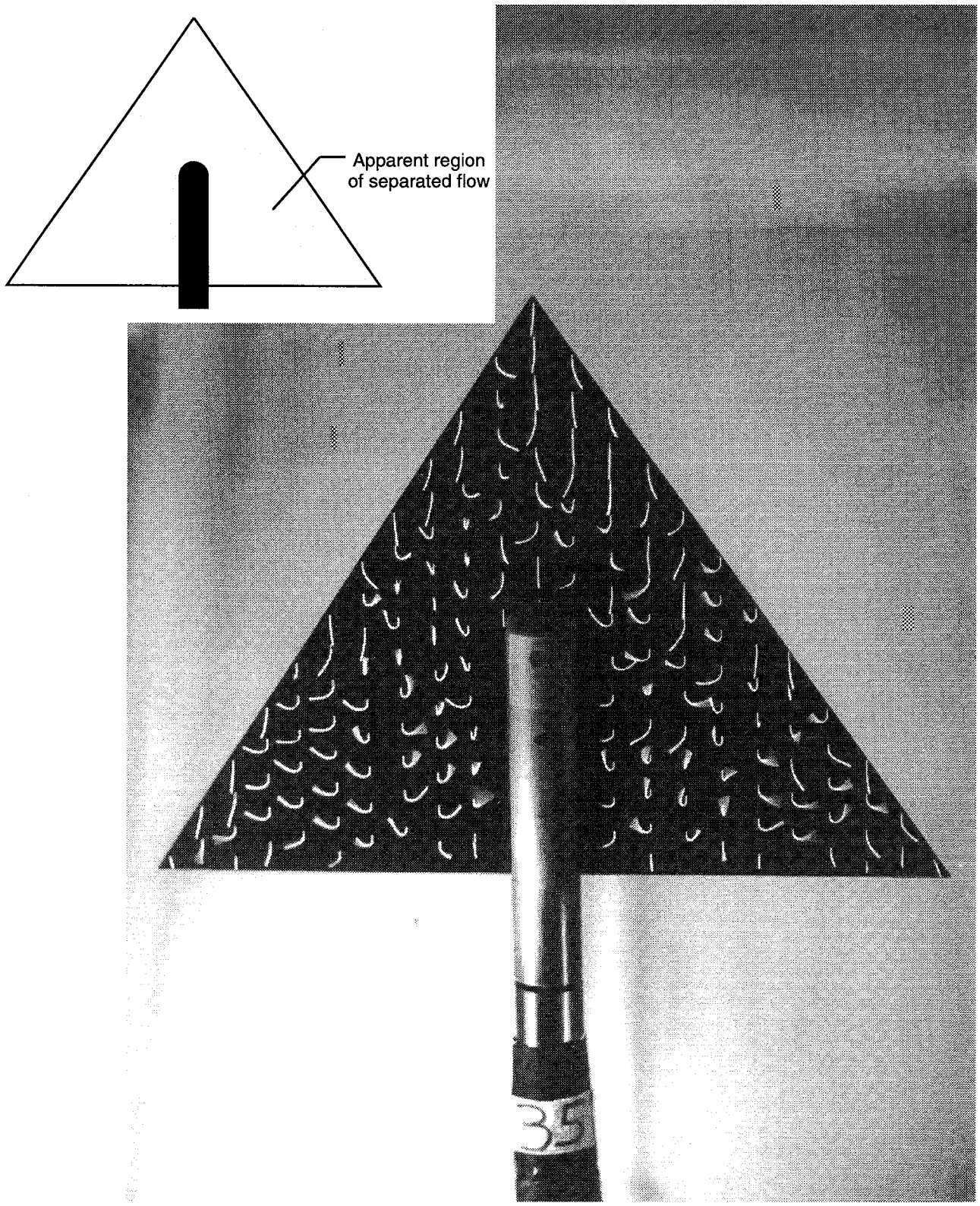

(c) $\alpha = 35°$.

Figure 13. Continued.

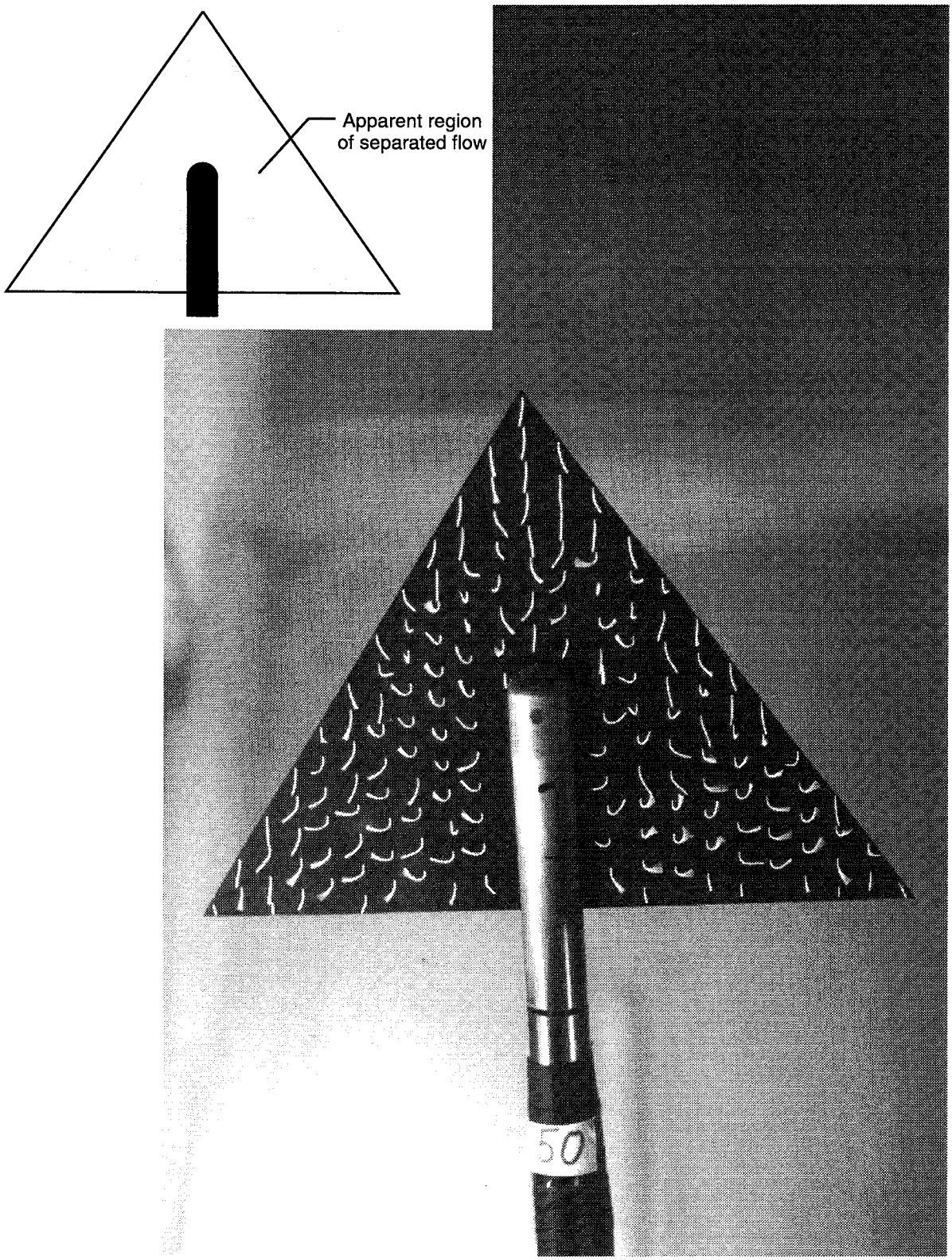

(d) $\alpha = 50°$.

Figure 13. Concluded.

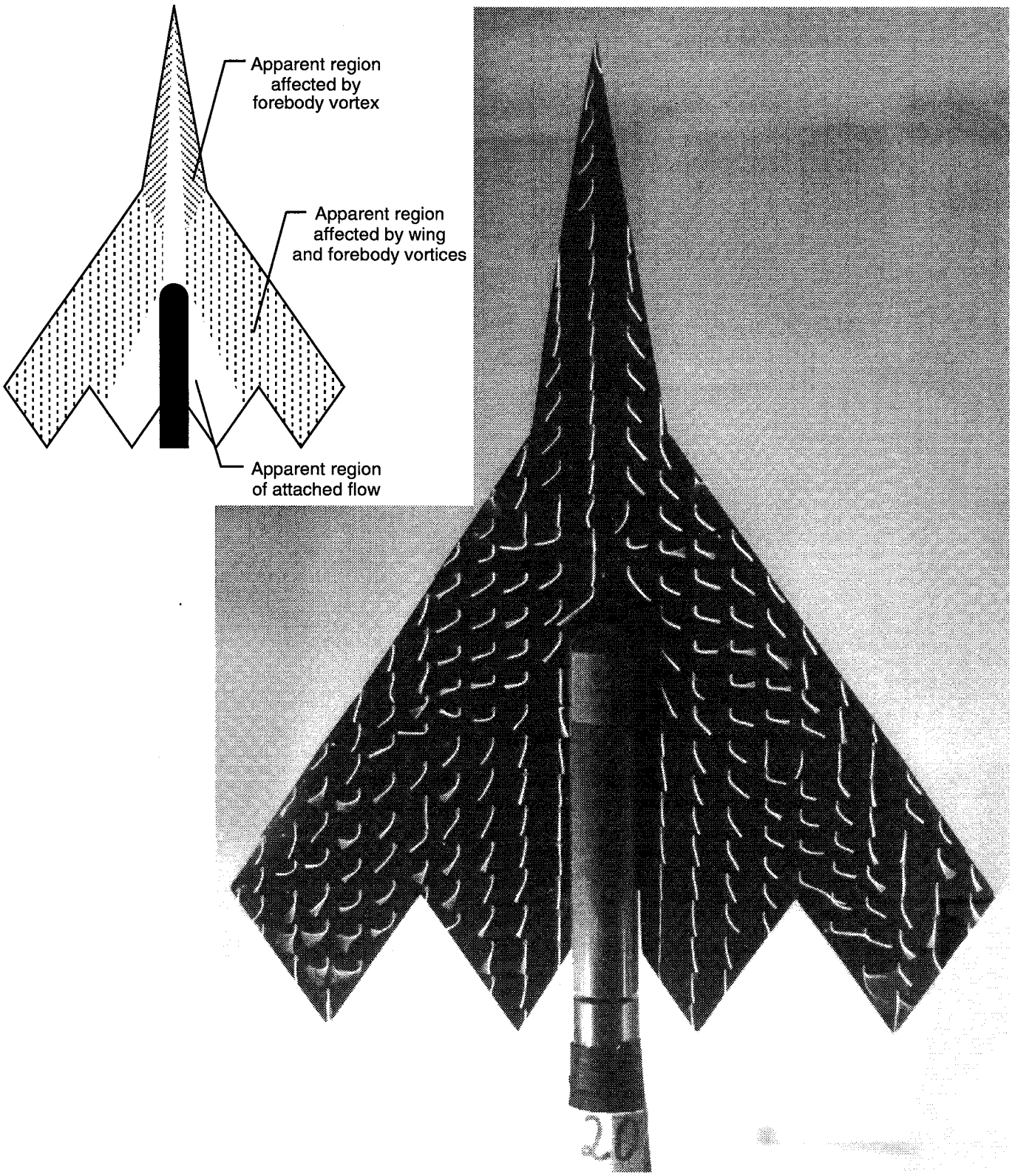

(a) $\alpha = 20°$.

Figure 14. Surface flow visualization on 55° delta with trailing-edge serrations.

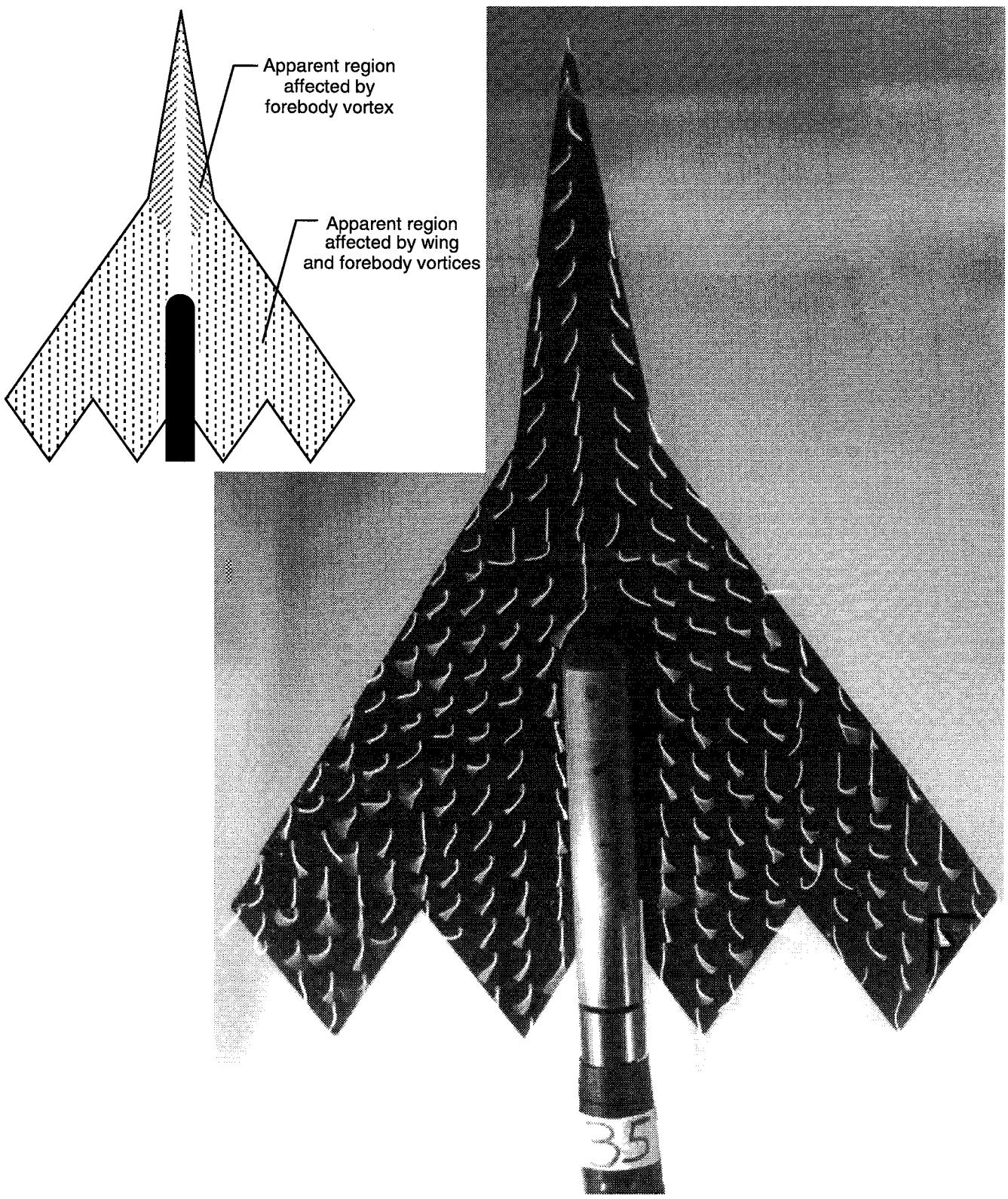

(b) $\alpha = 35°$.

Figure 14. Continued.

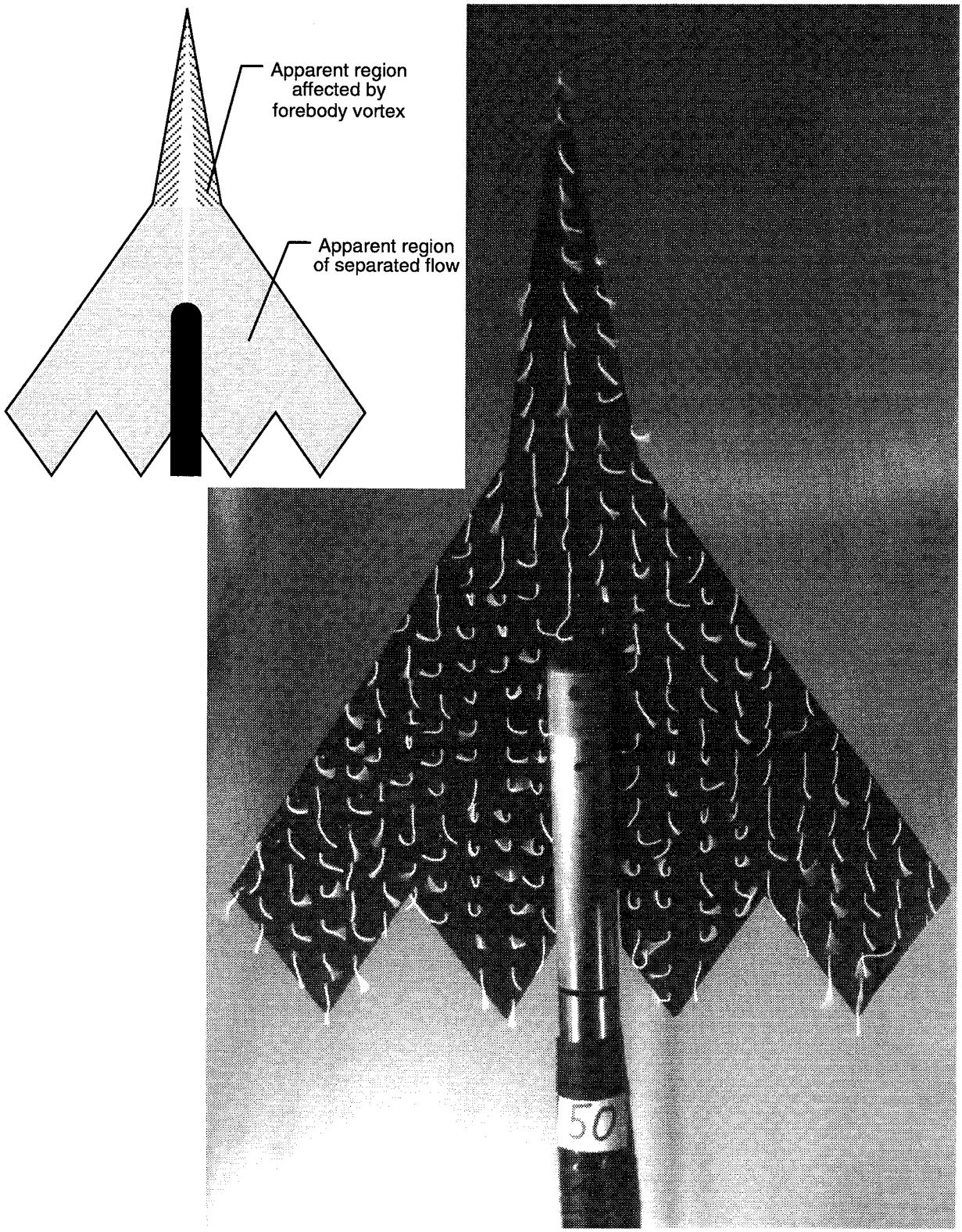

(c) $\alpha = 50°$.

Figure 14. Concluded.

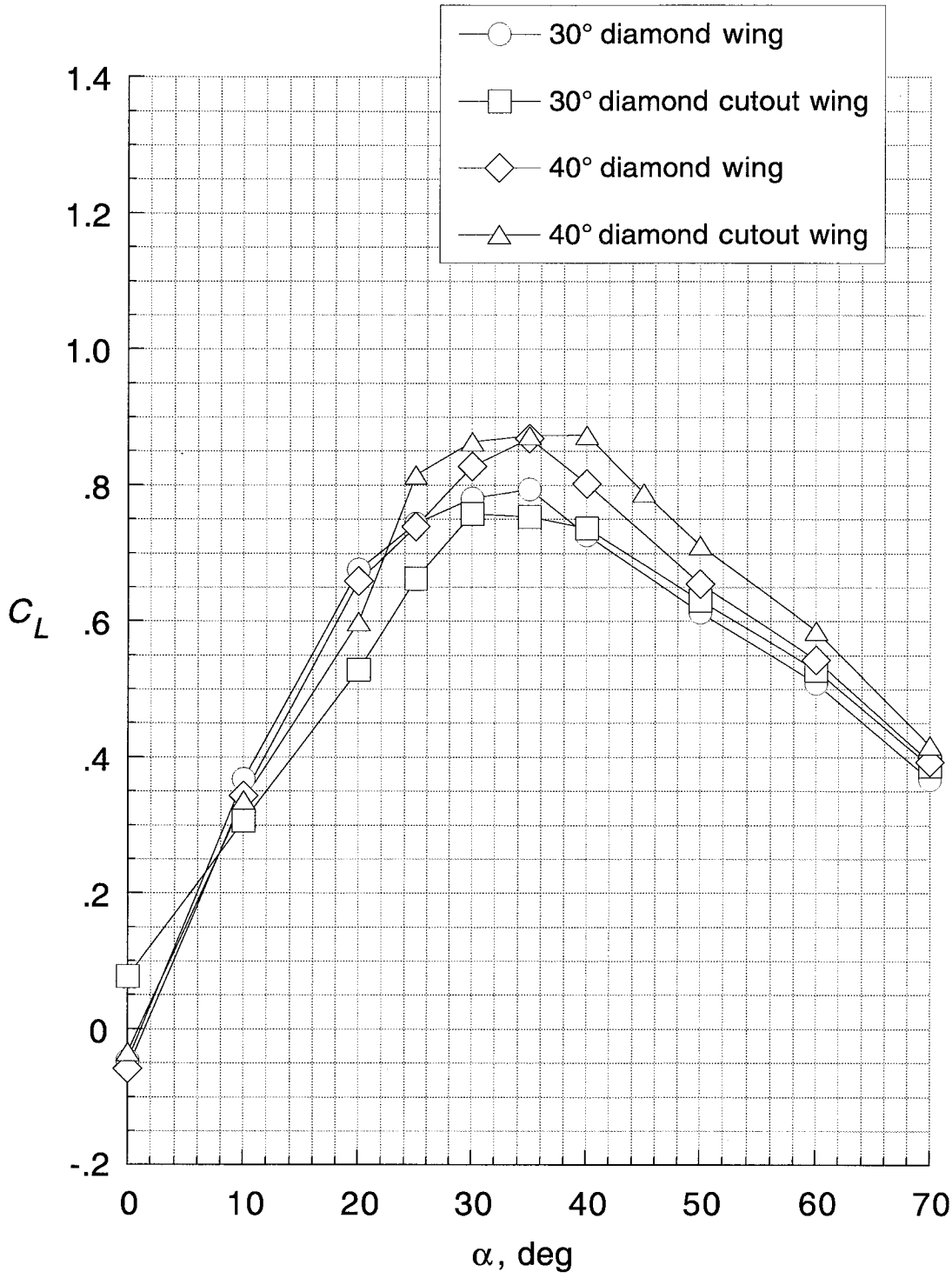

(a) Lift coefficient versus angle of attack.

Figure 15. Longitudinal data illustrating original cutout effects.

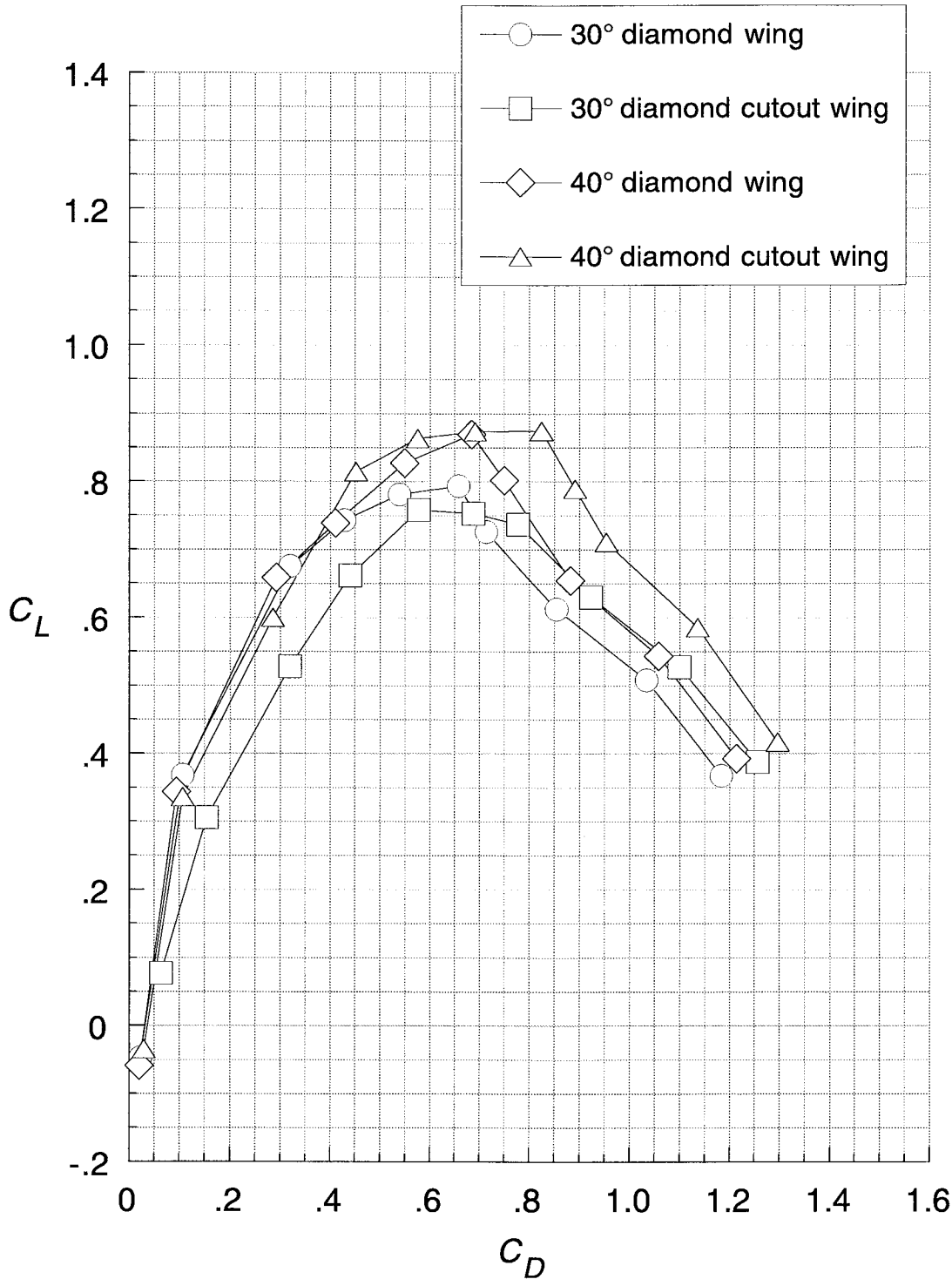

(b) Lift coefficient versus drag coefficient.

Figure 15. Continued.

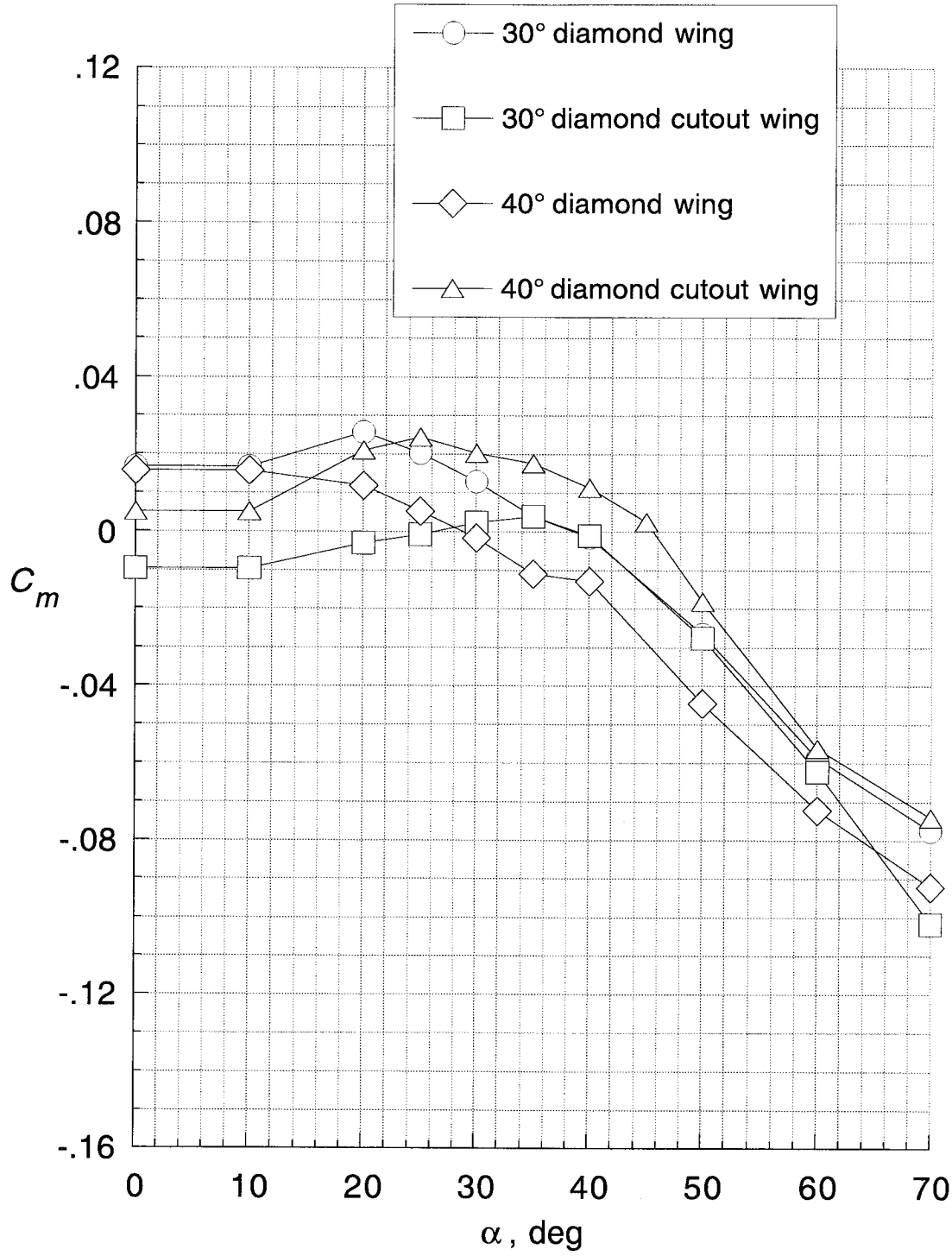

(c) Pitching-moment coefficient versus angle of attack.

Figure 15. Concluded.

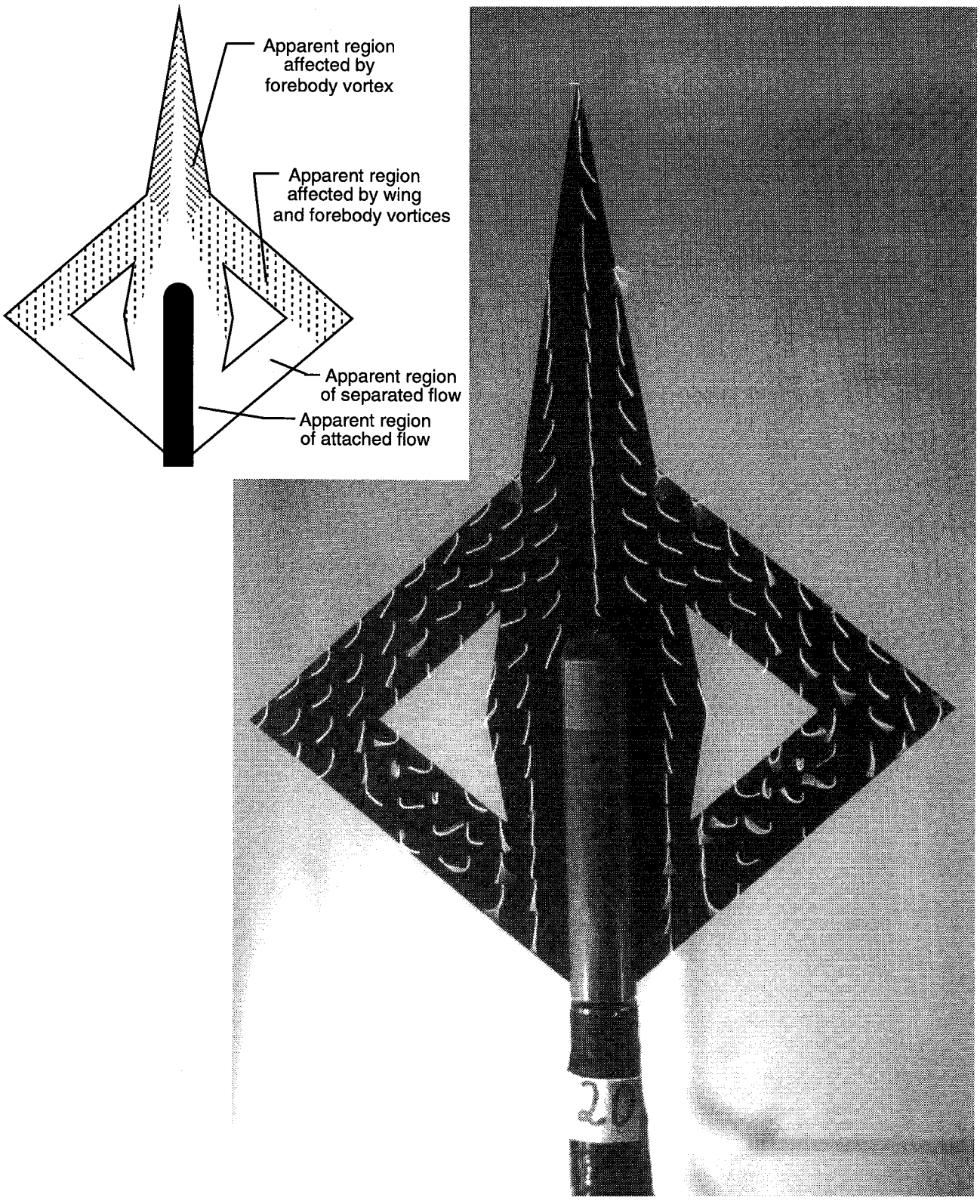

(a) $\alpha = 20°$.

Figure 16. Surface flow visualization on 40° diamond cutout wing.

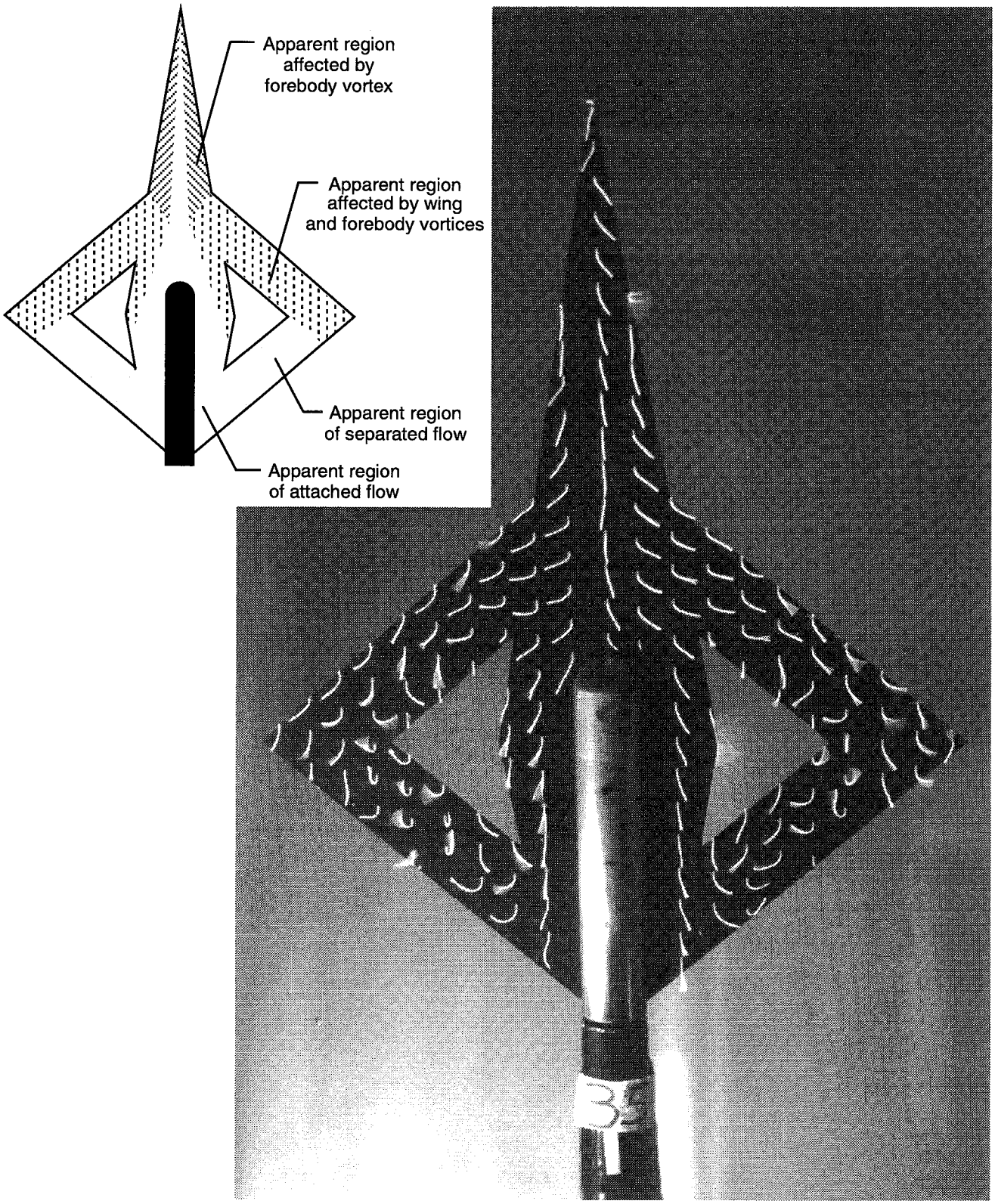

(b) $\alpha = 35°$.

Figure 16. Continued.

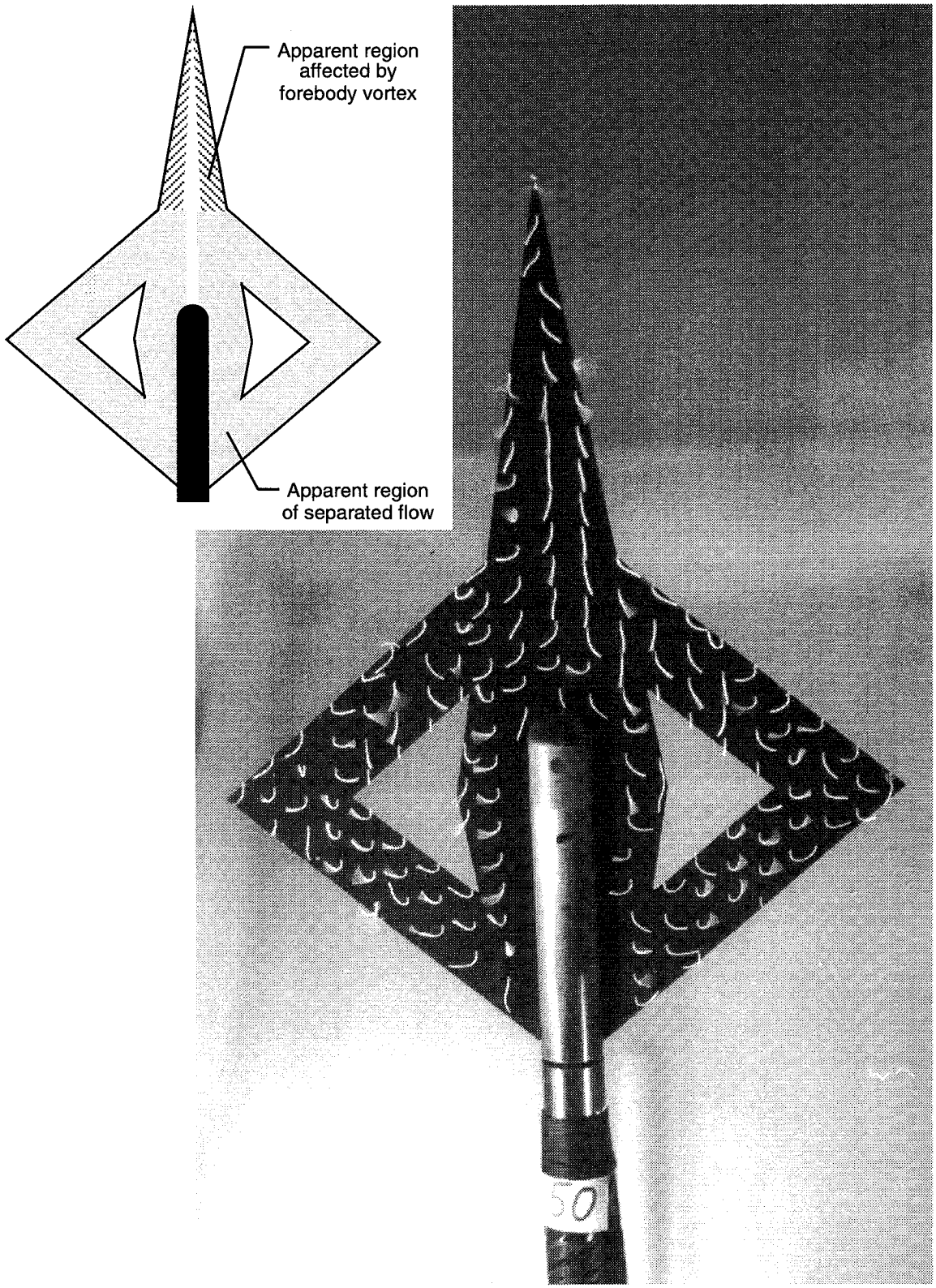

(c) $\alpha = 50°$.

Figure 16. Concluded.

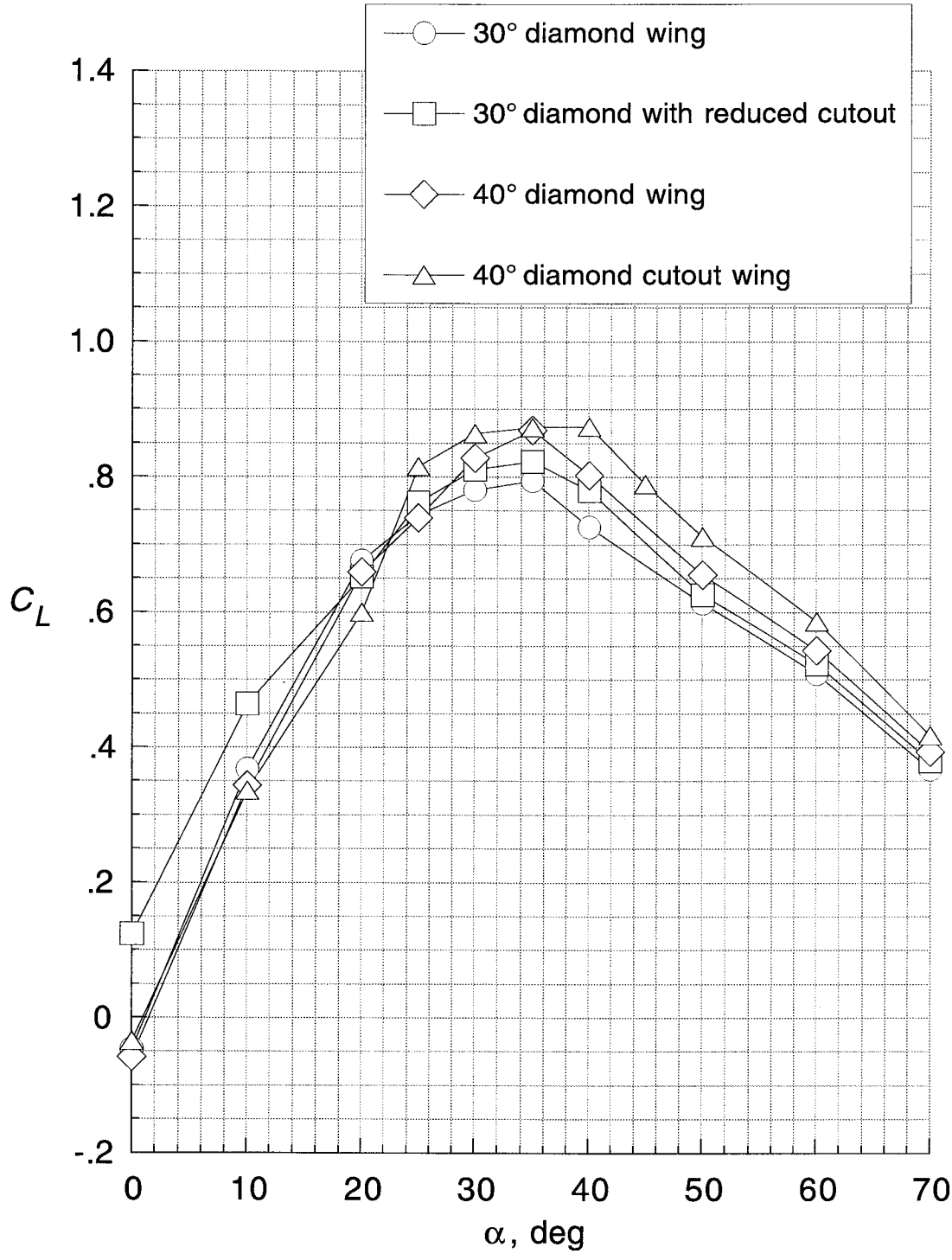

(a) Lift coefficient versus angle of attack.

Figure 17. Longitudinal data illustrating wing leading-edge sweep effect on cutout.

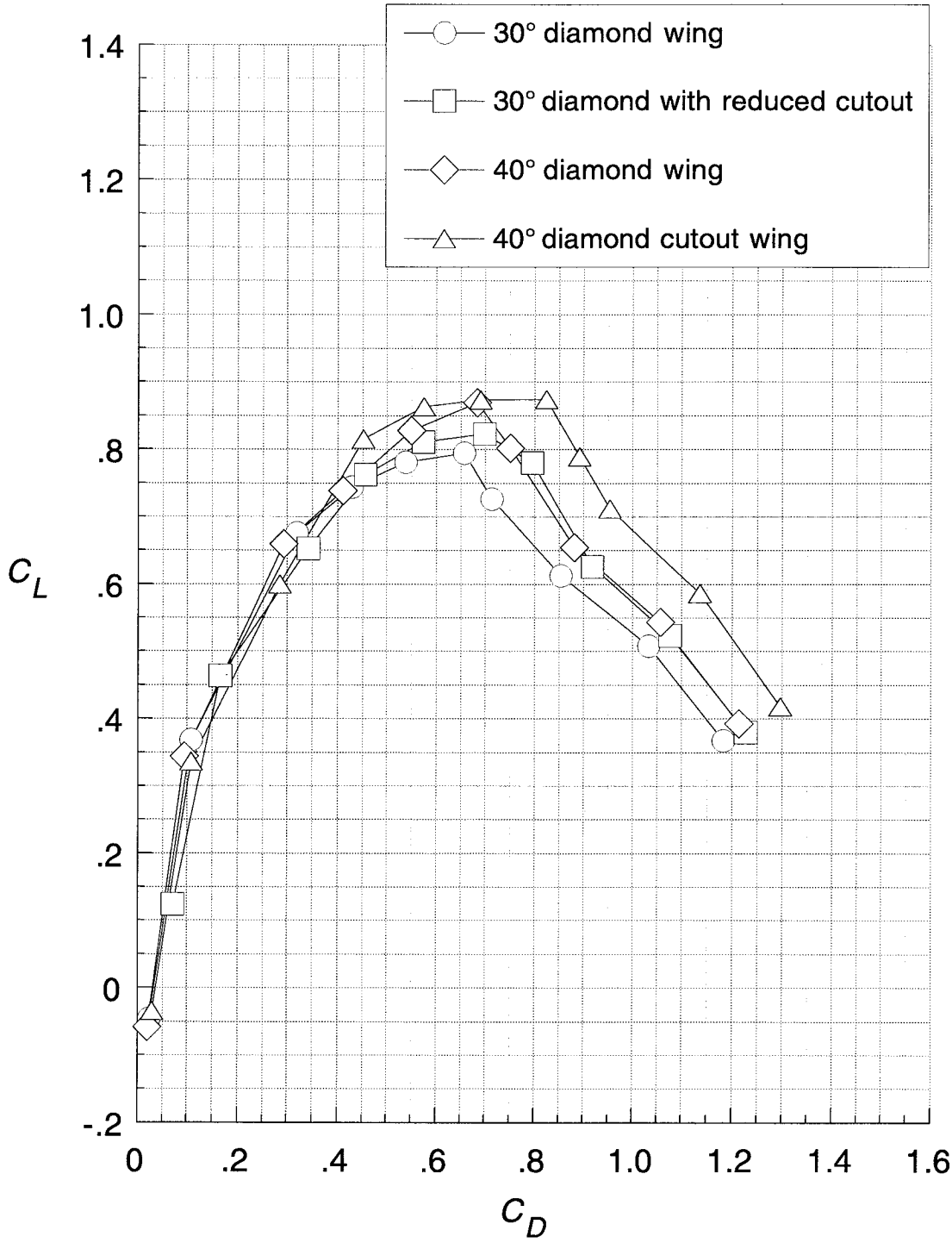

(b) Lift coefficient versus drag coefficient.

Figure 17. Continued.

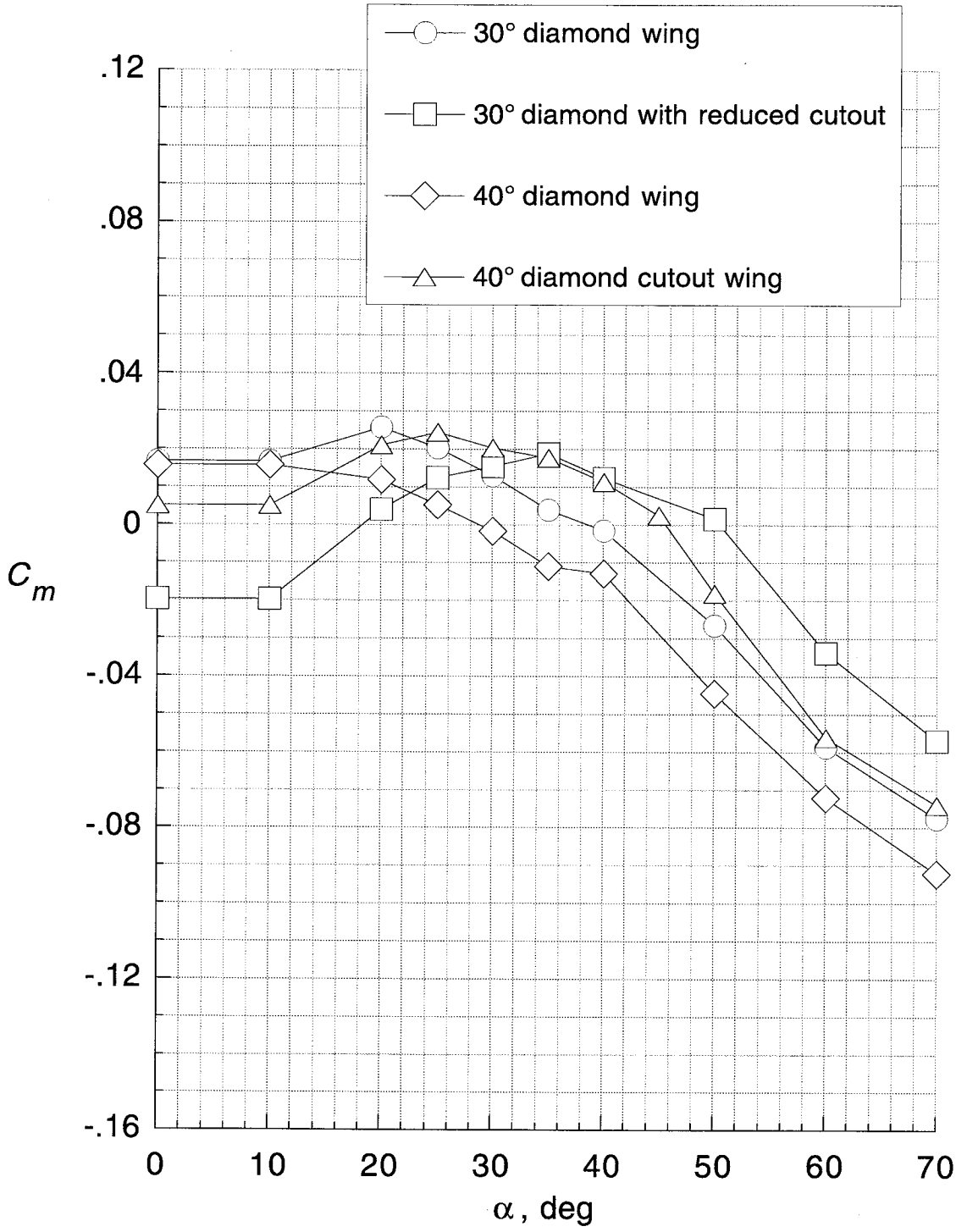

(c) Pitching-moment coefficient versus angle of attack.

Figure 17. Concluded.

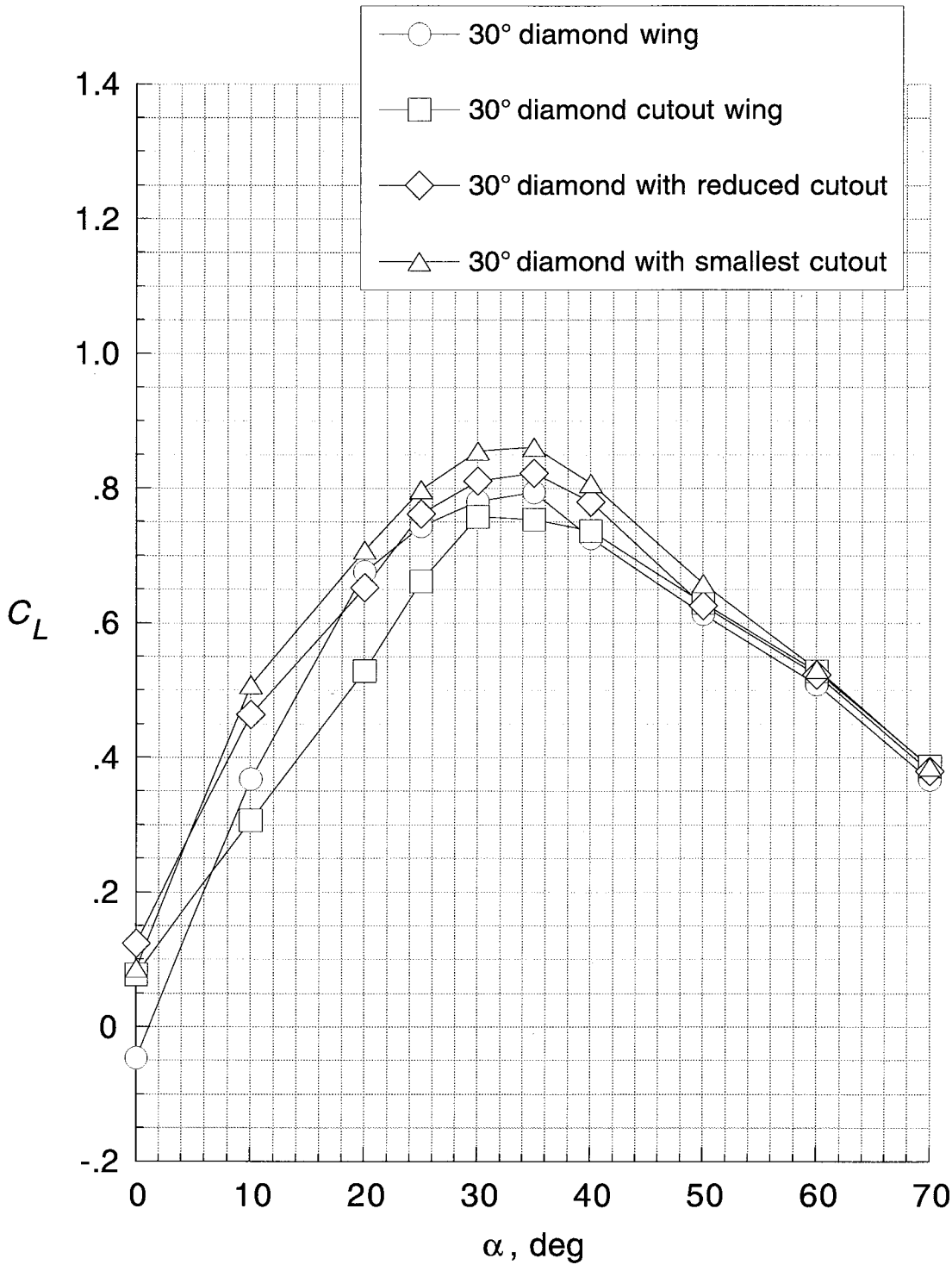

(a) Lift coefficient versus angle of attack.

Figure 18. Longitudinal data illustrating cutout size effects.

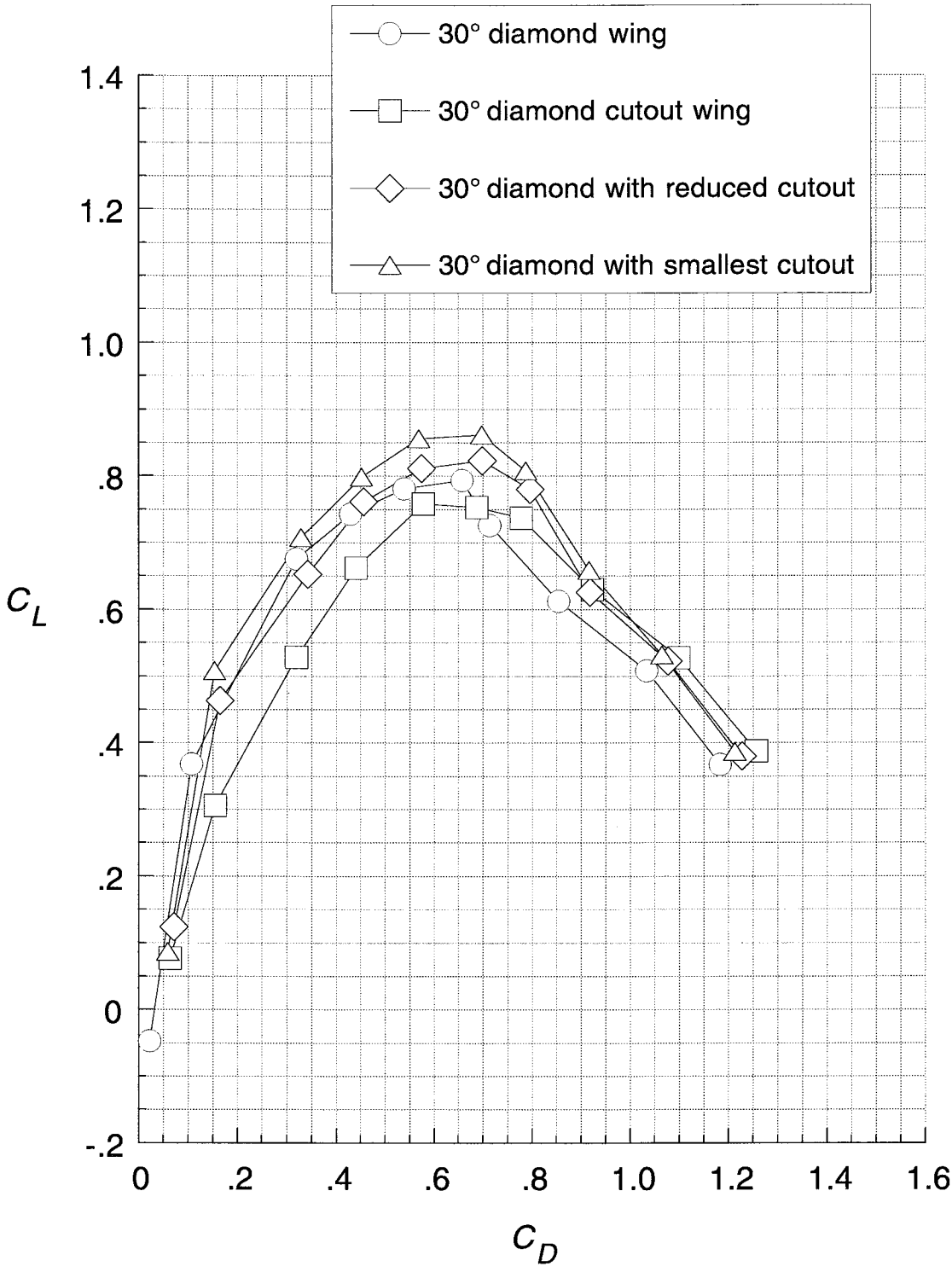

(b) Lift coefficient versus drag coefficient.

Figure 18. Continued.

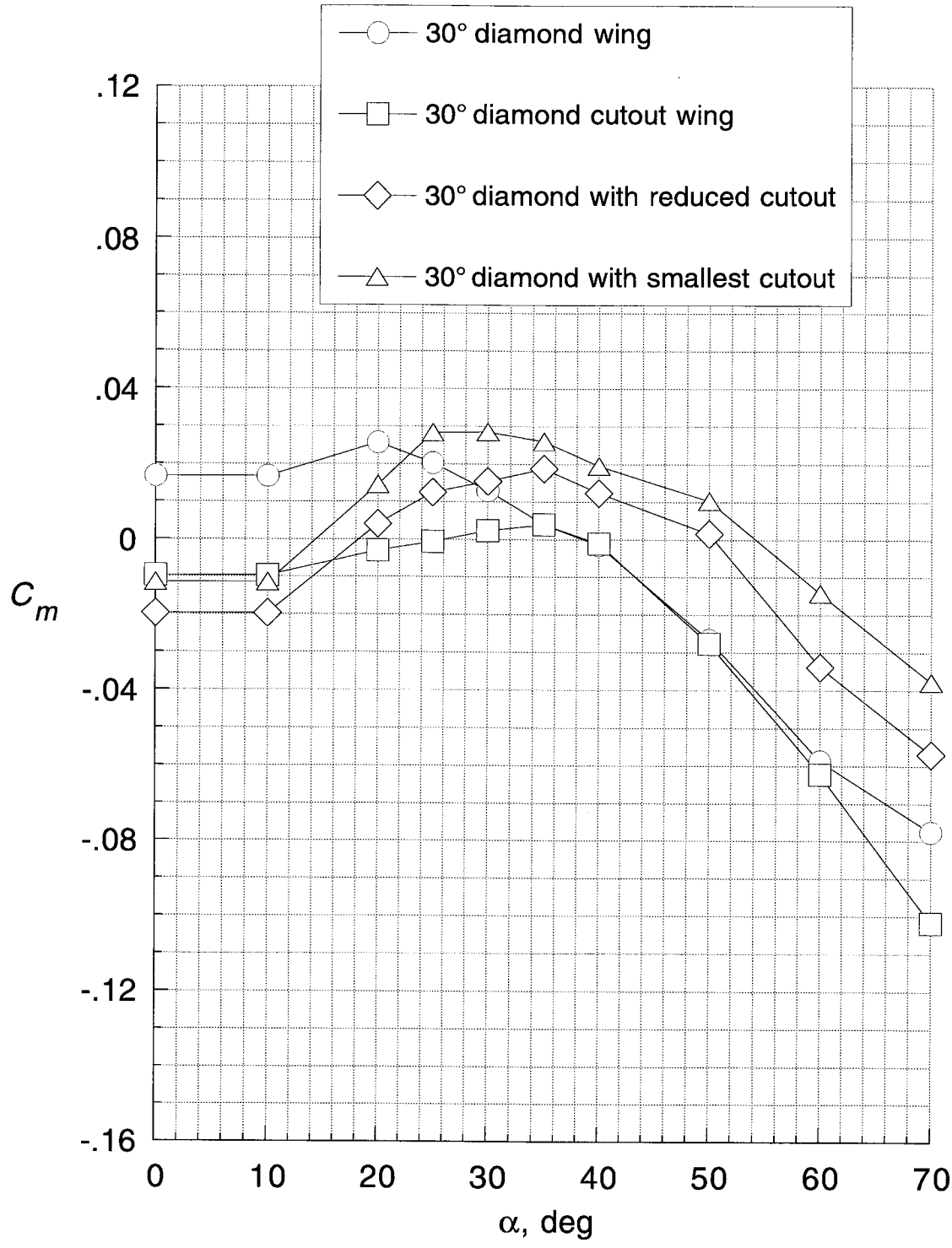

(c) Pitching-moment coefficient versus angle of attack.

Figure 18. Concluded.

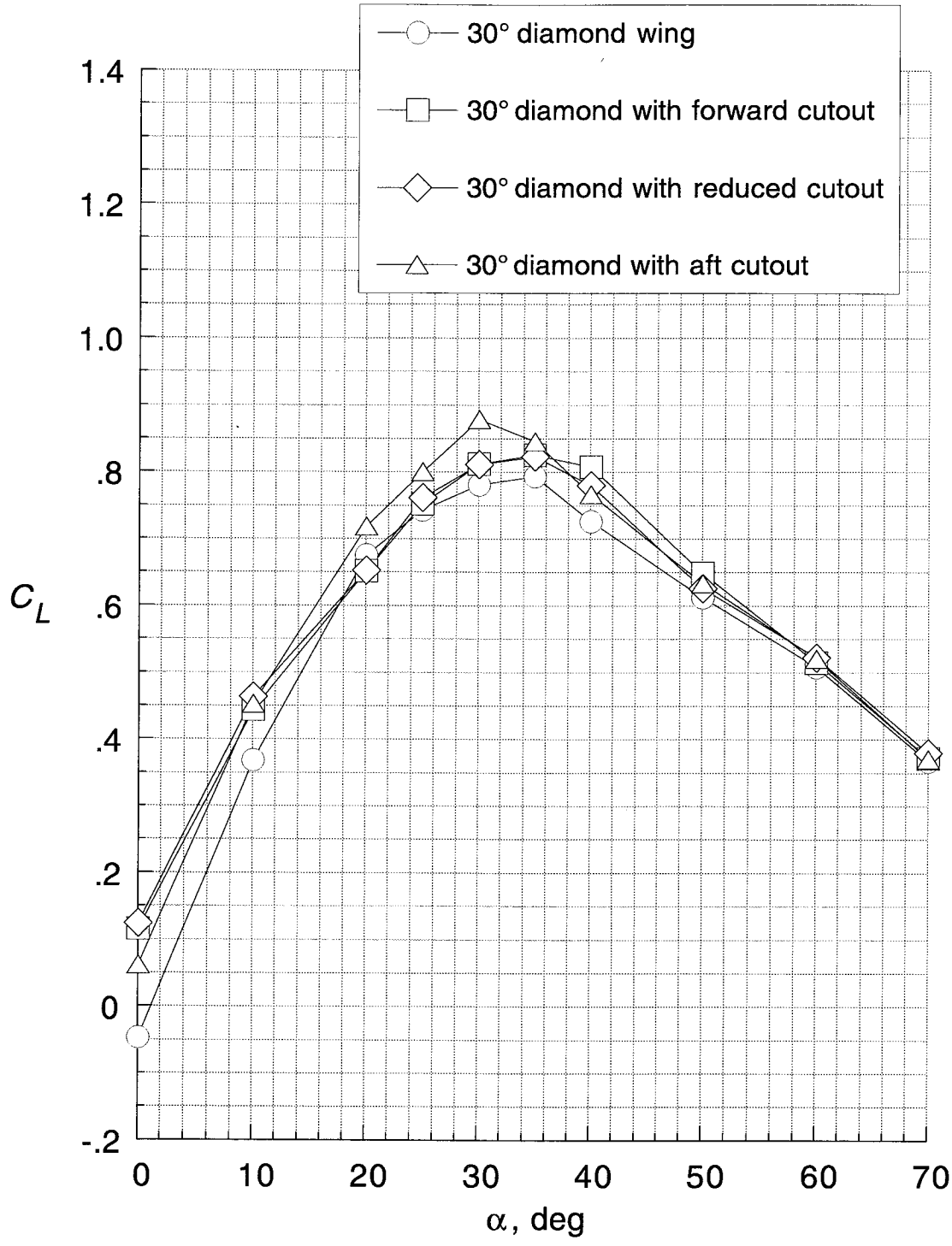

(a) Lift coefficient versus angle of attack.

Figure 19. Longitudinal data illustrating cutout location effects.

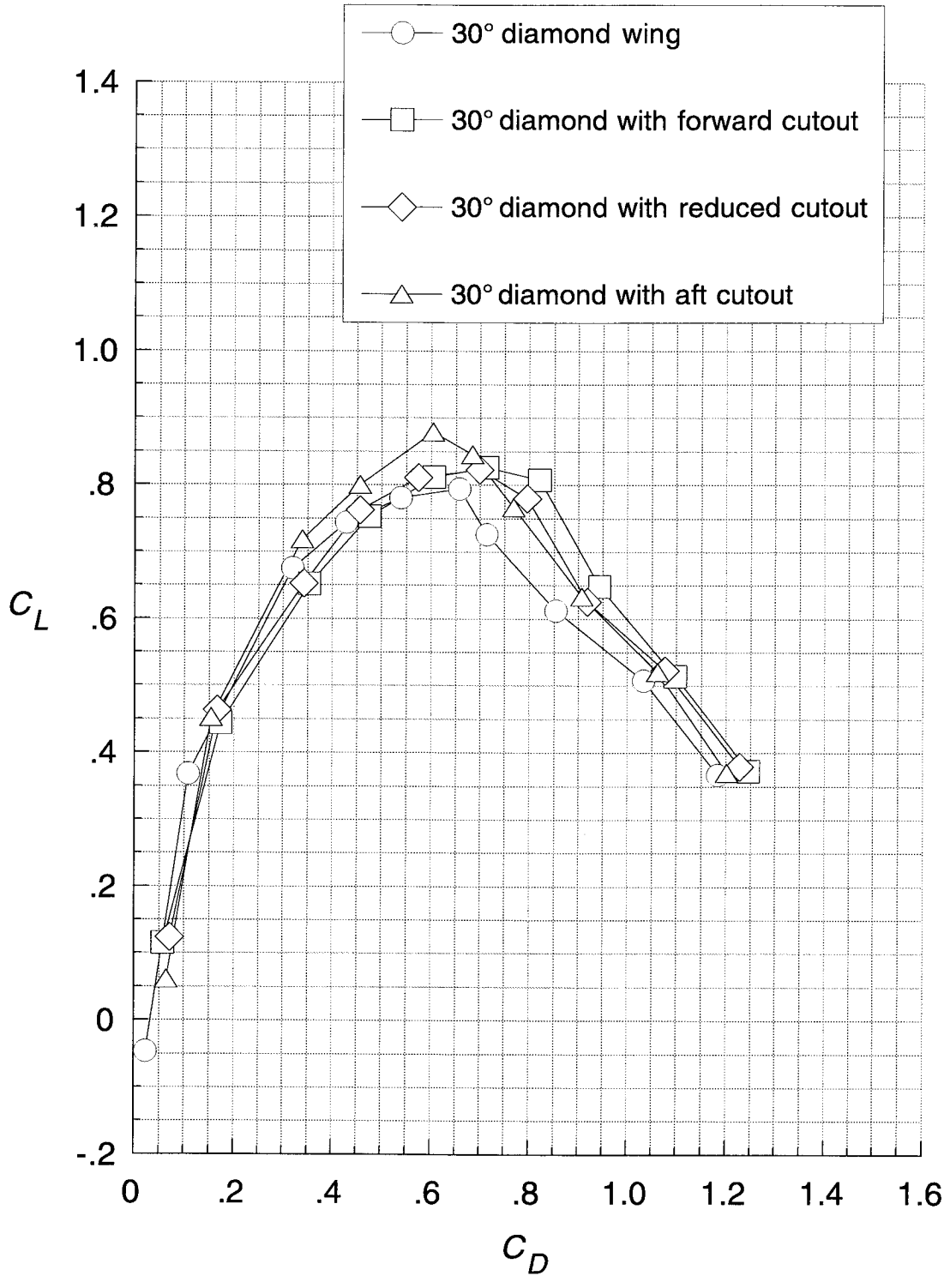

(b) Lift coefficient versus drag coefficient.

Figure 19. Continued.

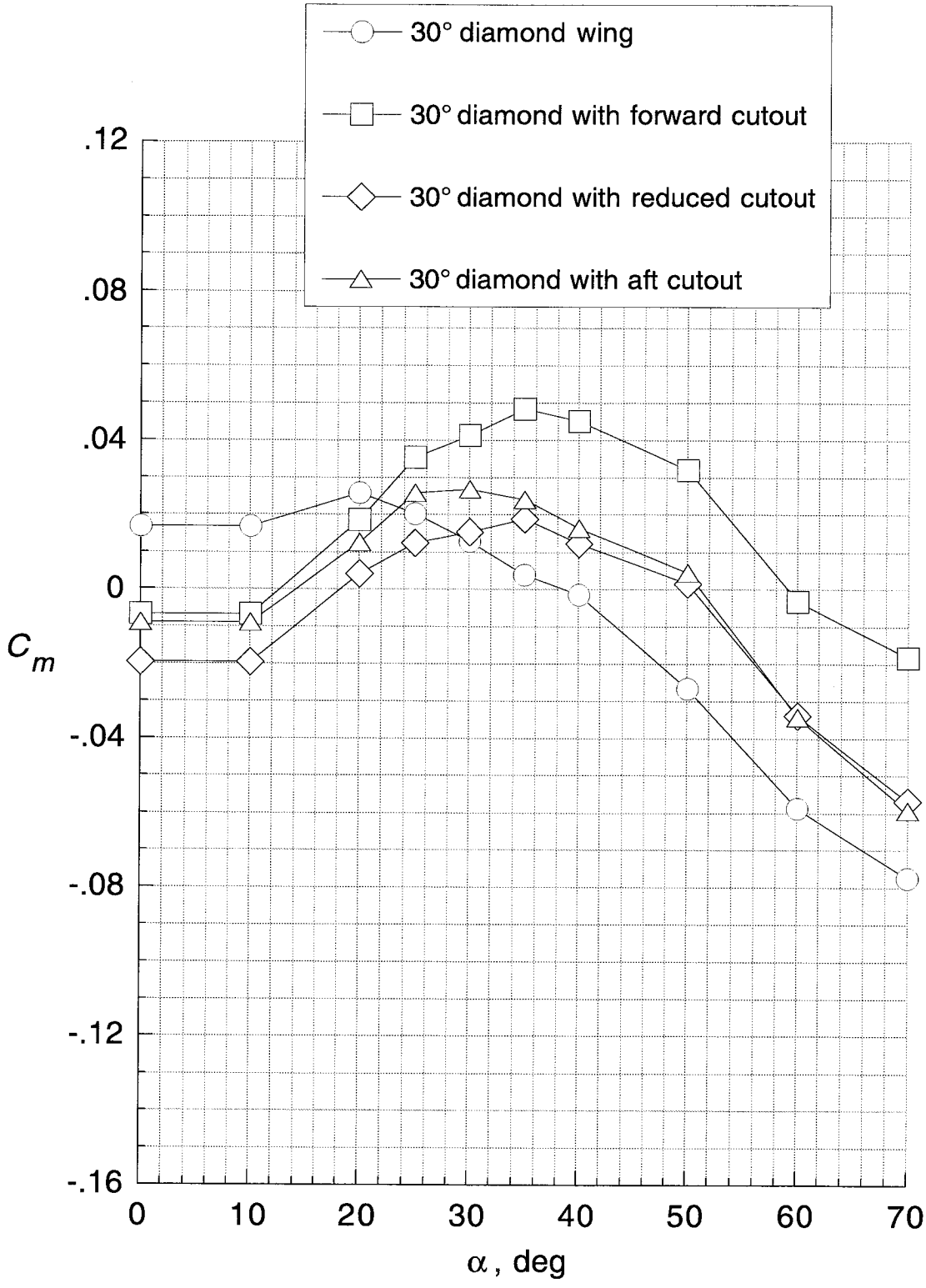

(c) Pitching-moment coefficient versus angle of attack.

Figure 19. Concluded.

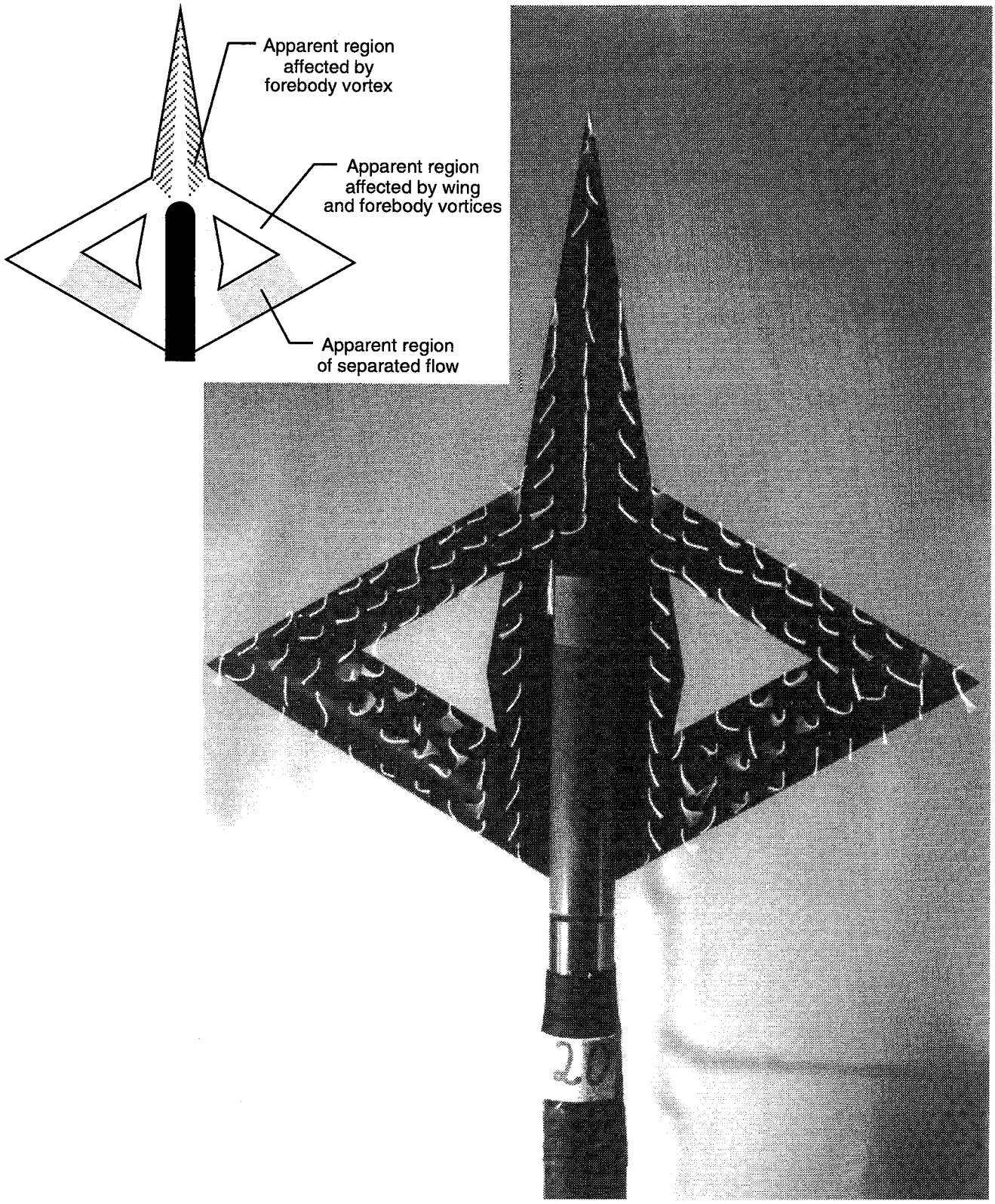

(a) $\alpha = 20°$.

Figure 20. Surface flow visualization on 30° diamond with forward cutout.

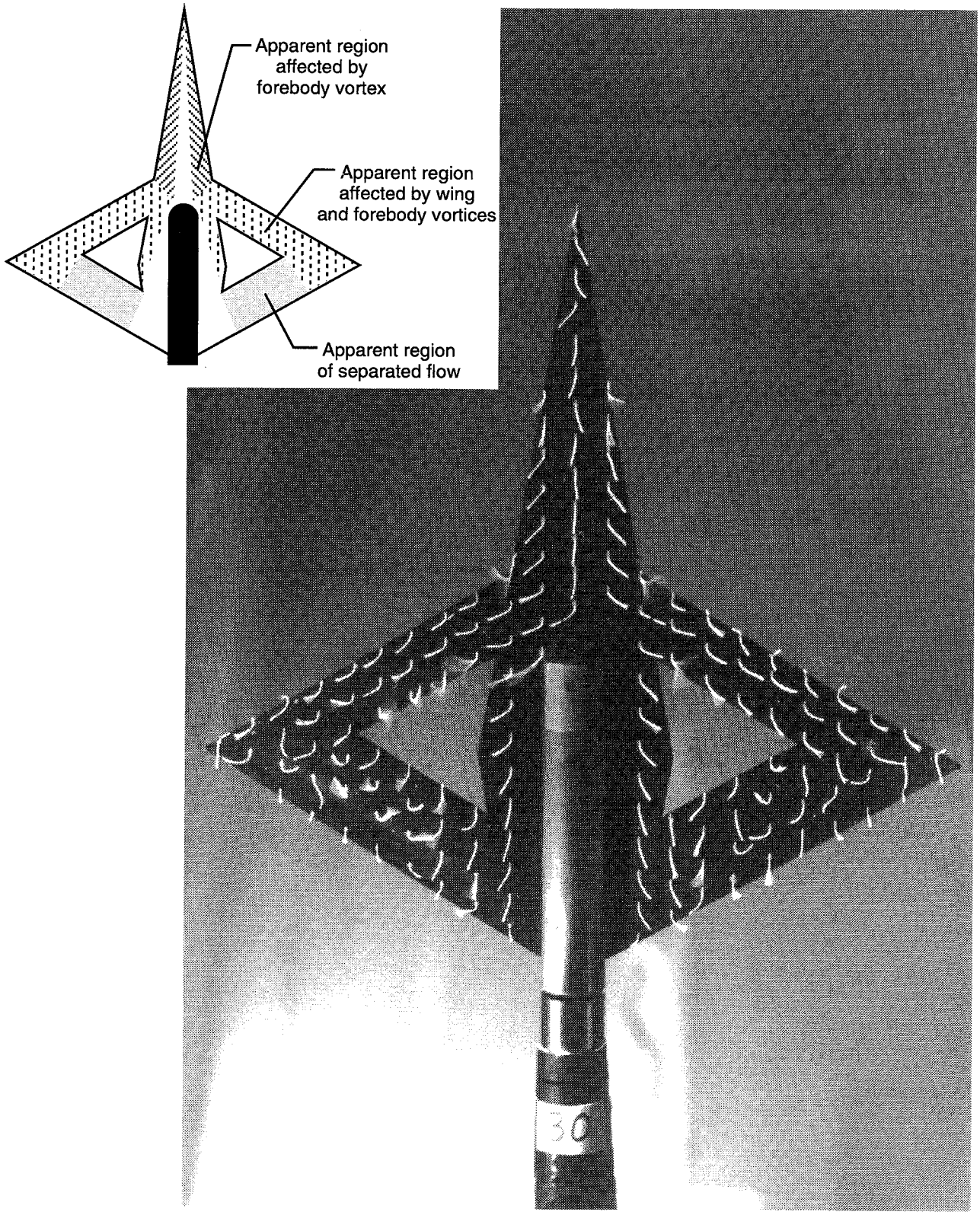

(b) $\alpha = 30°$.

Figure 20. Continued.

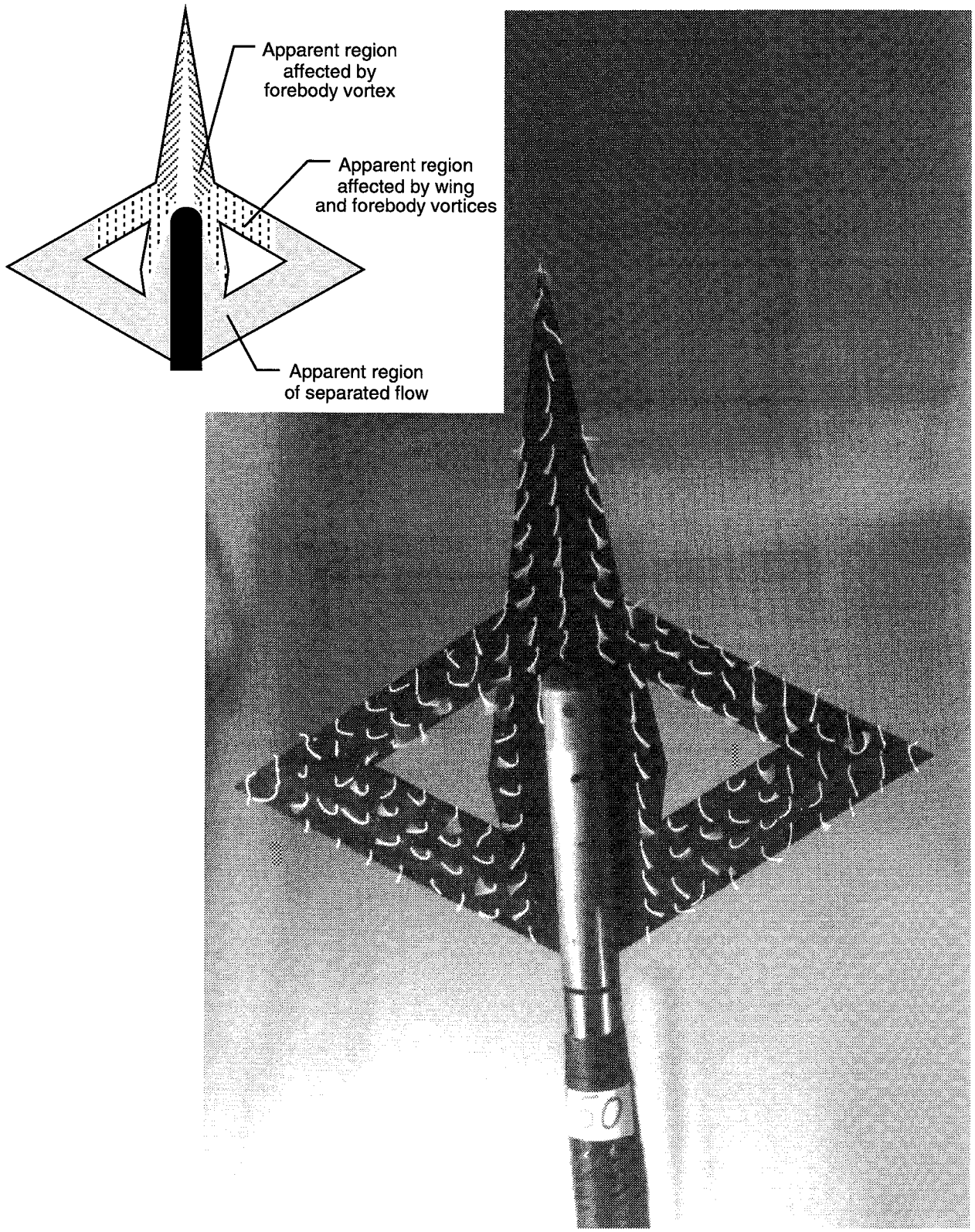

(c) $\alpha = 50°$.

Figure 20. Concluded.

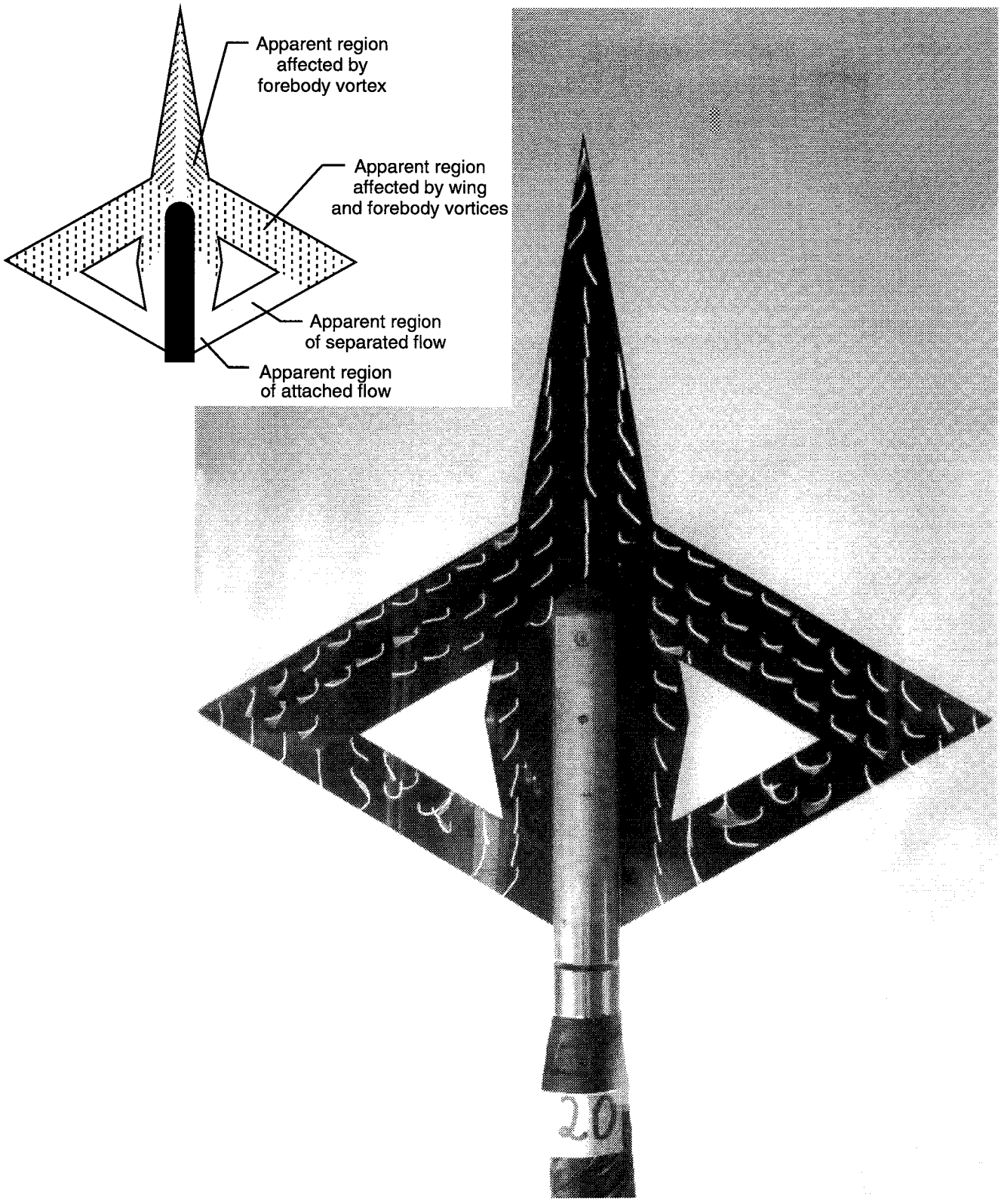

(a) $\alpha = 20°$.

Figure 21. Surface flow visualization on 30° diamond with aft cutout.

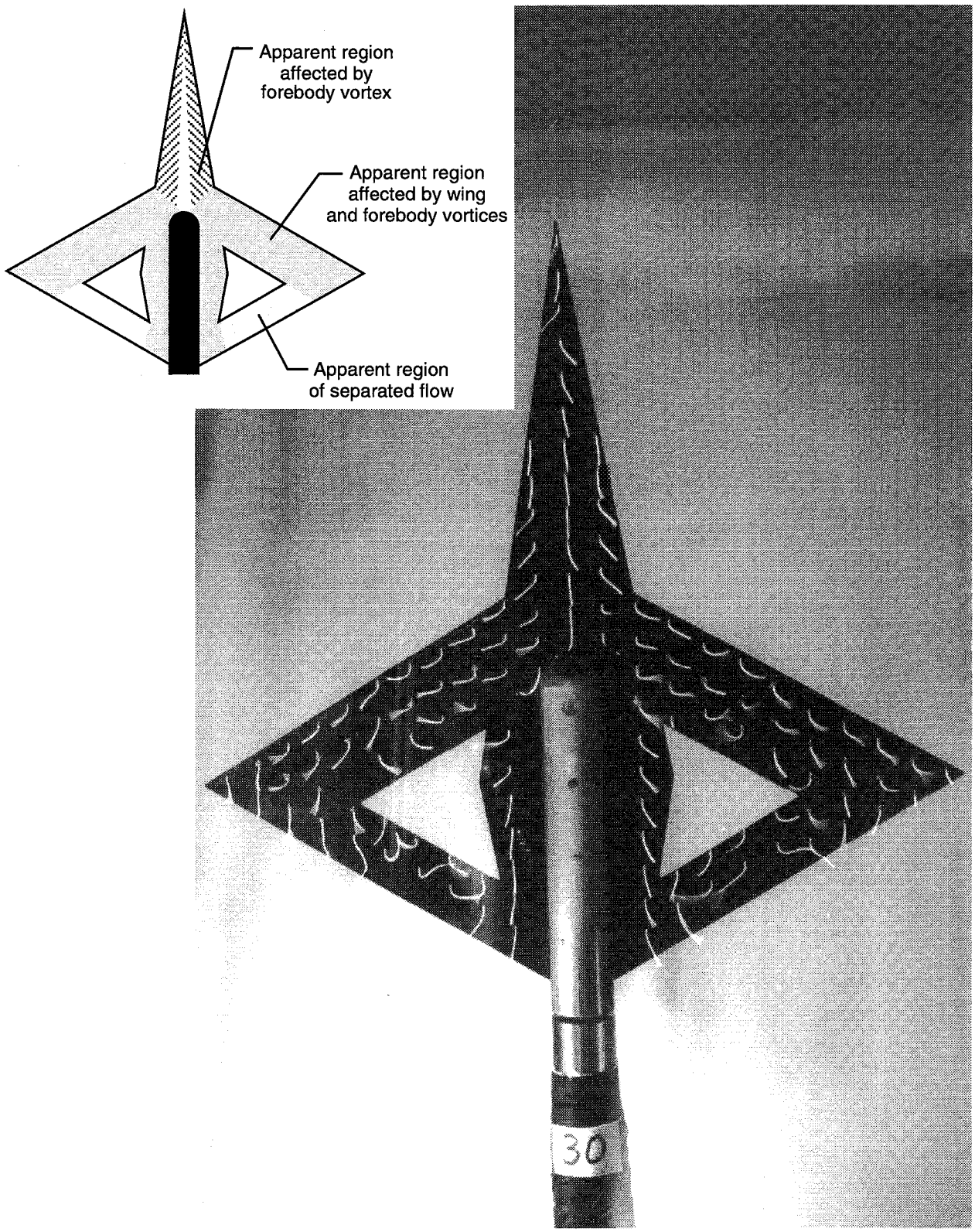

(b) $\alpha = 30°$.

Figure 21. Continued.

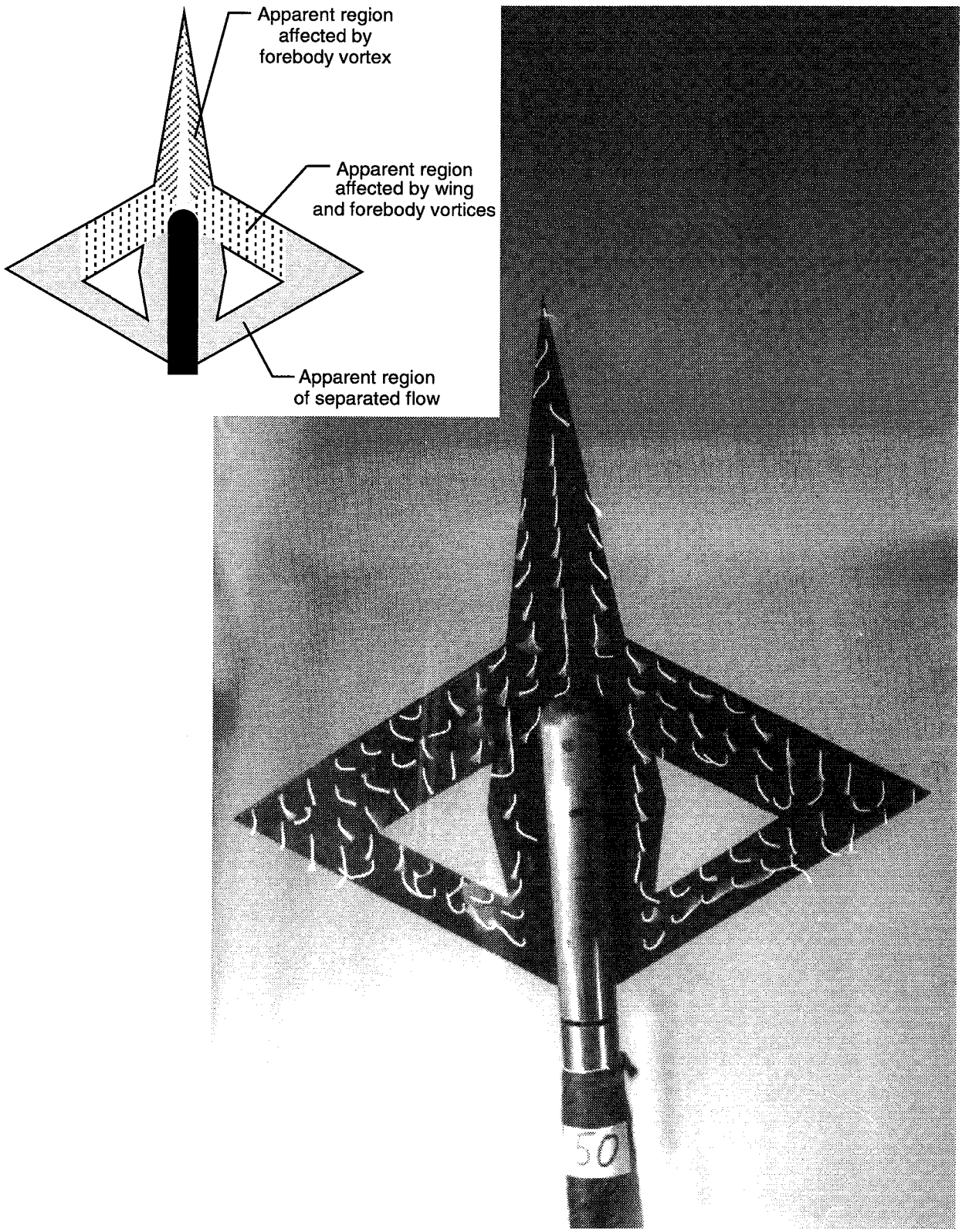

(c) $\alpha = 50°$.

Figure 21. Concluded.

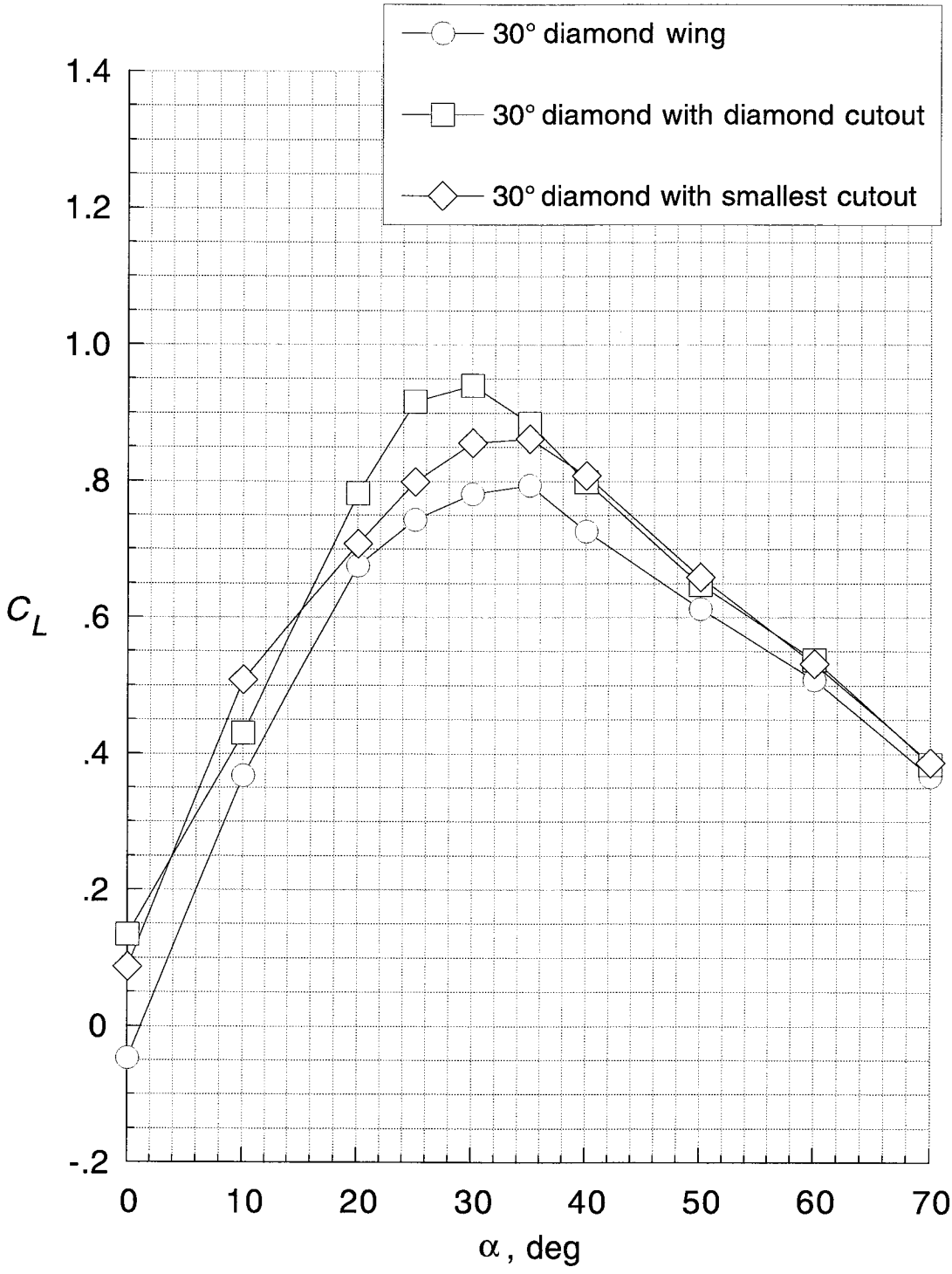

(a) Lift coefficient versus angle of attack.

Figure 22. Longitudinal data illustrating cutout shape effects.

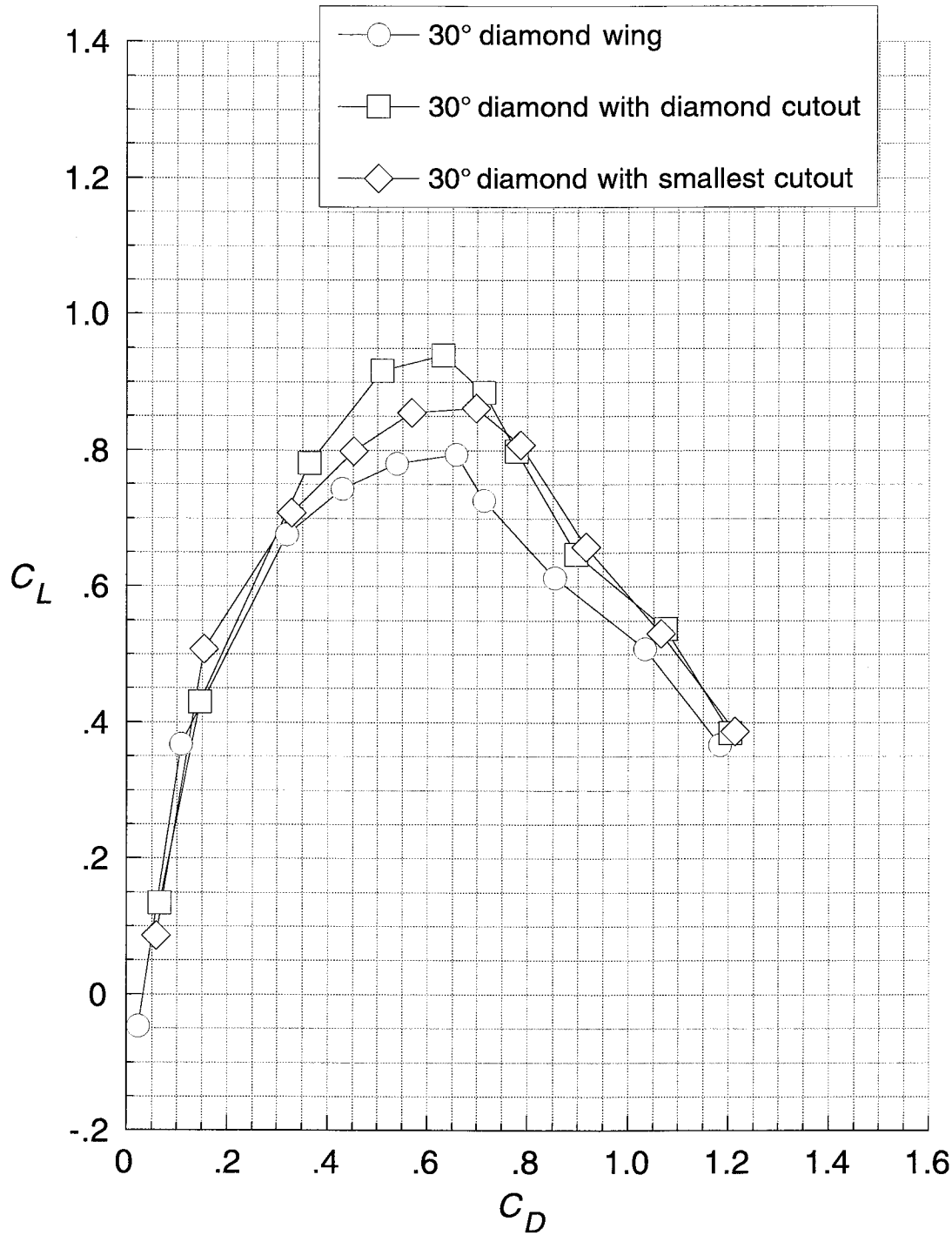

(b) Lift coefficient versus drag coefficient.

Figure 22. Continued.

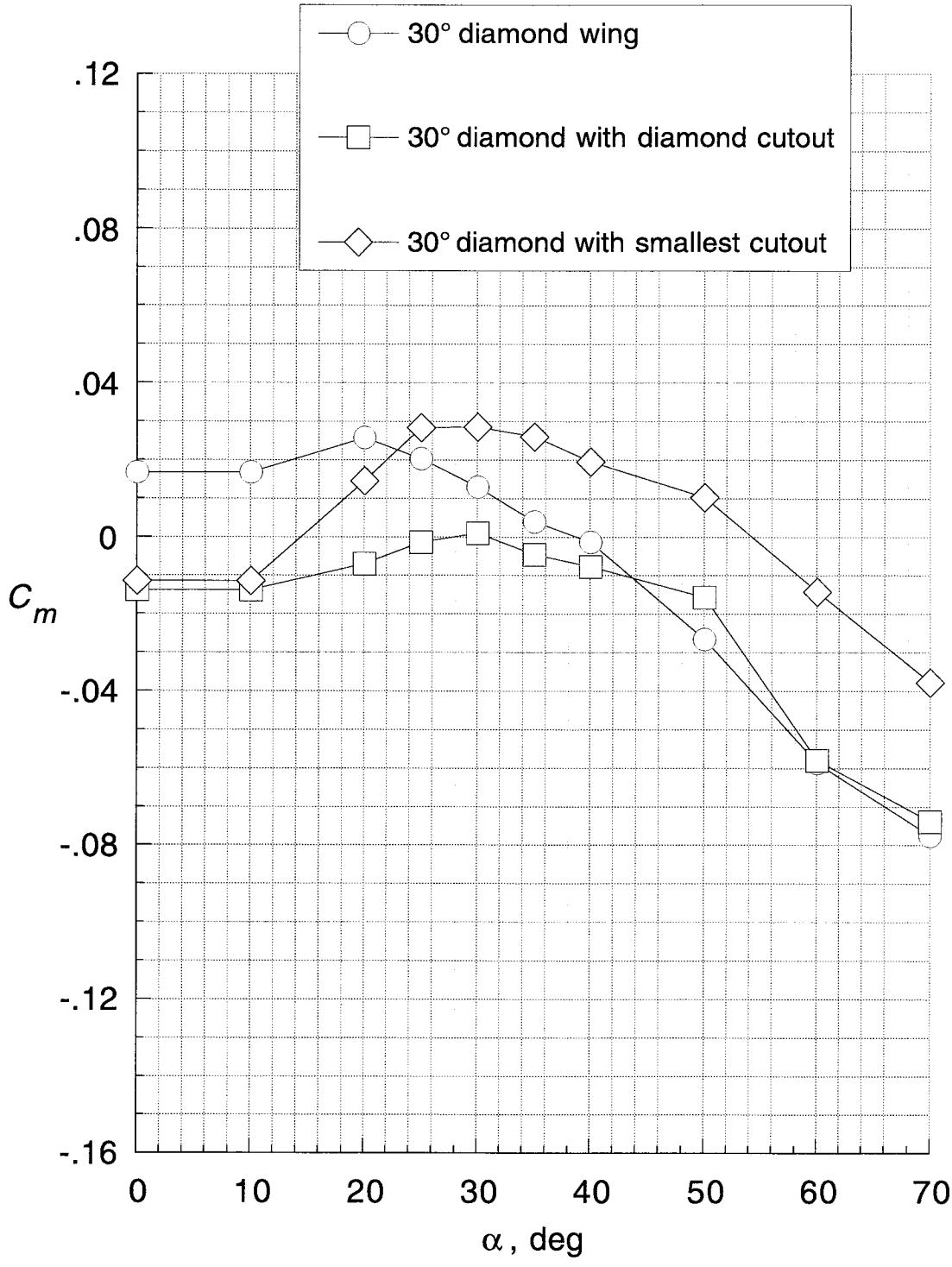

(c) Pitching-moment coefficient versus angle of attack.

Figure 22. Concluded.

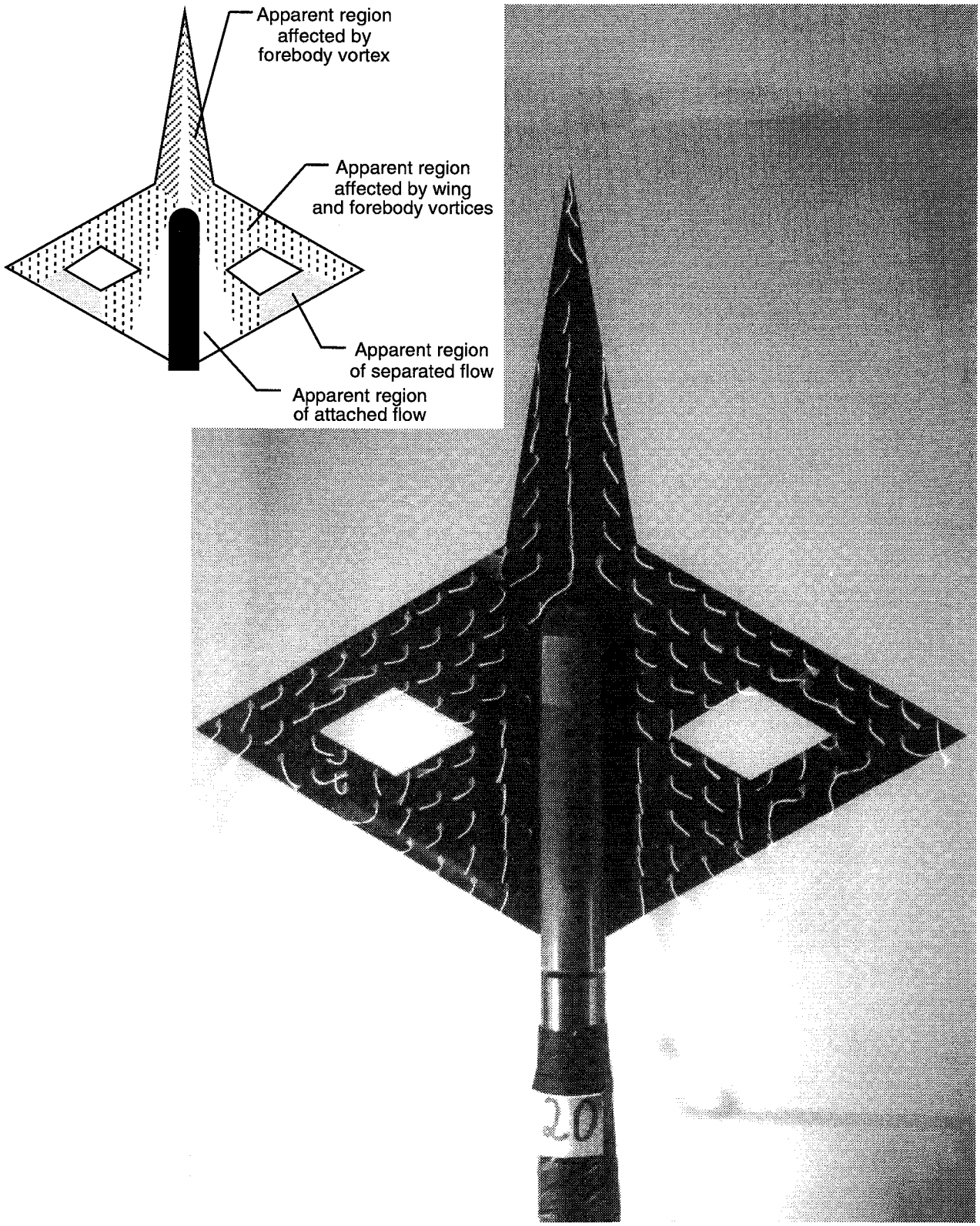

(a) $\alpha = 20°$.

Figure 23. Surface flow visualization on 30° diamond with diamond cutout.

C-2

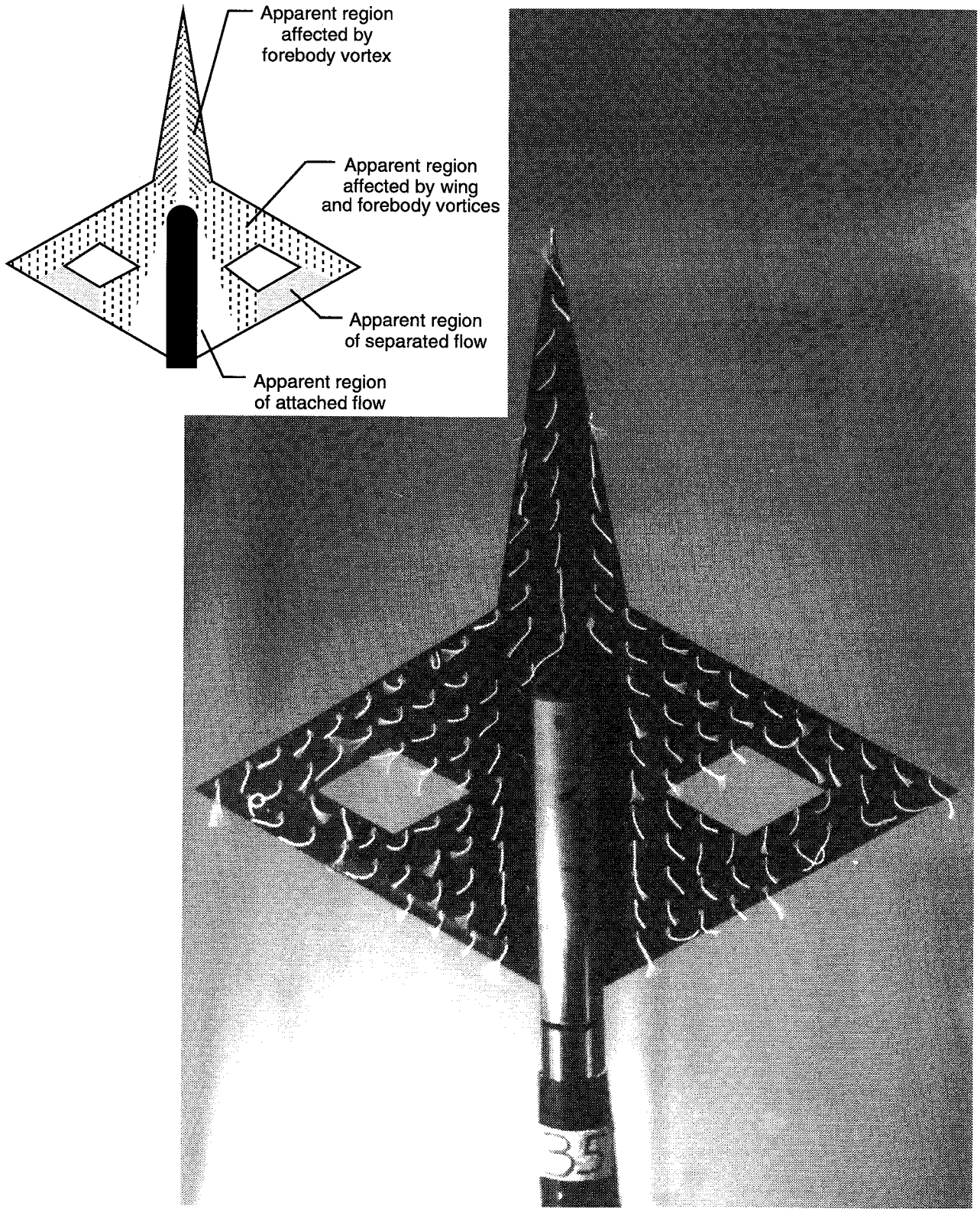

(b) $\alpha = 35°$.

Figure 23. Continued.

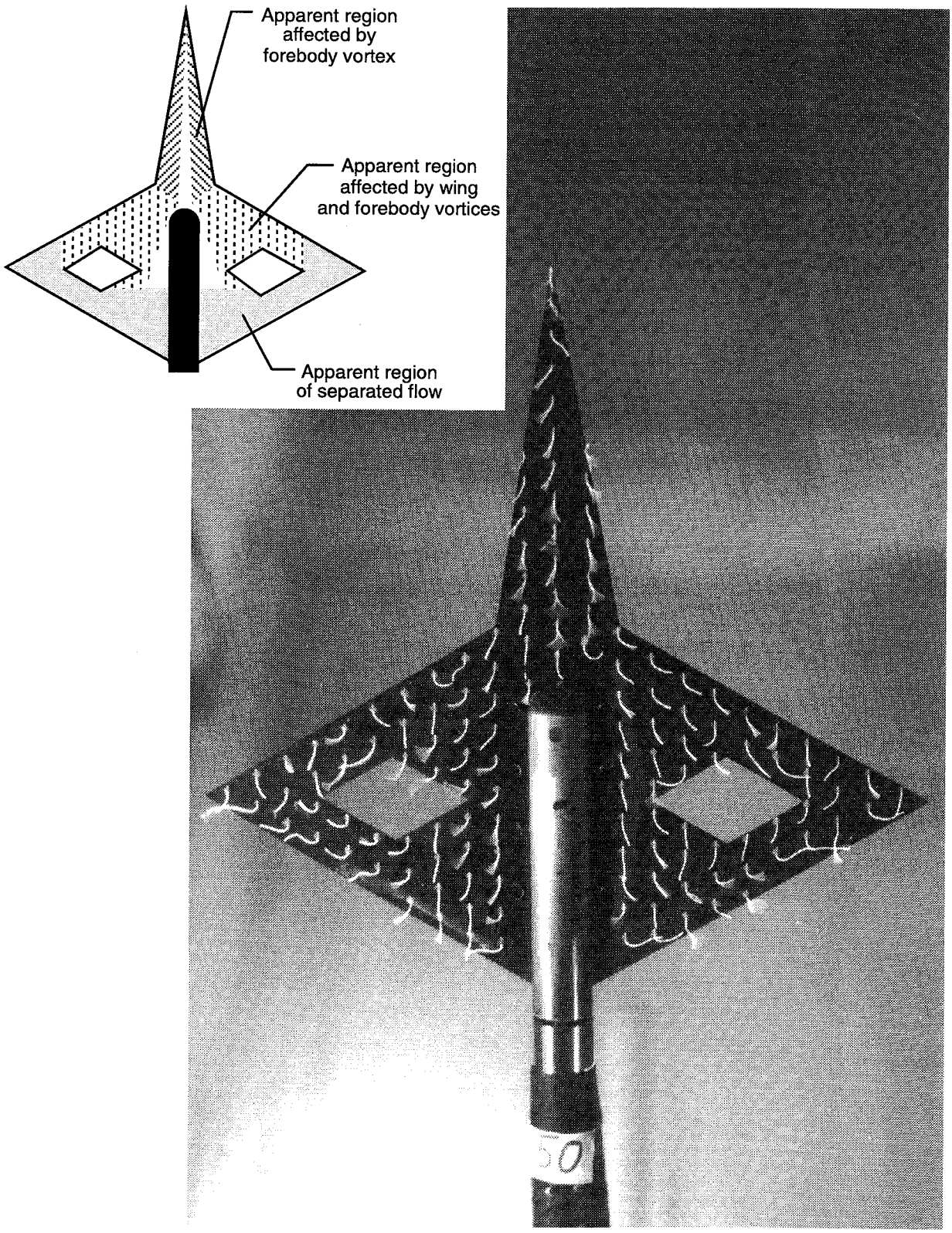

(c) $\alpha = 50°$.

Figure 23. Concluded.

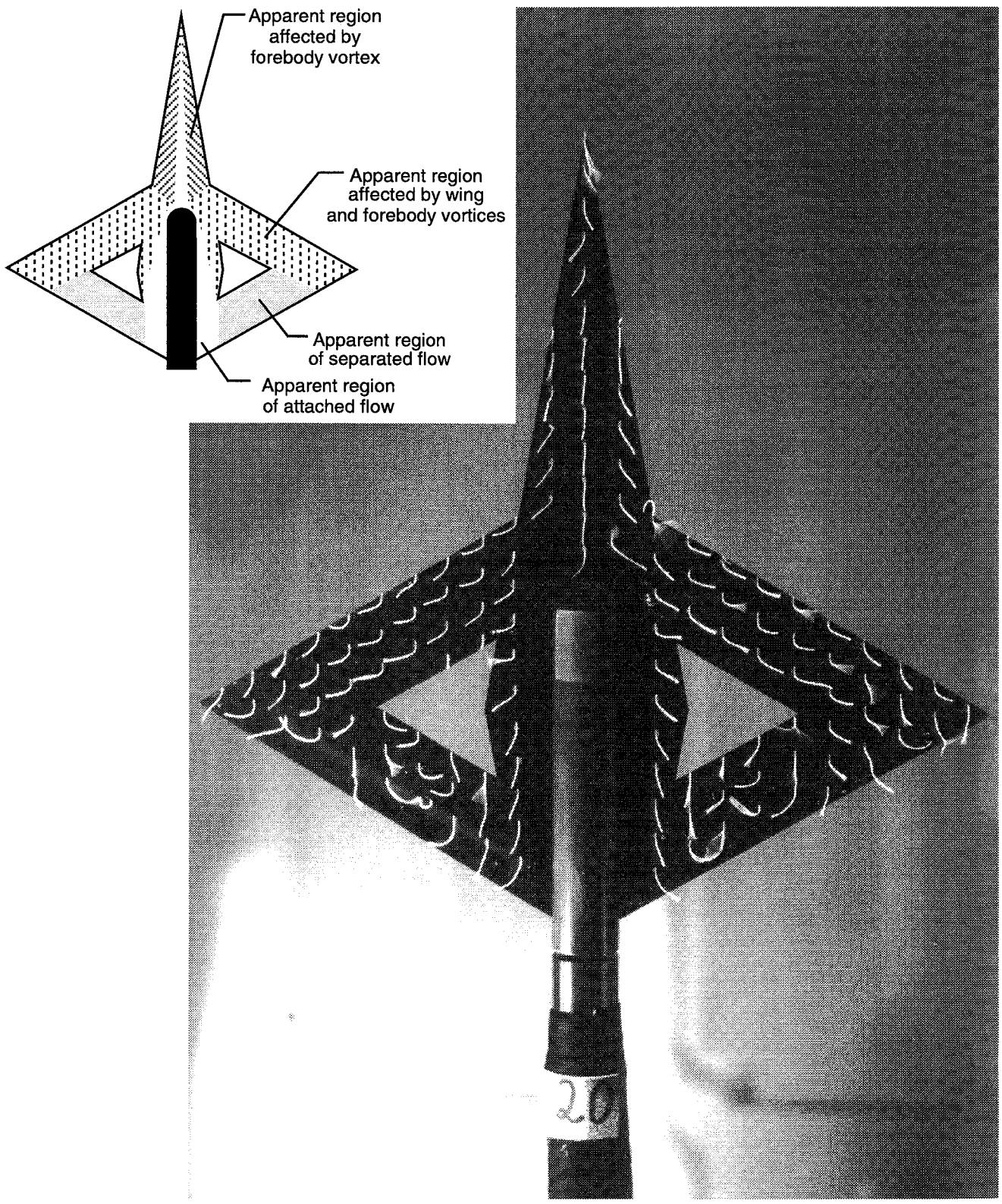

(a) $\alpha = 20°$.

Figure 24. Surface flow visualization on 30° diamond with smallest cutout.

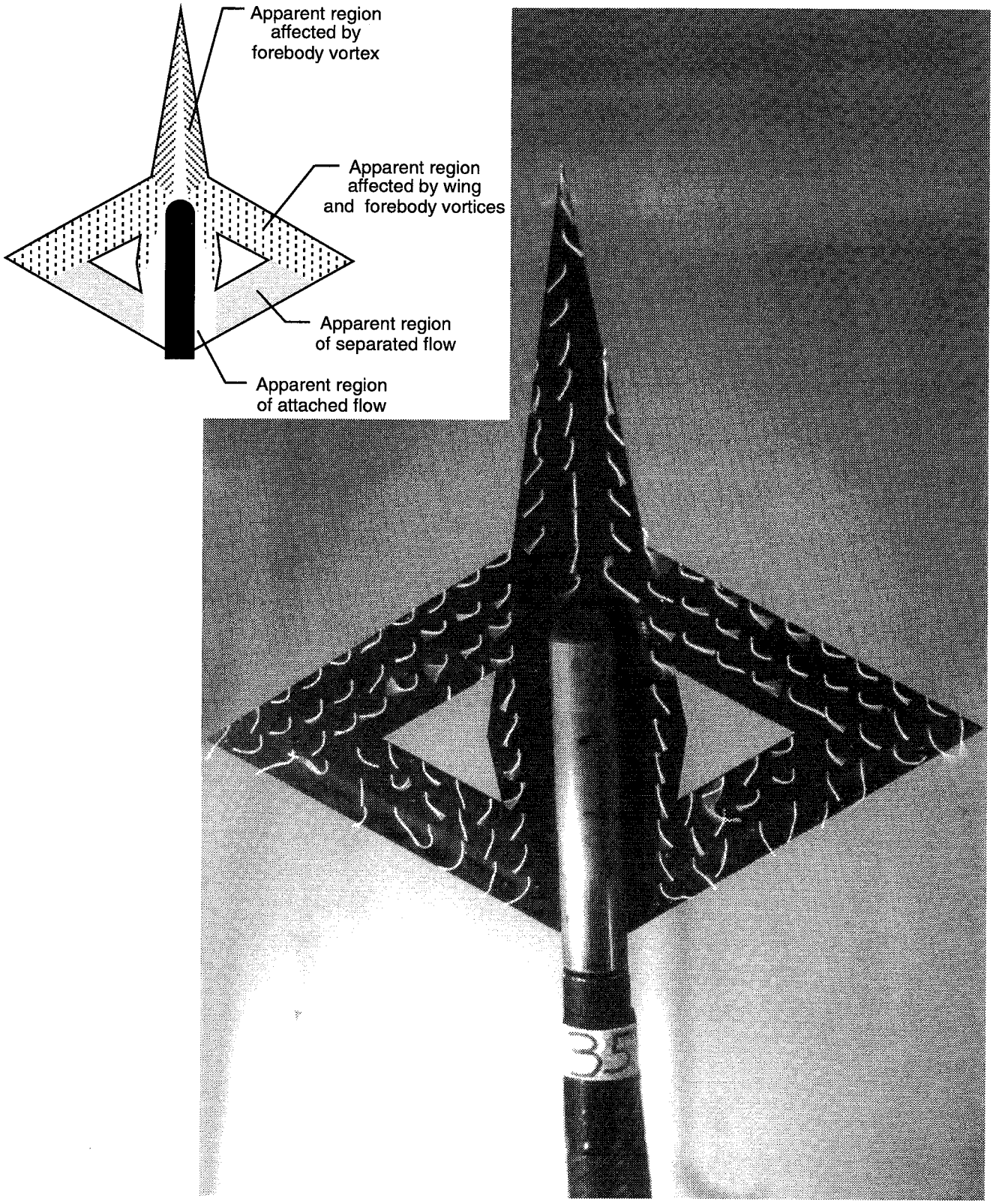

(b) $\alpha = 35°$.

Figure 24. Continued.

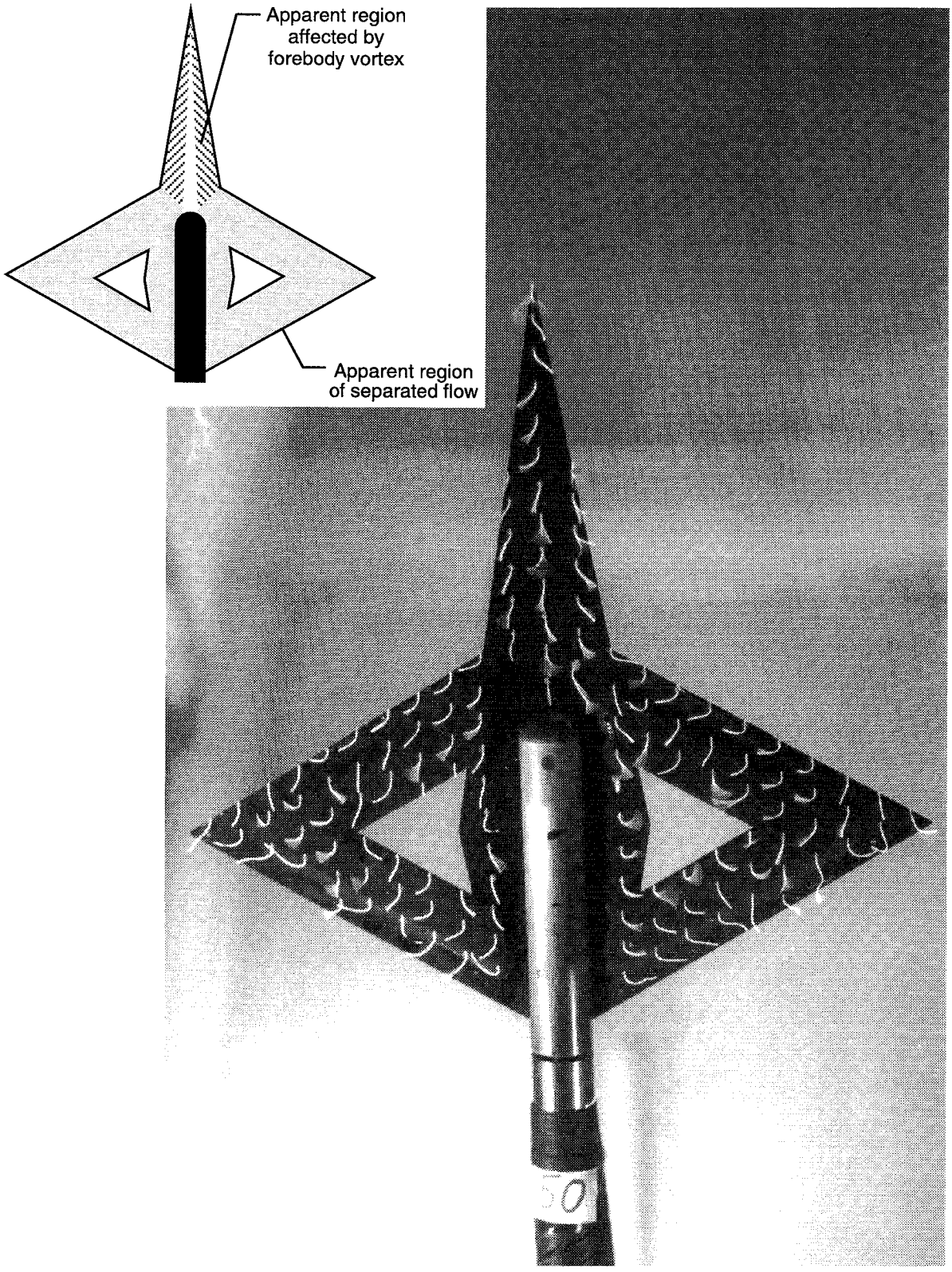

(c) $\alpha = 50°$.

Figure 24. Concluded.

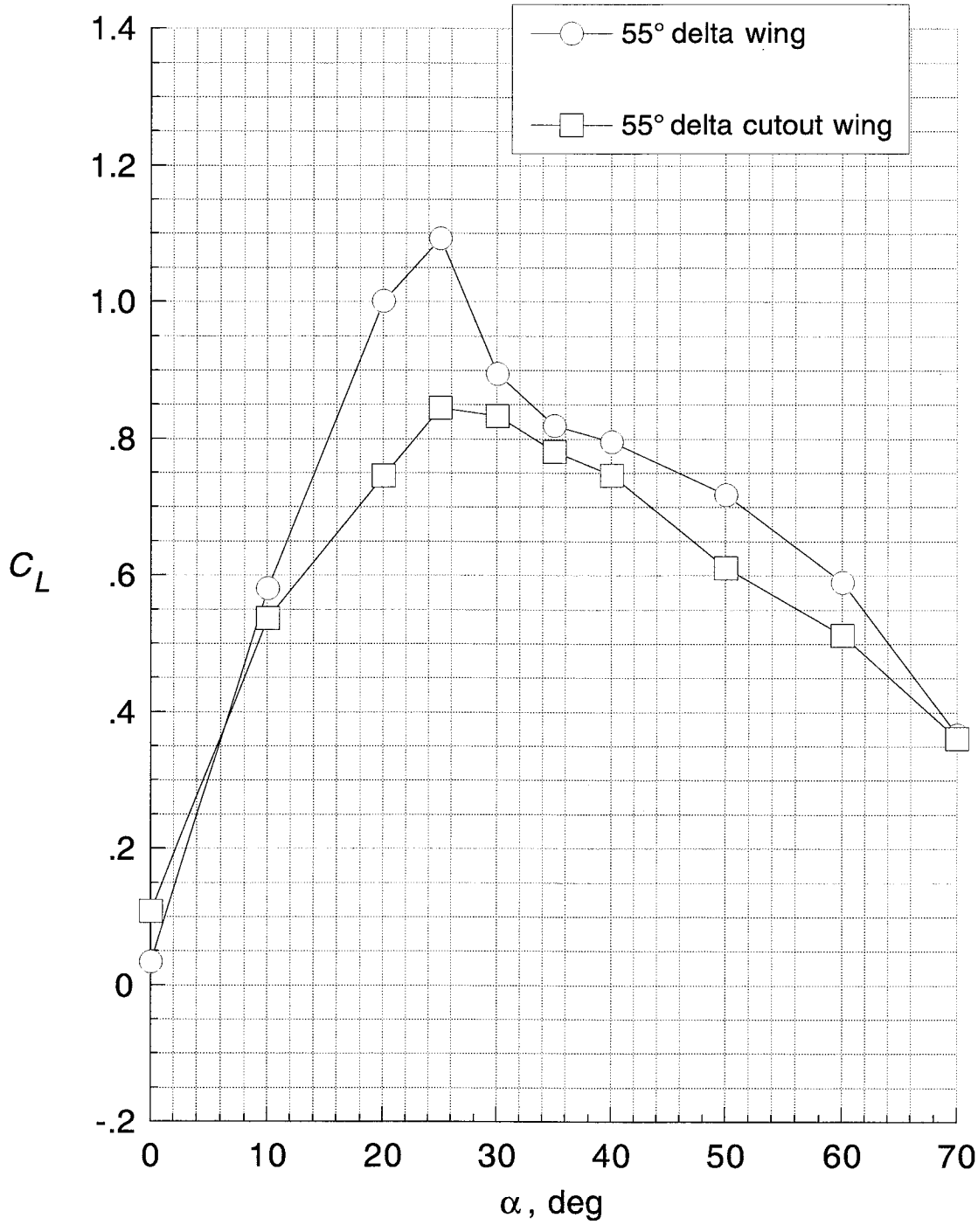

(a) Lift coefficient versus angle of attack.

Figure 25. Longitudinal data illustrating effects of cutout on 55° delta wing.

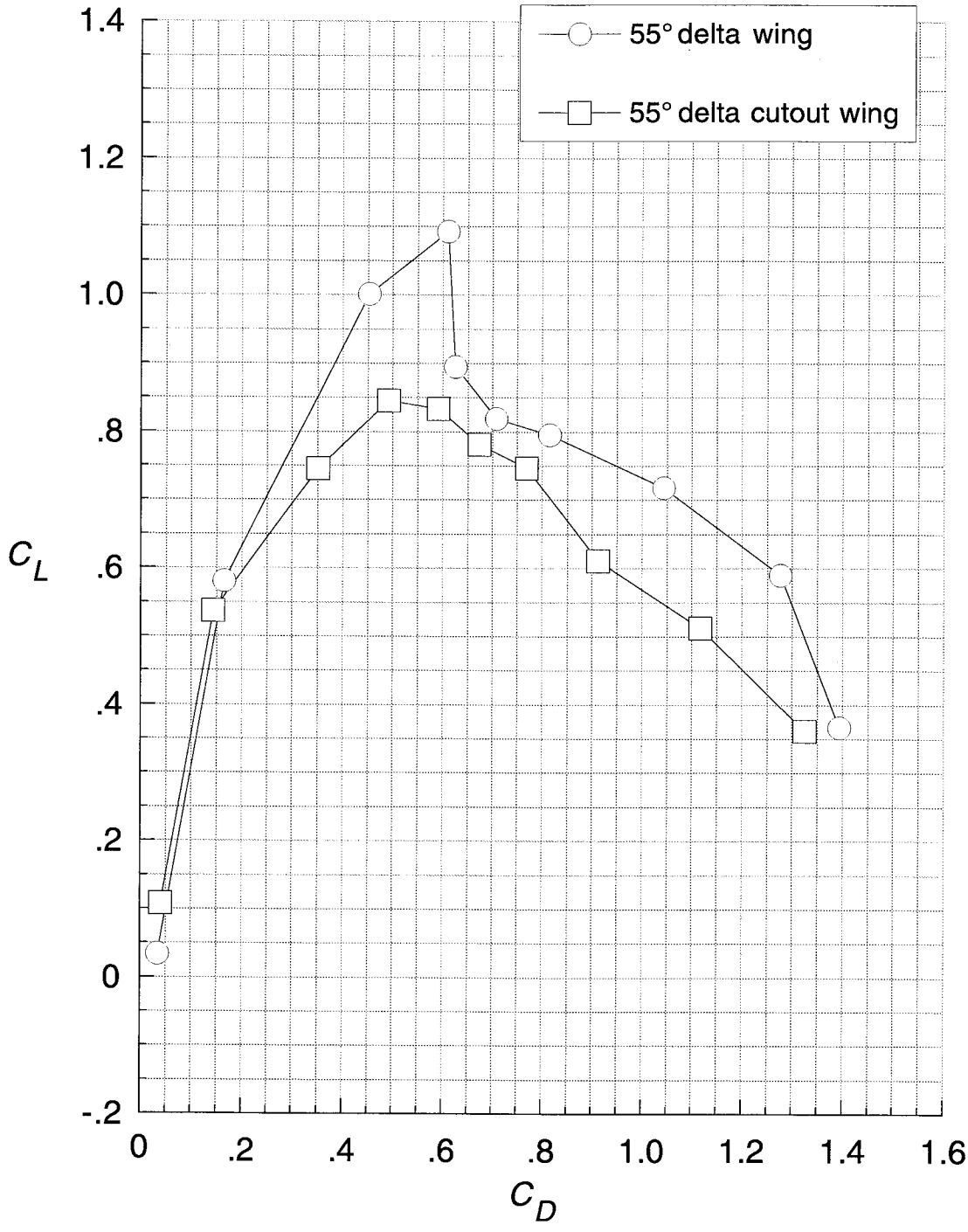

(b) Lift coefficient versus drag coefficient.

Figure 25. Continued.

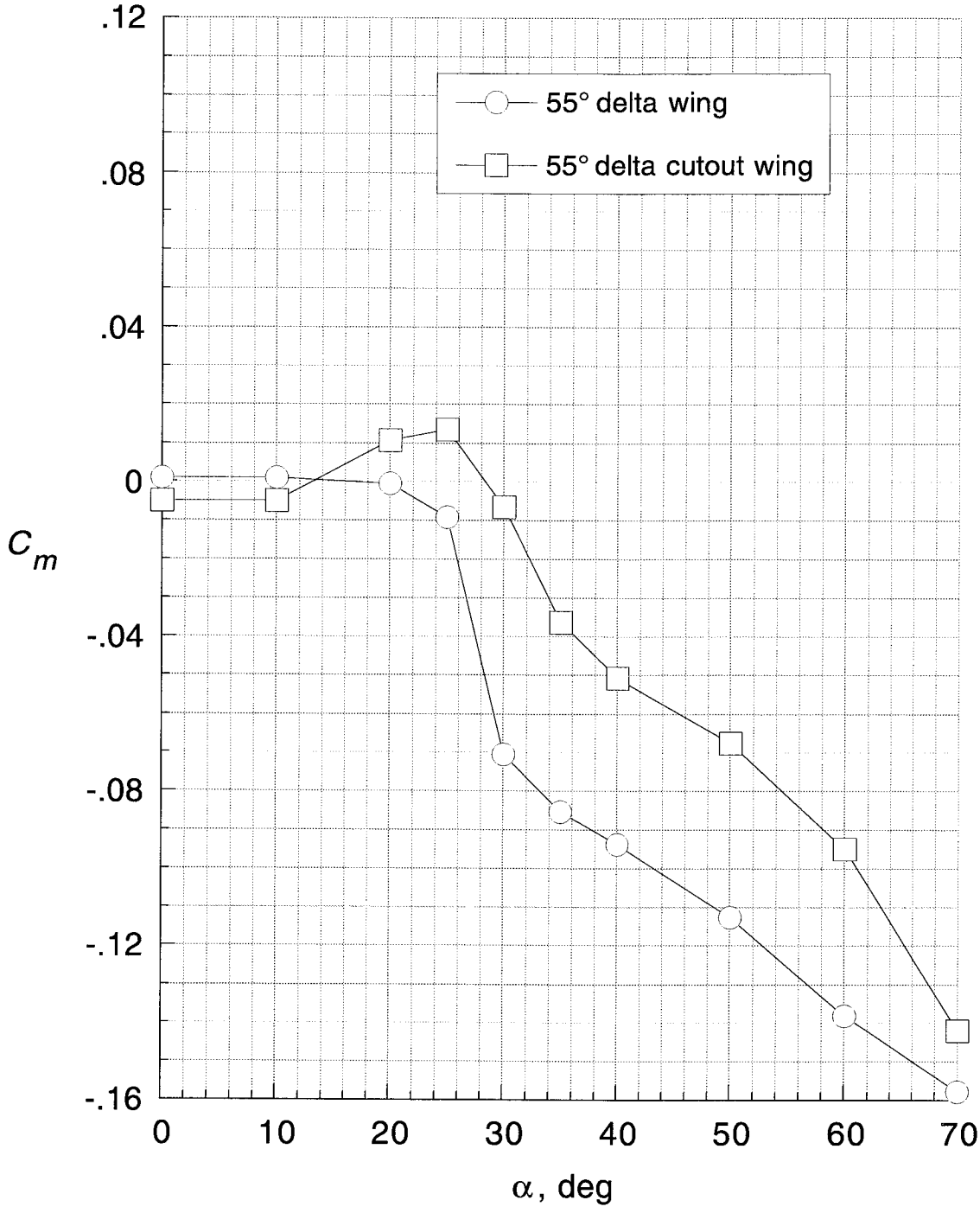

(c) Pitching-moment coefficient versus angle of attack.

Figure 25. Concluded.

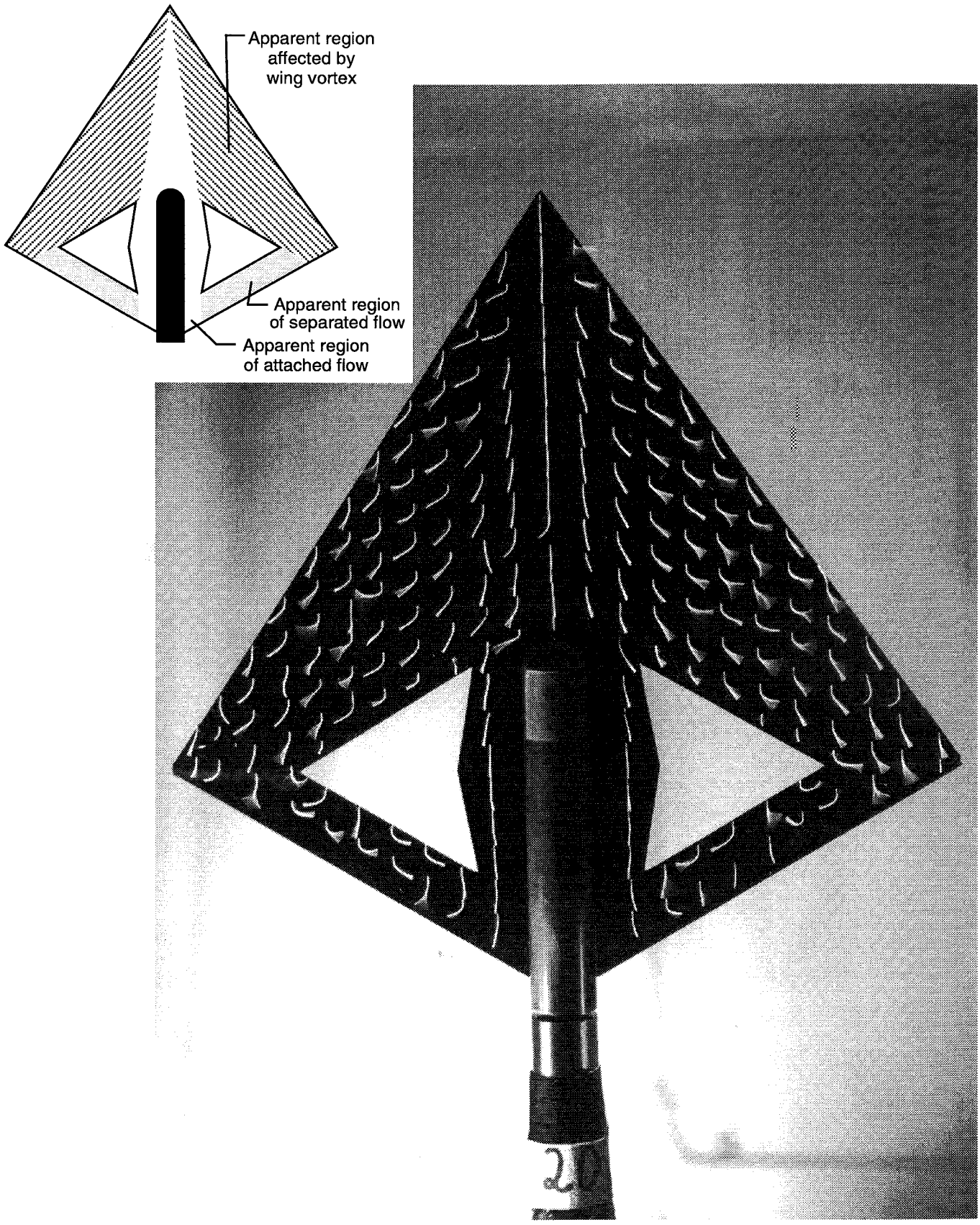

(a) $\alpha = 20°$.

Figure 26. Surface flow visualization on 55° delta cutout wing.

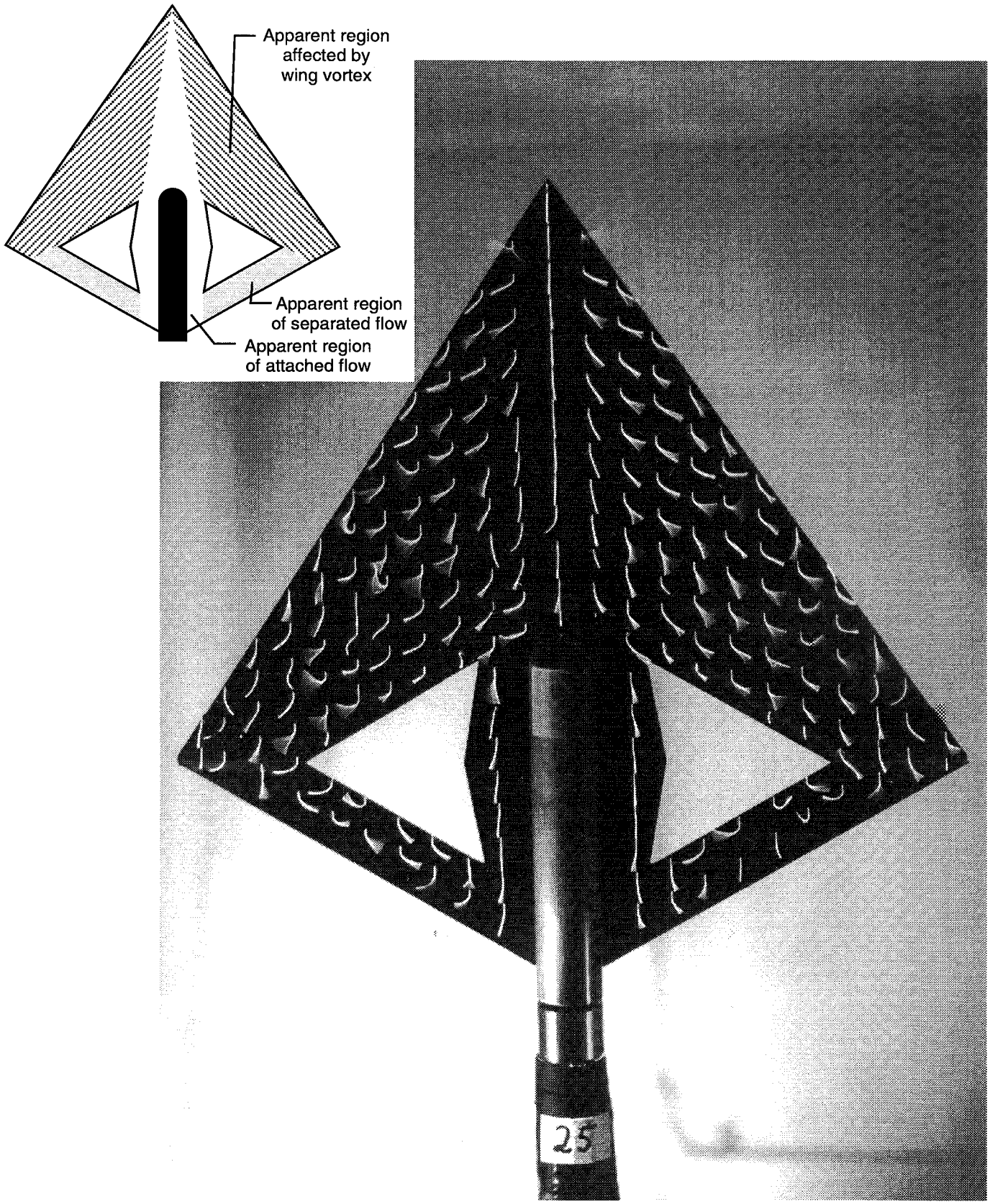

(b) $\alpha = 25°$.

Figure 26. Continued.

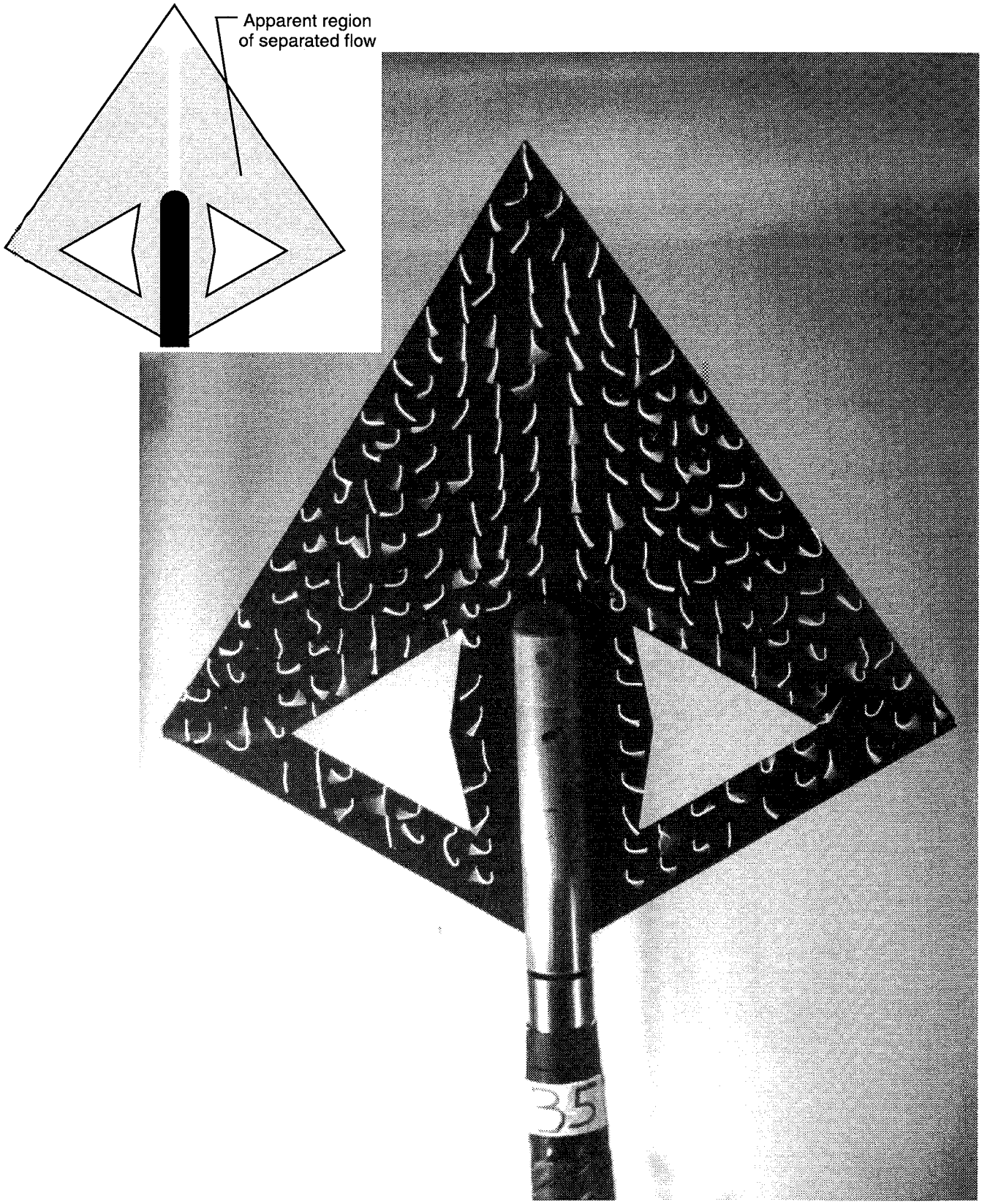

(c) $\alpha = 35°$.

Figure 26. Continued.

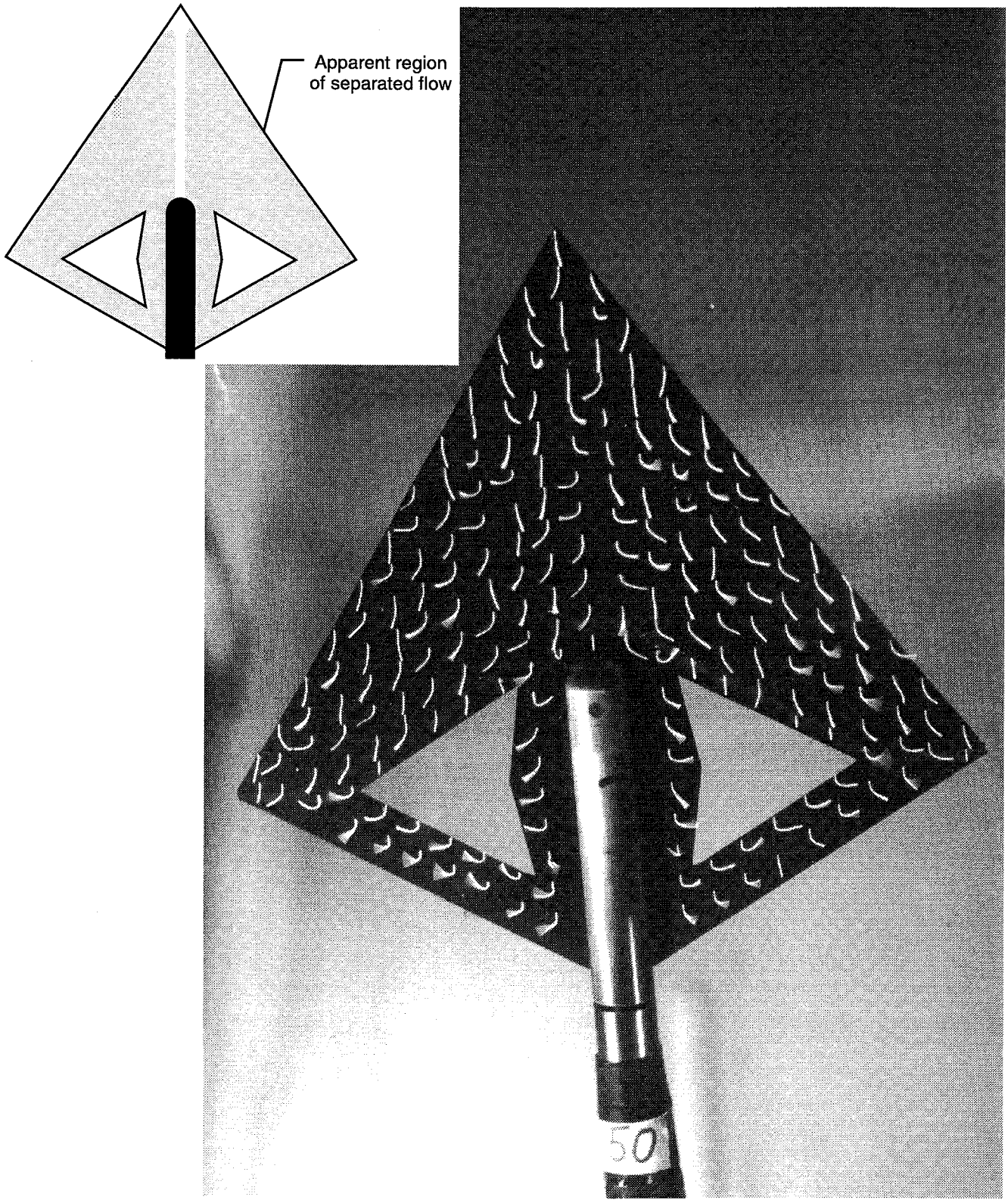

(d) $\alpha = 50°$.

Figure 26. Concluded.

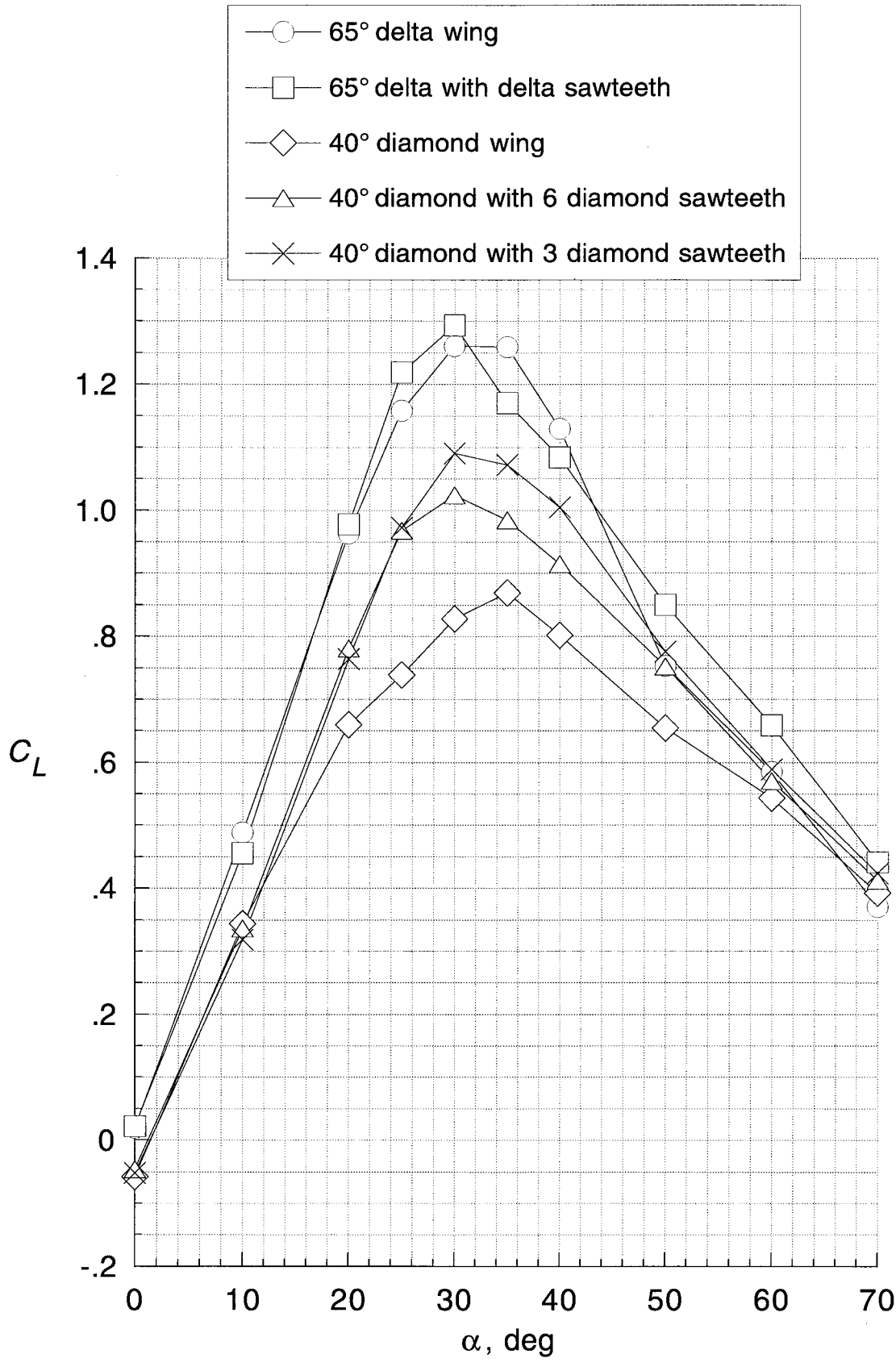

(a) Lift coefficient versus angle of attack.

Figure 27. Longitudinal data illustrating serrated forebody effects.

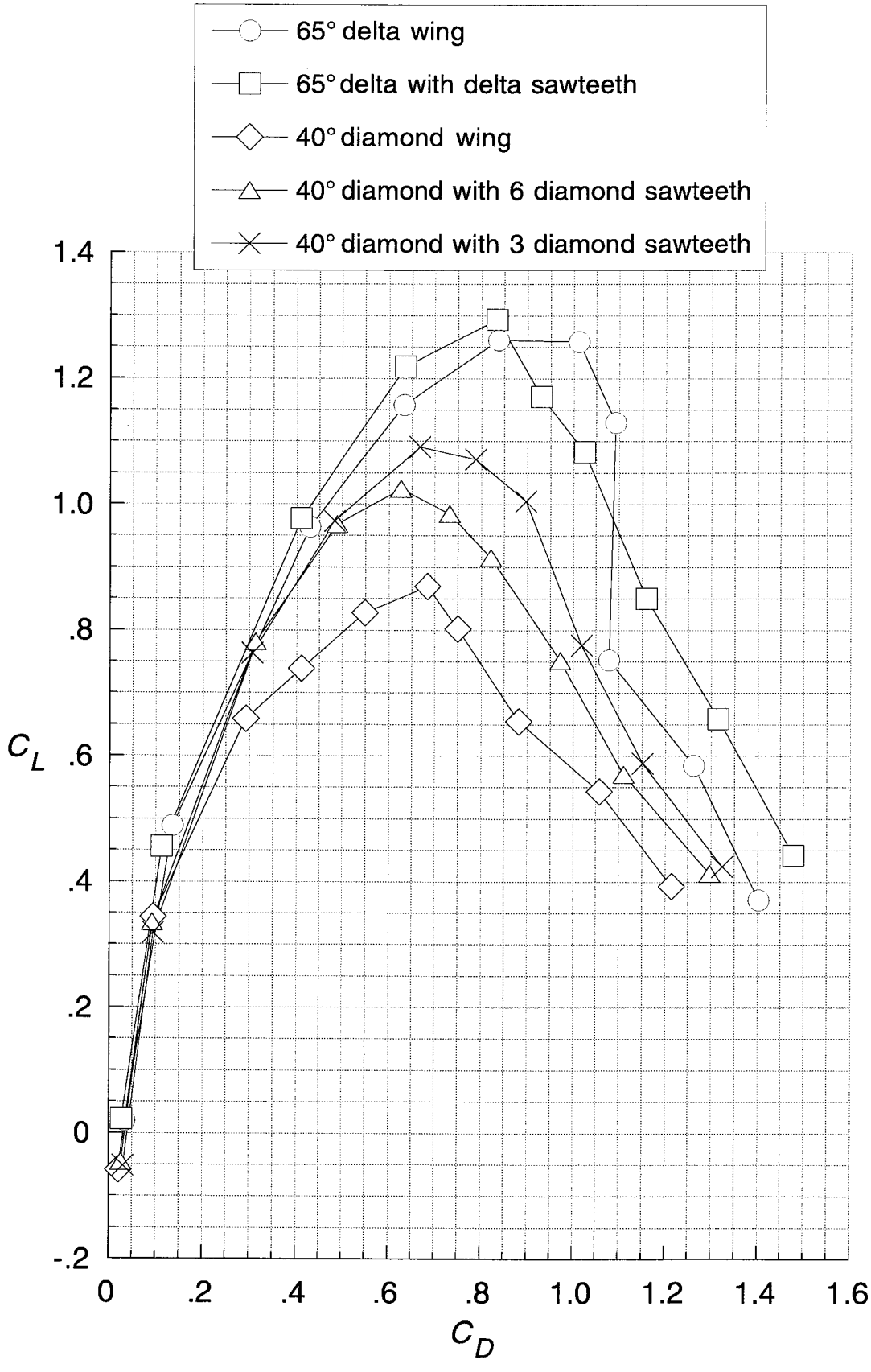

(b) Lift coefficient versus drag coefficient.

Figure 27. Continued.

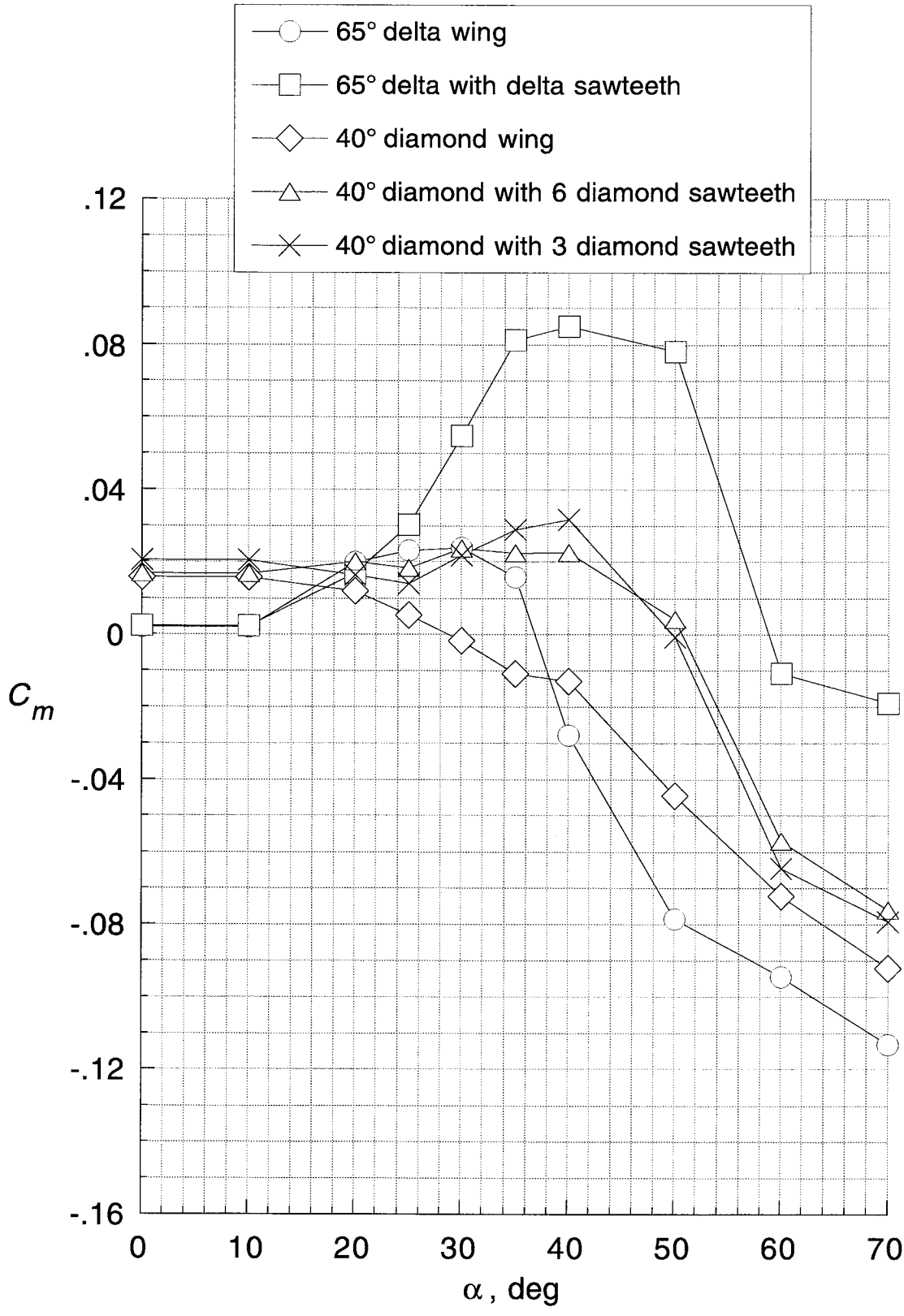

(c) Pitching-moment coefficient versus angle of attack.

Figure 27. Concluded.

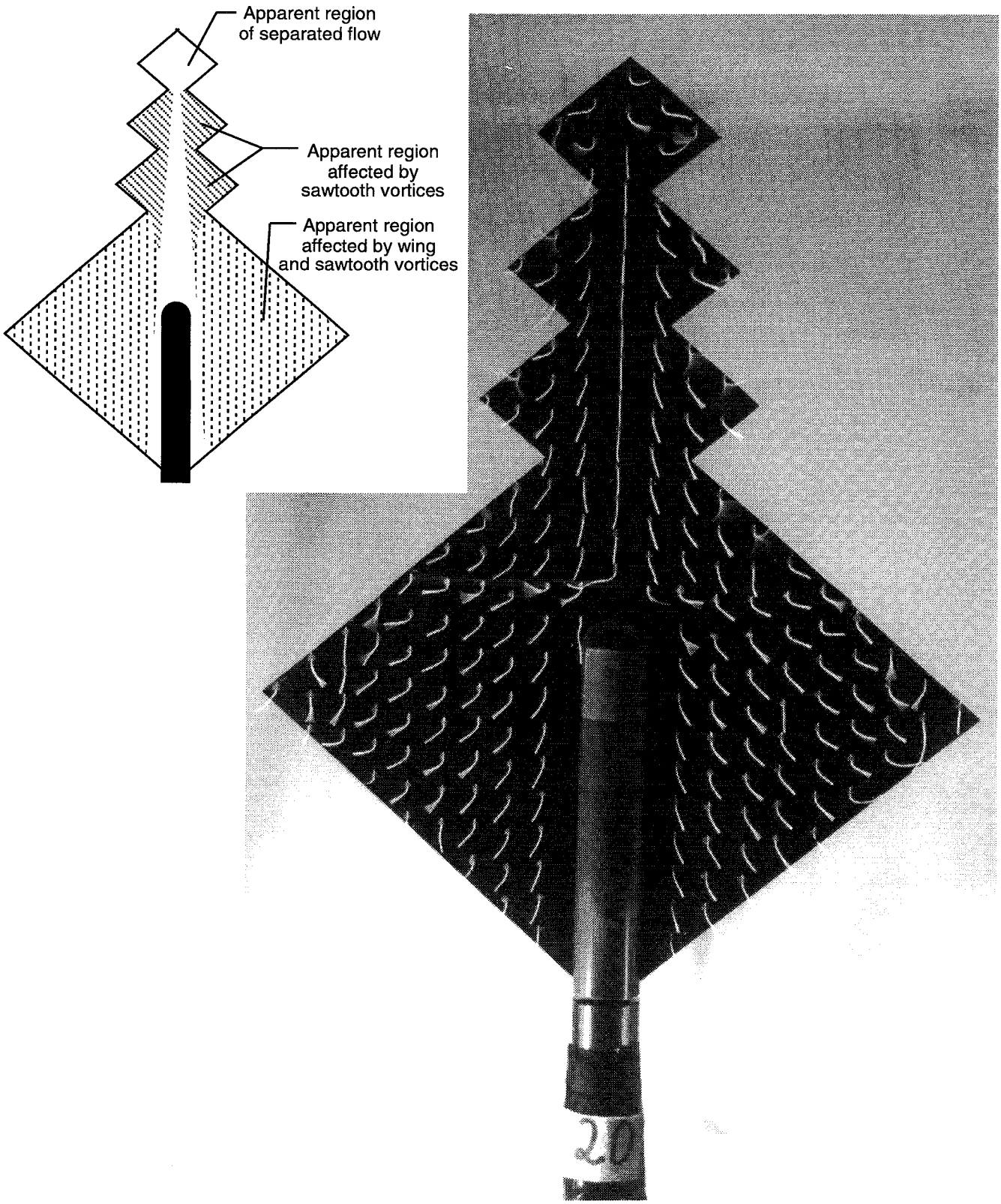

(a) $\alpha = 20°$.

Figure 28. Surface flow visualization on 40° diamond with 3 diamond sawteeth.

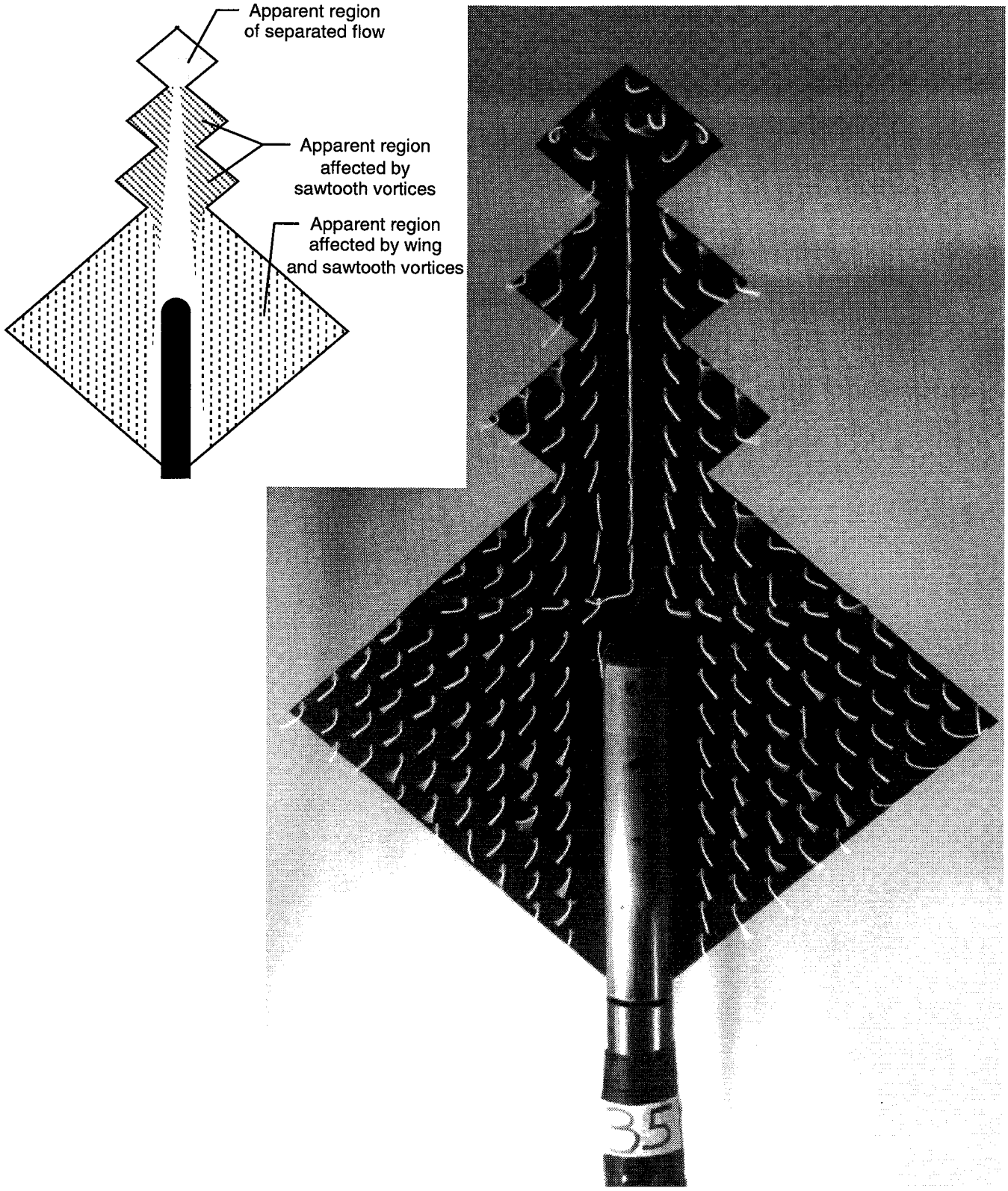

(b) $\alpha = 35°$.

Figure 28. Continued.

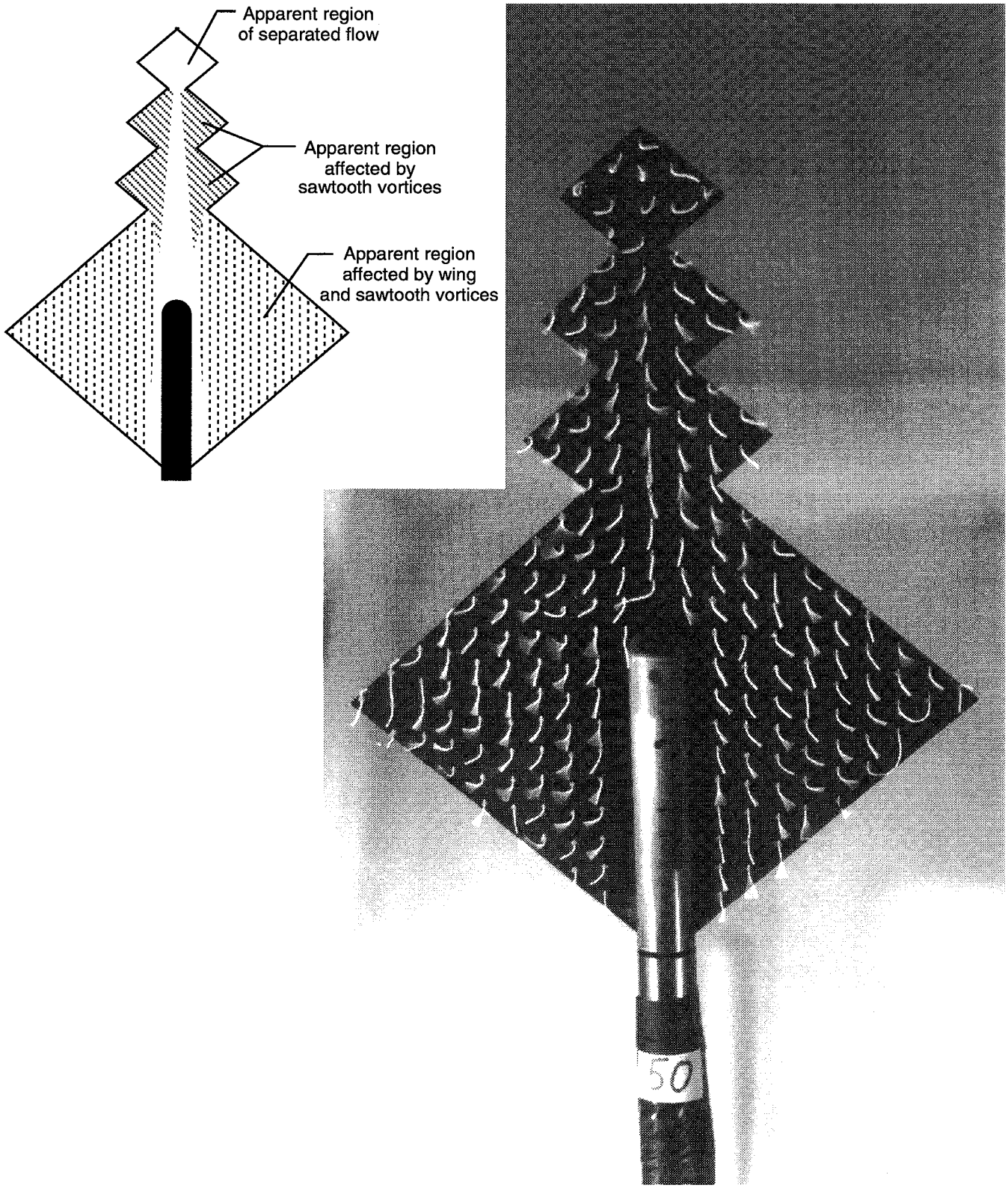

(c) $\alpha = 50°$.

Figure 28. Concluded.

REPORT DOCUMENTATION PAGE

Form Approved
OMB No. 0704-0188

1. AGENCY USE ONLY *(Leave blank)*	2. REPORT DATE	3. REPORT TYPE AND DATES COVERED
	August 1995	Technical Paper

4. TITLE AND SUBTITLE
Low-Speed Longitudinal Aerodynamic Characteristics Through Poststall for Twenty-One Novel Planform Shapes

5. FUNDING NUMBERS
WU 505-68-70-04

6. AUTHOR(S)
Gregory M. Gatlin and Brian E. McGrath

7. PERFORMING ORGANIZATION NAME(S) AND ADDRESS(ES)
NASA Langley Research Center
Hampton, VA 23681-0001

8. PERFORMING ORGANIZATION REPORT NUMBER
L-17301

9. SPONSORING/MONITORING AGENCY NAME(S) AND ADDRESS(ES)
National Aeronautics and Space Administration
Washington, DC 20546-0001

10. SPONSORING/MONITORING AGENCY REPORT NUMBER
NASA TP-3503

11. SUPPLEMENTARY NOTES
Gatlin: Langley Research Center, Hampton, VA; McGrath: Lockheed Engineering & Sciences Company, Hampton, VA.

12a. DISTRIBUTION/AVAILABILITY STATEMENT
Unclassified–Unlimited
Subject Category 02
Availability: NASA CASI (301) 621-0390

12b. DISTRIBUTION CODE

13. ABSTRACT *(Maximum 200 words)*
To identify planform characteristics which have promise for a highly maneuverable vehicle, an investigation was conducted in the Langley Subsonic Basic Research Tunnel to determine the low-speed longitudinal aerodynamics of 21 planform geometries. Concepts studied included twin bodies, double wings, cutout wings, and serrated forebodies. The planform models tested were all 1/4-in.-thick flat plates with beveled edges on the lower surface to ensure uniform flow separation at angle of attack. A 1.0-in.-diameter cylindrical metric body with a hemispherical nose was used to house the six-component strain gauge balance for each configuration. Aerodynamic force and moment data were obtained across an angle-of-attack range of 0° to 70° with zero sideslip at a free-stream dynamic pressure of 30 psf. Surface flow visualization studies were also conducted on selected configurations using fluorescent minitufts. Results from the investigation indicate that a cutout wing planform can improve lift characteristics; however, cutout size, shape, and position and wing leading-edge sweep will all influence the effectiveness of the cutout configuration. Tests of serrated forebodies identified this concept as an extremely effective means of improving configuration lift characteristics; increases of up to 25 percent in the value of maximum lift coefficient were obtained.

14. SUBJECT TERMS
Planform shapes; Low speed; Longitudinal aerodynamics; Twin wing; Twin body; Cutout wing; Serrated forebody; Flow visualization

15. NUMBER OF PAGES
113

16. PRICE CODE
A06

17. SECURITY CLASSIFICATION OF REPORT	18. SECURITY CLASSIFICATION OF THIS PAGE	19. SECURITY CLASSIFICATION OF ABSTRACT	20. LIMITATION OF ABSTRACT
Unclassified	Unclassified	Unclassified	